Detecting tumour responses to treatment using metabolic imaging with hyperpolarised [1-^{13}C]pyruvate and 2-([^{18}F]fluoro)-2-deoxy-D-glucose

Richard L. Hesketh

Christ's College

Supervisor: Professor Kevin Brindle

September 2018

This dissertation is submitted for the degree of Doctor of Philosophy

“After climbing a great hill one only finds that there are many more hills to climb.”

Nelson Rolihlahla Mandela
1918 - 2013

Declaration

This dissertation is the result of my own work and includes nothing which is the outcome of work done in collaboration except as declared in the preface and specified in the text. It is not substantially the same as any that I have submitted, or, is being concurrently submitted for a degree or diploma or other qualification at the University of Cambridge or any other University or similar institution except as declared in the preface and specified in the text. I further state that no substantial part of my dissertation has already been submitted or is being concurrently submitted for any such degree, diploma or other qualification at the University of Cambridge or any other University or similar institution except as declared in the preface and specified in the text.

It does not exceed 60,000 words.

Contents

Acknowledgements

Firstly I must thank Kevin Brindle for giving me the opportunity to do my PhD in his lab and for the subsequent supervision over the last 4 years. Without his support for new ideas and guidance the work in this thesis would not have been possible and it has been educational, enjoyable and a huge privilege to have had so many extended discussions with him about science, clinicians and life! I also have to thank CRUK for funding my PhD and the support of Christ's College and the University of Cambridge.

The fantastic team at CRUK Cambridge Institute has also made much of the research presented here possible and deserve thanks here. Despite regular attempts to make me denounce hyperpolarised MR and become a PET convert David Lewis has become a close friend. Although most of our protracted discussions shouldn't (and won't) be discussed outside the PET room, working in the basement wouldn't have been half the fun without them. At the same time many of the experiments described in this thesis were planned and executed during those many hours. Despite his untimely repatriation to Glasgow I have no doubt we will stay in touch personally and professionally. Alan Wright has provided brilliant advice throughout the last four years, particularly about NMR / MRI, and I will miss his enthusiasm and our many hours spent together, particularly at ISMRM 2018 – watching England score in the 90th min to beat Tunisia in a Parisian bar full of Tunisians being a particular highlight! It has been a pleasure to work with all the other members of the Brindle lab, particularly Sarah McGuire, Susana Ros, Dmitry Soloviev, De-en Hu, André Neves, Franz Schilling. All are incredibly talented in their respective fields and have been approachable and helpful throughout.

Thanks must also go to my fellow PhD students. Many of the experiments performed here would not have been possible without Jiazheng Wang who designed the hyperpolarised imaging sequences used. We performed almost all the PET/MRI experiments together throughout, engraining the words 七，八，九 in my vocabulary forever! It has been a privilege to work with Jay and I hope that the opportunity arises to do so again in the future (or at least a visit to Beijing!). Robbie Bielik has been great fun to work with and I look forward to catching up with him in… Glasgow? Kerstin Timm, living proof that there is nothing wrong with the German sense of humour, made life at the CI lots of fun, particularly during the days of Insanity and at ISMRM. Lynn Asante-Asare, Richard Mair and Eva Serrao and have also been a lot of fun to work with and are trusted friends and colleagues.

Finally, I have to thank my family which has grown by two during my PhD. My wife Becky has been an absolute rock, I have no idea how I ended up with somebody so selflessly supportive of everything I have done: the late nights in the lab, the weekends and nights in A&E and, to a lesser extent, the intensive hockey schedule. And then along came Bryony, wriggles and all. The last ten months have been hugely enjoyable and I cannot express how happy I am to see your smile in the morning, it's just the best part of my day. Finally, Mum and Dad, I simply cannot thank you enough. As with everything in my life your support has been unwavering and I am incredibly lucky to have you, be able to discuss science and medicine with you (only occasionally berating genomics for its lack of clinical impact!) and being able to stay in the West Wing with all of its culinary and bed-making assets!

Abbreviations

[^{18}F]FDG	2-([^{18}F]fluoro)-2-deoxy-D-glucose
2-HG	2-hydroxyglutarate
α-KG	alpha ketoglutarate
AA	ascorbic acid
ACT	alanine, serine cysteine transporters
ADP	adenosine diphosphate
AKT	protein kinase B
ALT	alanine transaminase
ATP	adenosine triphosphate
AUC	area under the curve
BCAA	branched chain amino acid
BCAT	branched chain amino acid aminotransferase
BLI	bioluminescence imaging
Bq	becquerel
CAIX	carbonic anhydrase 9
CC3	cleaved caspase-3
CCL	chemokine ligand
COX	cyclo-oxygenase
CT	computed tomography
DCE	dynamic contrast enhanced
DCT	dicarboxylate transporters
DHA	dehydroascorbic acid
DHAR	dehydroascorbate reductase
DNA	deoxyribonucleic acid

DNP	dynamic nuclear polarisation
DSE	dual spin echo
EDTA	ethylenediaminetetraacetic acid
EGF	epidermal growth factor
EPI	echo planar imaging
FACS	fluorescence activated cell sorting
FH	fumarate hydratase
FID	free induction decay
FLASH	fast low angle shot
FLI	fluorescence imaging
FOV	field of view
FOX	forkhead box
FSE	fast spin echo
GAPDH	glyceraldehyde-3-phosphate dehydrogenase
GGT	gamma-glutamyltransferase
GLDH	glutamine dehydrogenase
GLS	glutaminase
GLUT	glucose transporter
GPI	glucose-6-phosphate isomerase
GSSG	glutathione disulphide
Gy	gray
H&E	haematoxylin and eosin
HIF	Hypoxia-inducible factor
HK	hexokinase
HPLC	high performance liquid chromatography

IDH	isocitrate dehydrogenase
Ig	immunoglobulin
IL	interleukin
KIC	alpha-ketoisocaproate
LDH	lactate dehydrogenase
LN	laminin
mAb	monoclonal antibody
MCP	monocyte chemoattractant protein
MCT	monocarboxylate transporter
MIP	maximum intensity projection
MMP	matrix metalloproteinase
MRI	magnetic resonance imaging
MRS	magnetic resonance spectroscopy
mTOR	mammalian target of rapamycin
NAD^+	nicotinamide adenine dinucleotide
NADH	reduced nicotinamide adenine dinucleotide
NADPH	reduced nicotinamide adenine dinucleotide phosphate
NMR	nuclear magnetic resonance
p.p.m.	parts per million
PARP	poly-ADP ribose polymerase
PBS	phosphate buffered saline
PC	pyruvate carboxylase
PCA	perchloric acid
PDGF	Platelet-derived growth factor
PDH	pyruvate dehydrogenase

PDK	pyruvate dehydrogenase kinase
PET	positron emission tomography
PFK	phosphofructokinase
PGK	phosphoglycerate kinase
PGM	phosphoglycerate mutase
PI3K	phosphatidylinositol-4,5,-bisphosphate-3-kinase
PK	pyruvate kinase
PPP	pentose phosphate pathway
PSMA	prostate specific membrane antigen
PTEN	phosphatase and tensin homolog
RECIST	Response Evaluation Criteria in Solid Tumours
RF	radiofrequency
ROI	region of interest
ROS	reactive oxygen species
SCO2	synthesis of cytochrome c oxidase 2
SD	standard deviation
SDH	succinate dehydrogenase
SEM	standard error of the mean
SNR	signal to noise ratio
SPECT	single photon emission computed tomography
SpSp	spectral-spatial
SUV	standardised uptake value
SVCT	sodium-ascorbate co-transporter
T_1	spin-lattice relaxation time
T_2	spin-spin relaxation time

TAC	time activity curve
TCA cycle	tricarboxylic acid cycle
TE	echo time
TETs	ten-eleven translocation proteins
TIGAR	TP53-inducible glycolysis and apoptosis regulator
TNF	tumour necrosis factor
TPI	triosephosphate isomerase
TR	repetition time
TRAIL	TNF-related apoptosis-inducing ligand
TUNEL	terminal deoxynucleotidyl transferase nick-end labelling
VEGF	vascular endothelial growth factor

Summary

Earlier detection of tumour responses to treatment would facilitate modification of treatment regimens and reduce unnecessary side effects and the costs of ineffective therapy. Anatomical changes following treatment are often slow to manifest and are occasionally misleading. Molecular imaging targeting dysregulated metabolic pathways in tumours can facilitate earlier detection of treatment response. The aim of this study was to directly compare two metabolic imaging techniques that measure different parts of glycolysis, 2-([^{18}F]fluoro)-2-deoxy-D-glucose positron emission tomography ([^{18}F]FDG-PET) and hyperpolarised [1-^{13}C]pyruvate magnetic resonance imaging), for the purpose of detecting early responses to treatment in mouse models of cancer.

Two mouse models of lymphoma, subcutaneous EL4 tumours and Eμ-*Myc* transgenic mice, were treated with etoposide and cyclophosphamide, respectively. In EL4 tumours 24 h after treatment there was a significant reduction in [^{18}F]FDG uptake with no significant change in the hyperpolarised [1-^{13}C]lactate/[1-^{13}]Cpyruvate ratio. While treatment resulted in significant decreases in glucose transporter expression, there were variable amounts of cell death before and after treatment, potentially explaining this discrepancy. In Eμ-*Myc* mice, reductions of both [^{18}F]FDG uptake and the [1-^{13}C]lactate/[1-^{13}C]pyruvate ratio were observed after treatment. However, the decreases in [^{18}F]FDG uptake in cervical tumours were partially masked by high uptake in surrounding tissues demonstrating the benefit of improved specificity of hyperpolarised [1-^{13}C]pyruvate for detecting the Warburg effect.

In two xenograft models of human colorectal and breast adenocarcinoma, a large reduction in hyperpolarised [1-^{13}C]lactate/[1-^{13}C]pyruvate ratio was observed in all tumours 24 hours after treatment with a TRAIL agonist. However, despite treatment inducing widespread apoptosis and long-term remission, [^{18}F]FDG-PET largely failed to detect a response. Measurements of [^{18}F]FDG uptake in disaggregated tumour cells that had been sorted by fluorescence-activated cell sorting demonstrated that inflammatory infiltration or activation was not responsible for failure to detect a response to treatment with [^{18}F]FDG. Furthermore, [1,6 $^{13}C_2$]glucose infusions into tumour bearing mice demonstrated that tumour uptake of [^{18}F]FDG after treatment was not reflective of overall glycolytic flux.

Publications

Hesketh RL, Wang J, Wright AJ, Lewis DY, Denton AE, Grenfell R, Miller JL, Bielik R, Gehrung M, Fala M, Ros S, Xie B, Hu DE, Brindle KM. Magnetic resonance imaging is more sensitive than PET for detecting treatment-induced cell-death dependent changes in glycoloysis. *Cancer Research.* 2019. Epub ahead of print.

Hesketh RL, Brindle KM. Magnetic resonance imaging of cancer metabolism with hyperpolarized 13C-labeled cell metabolites. *Current Opinion in Chemical Biology.* 2018. Accepted for publication.

Wang J, Wright AJ, Hu DE, Hesketh RL, Brindle KM. Single shot three-dimensional pulse sequence for hyperpolarized ^{13}C MRI. *Magnetic Resonance in Medicine.* 2017. Feb; 77(2):740-752. Epub 2016, Feb 24.

Wang J, Kreis F, Wright AJ, Hesketh RL, Levitt MH, Brindle KM. Dynamic ^{1}H imaging of hyperpolarized [1-^{13}C]lactate *in vivo* using a reverse INEPT experiment. *Magnetic Resonance in Medicine.* 2018. Feb; 79(2)741-747. Epub 2017, May 5.

Wang J, Wright AJ, Hesketh RL, Hu DE, Brindle KM. A referenceless Nyquist ghost correction workflow for echo planar imaging of hyperpolarized [1-^{13}C]pyruvate and [1-^{13}C]lactate. *NMR in Biomedicine.* 2018. Feb; 31(2). Epub 2017, Dec 7.

Awards

Joint Annual Meeting ISMRM-ESMRMB 2018. Multi-modality molecular imaging with hyperpolarized [1-^{13}C]pyruvate MRSI and ^{18}FDG-PET of early tumor response to a novel TRAIL agonist. Magna cum laude.

Joint Annual Meeting ISMRM-ESMRMB 2018. Multi-modality molecular imaging with hyperpolarized [1-^{13}C]pyruvate MRSI and ^{18}FDG-PET of early tumor response to a novel TRAIL agonist. 1st place in MR in Drug Research Study Group.

World Molecular Imaging Congress September 2017. Multi-modality molecular imaging of early tumor response to a novel TRAIL agonist (MEDI3039) in a mouse model of colorectal cancer. Highlights lecture.

List of Tables

List of Figures

1. Introduction

1.1. Cancer

Cancer is the second most common cause of death worldwide and, despite the significant resources that have been devoted to research and clinical oncology, it is still the cause of one in four deaths in the UK[1, 2]. Cancer is a heterogeneous group of diseases characterised by dysregulated cell proliferation that may, when combined with an acquired invasive phenotype, spread into surrounding tissues and metastasise to distant sites. Cancers can broadly be categorised by tissue of origin, each a distinct disease with its own risk factors, epidemiology, pattern of disease, treatment and prognosis. However, all cancers share the common pathogenesis of genetic mutations in the signalling pathways that control proliferation and apoptosis, normal processes that are required for development and maintenance of tissues throughout the lifetime of multi-cellular organisms[3].

DNA mutation results from errors of replication and damage to DNA. The majority of DNA damage arises as a result of endogenous processes, most frequently oxidative damage from reactive oxygen species (ROS), but a large number of other naturally generated chemicals also cause a myriad of DNA aberrations[4]. Endogenous DNA damage is mostly unavoidable but humans are also exposed to a large number of exogenous mutagens that not only add to the overall mutational burden but can disproportionately promote tumourigenesis by causing specific mutations at susceptible points in the genome. For example, aflatoxin B_1 exposure strongly predisposes to development of hepatocellular carcinoma by causing a codon R249S substitution in *TP53*, the most frequently mutated gene in human cancer[5]. Tobacco smoking, to which over one-fifth of cancers are attributed, can increase the number of mutations per cell per year by up to 150[6]. Furthermore, benzo[*a*]pyrene, a carcinogen in cigarette smoke, forms adducts at codons 157, 248 and 273 in *TP53*, mutations

seen in a majority of smoking-induced lung cancers[7]. DNA damage events are estimated at 10^4 - 10^5 lesions per day per cell. However, very efficient mechanisms prevent the propagation of mutations by repair or activation of cellular senescence or apoptosis, reducing the rate of somatic mutations permanently fixed in the genome to <1 per cell per day[8-10].

The majority of mutations do not change gene expression and have no cellular effects but, as a result of accelerated Darwinian evolution, mutations that increase survival and proliferation accumulate over time, predisposing to the development of cancer. Theoretically, cancer cells can result from mutations in any component of the signalling pathways that control proliferation. In reality, a small subset of "driver" mutations in oncogenes and tumour suppressor genes of select pathways are mutated with high frequency and it is generally believed that between one and ten mutated "drivers" are required for the emergence of most tumours[11]. However, mutational burden and "driver mutations" occur at cancer-associated frequencies in over a quarter of normal cells, so clearly they aren't the only determinant of malignancy and one of the biggest challenges facing cancer biology is to differentiate the driver mutations from the noise[12]. Cancer genomes are enormously diverse, with 1000-fold differences existing in the number of mutations across both different cancer types and cancers originating from the same tissue type[13-15]. The types of mutation range from base substitutions, insertions, deletions, amplifications and chromosomal rearrangements to copy number variations and these typically occur at increasing frequencies as cancers evolve[16]. Sequence variations are often accompanied by epigenetic changes that include DNA methylation, histone modification and chromatin changes that can further influence gene expression.

Signalling pathway mutations result in cancer cells being able to proliferate independently of normal growth factor signalling. Similar mechanisms can cause the failure of inhibitory growth signals to prevent proliferation and can even be subverted to promote the acquisition of an invasive and metastatic phenotype[17]. In contrast to normal cells, tumour cells can undergo unlimited cycles of growth and division. The ends of chromosomes are protected by telomeres, lengths of hexanucleotide repeats that shorten with each round of cell division, and cells become senescent once these are lost. Tumours are able to extend the lengths of telomeres, usually by expressing the enzyme telomerase, and thus avoid the normal limitations of cell division. Furthermore, inhibition of normal cell cycle checkpoint controls means that DNA damage, including telomere shortening, does not result in senescence or apoptosis and is instead propagated to daughter cells, accelerating the accumulation of mutations and genomic instability[17].

Whilst dysregulated proliferation is the key feature of tumour cells, virtually every aspect of intracellular and extracellular signalling is hijacked to overcome the barriers to macroscopic tumour formation. Like any cell, tumour cells require a supply of nutrients to survive and therefore angiogenesis is a key requirement for tumour size to progress beyond 1 – 2 mm[318]. Tumours secrete several factors, notably vascular endothelial growth factor (VEGF) and members of the angiopoietin family, that promote new blood vessels to form primarily by invasion and proliferation of endothelial cells from surrounding stroma[18]. Vessels may also be formed by tumour cells themselves in a process termed vascular mimicry. In contrast to normal capillary beds, tumour blood vessels are often fragile, tortuous, form arterio-venous shunts or blind-ending vessels and may exhibit sluggish or intermittent blood flow. Tumours also tend to outgrow their blood supply leading to zones of necrosis.

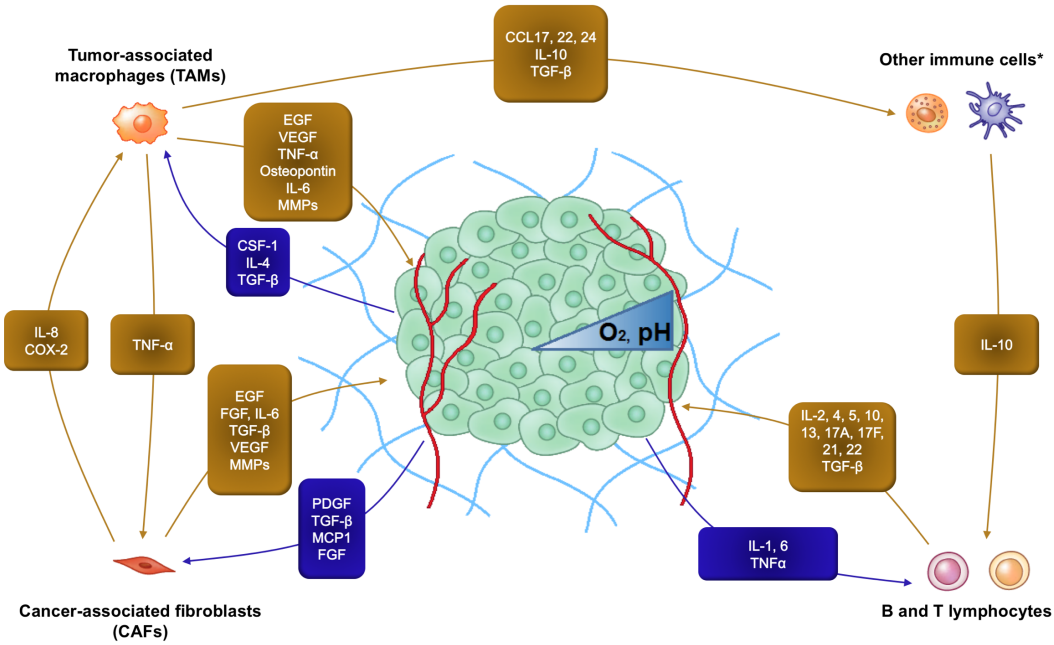

Figure 1.1. Components of the tumour microenvironment. Tumour cells (green) interact with and corrupt a range of different cell types. Disordered angiogenesis and dysregulated metabolism contribute to a hypoxic and acidic interstitial space. *Other immune cells include dendritic cells, myeloid-derived stem cells, natural killer T cells and tumour associated neutrophils. Abbreviations: IL – interleukin; PDGF – platelet-derived growth factor; MCP – monocyte chemoattractant protein; TNF – tumour necrosis factor; VEGF – vascular endothelial growth factor; FGF – fibroblast growth factor; EGF – epidermal growth factor; COX – cyclo-oxygenase; MMP- matrix metalloproteinase; CCL – chemokine ligand; LN – laminin.

The role of the immune system in cancer progression has long been recognised from observations of accelerated tumour growth in immune-suppressed mice and the propensity of tumours to arise at sites of chronic inflammation. Immune cells initially recognise tumour cells as 'non-self' and attempt to eliminate them. Certain immune cells have particular anti-tumour effects. For example, high levels of $CD4^+$ T helper 1, cytotoxic $CD8^+$ memory T cells and natural killer T cells slow growth and improve

prognosis. However, immune cells can also be converted to play, in combination with other cells - notably fibroblasts - specific roles in supporting tumour development by secreting a range of growth factors, chemokines, metabolic substrates and matrix remodelling enzymes that promote growth, angiogenesis, invasion and metastasis (Figure 1.1). The combination of tumour cells, recruited host cells and abnormal vasculature results in the formation of a self-regulating organ with a unique microenvironment and the emergence of the hallmarks of cancer (Figure 1.2)[19].

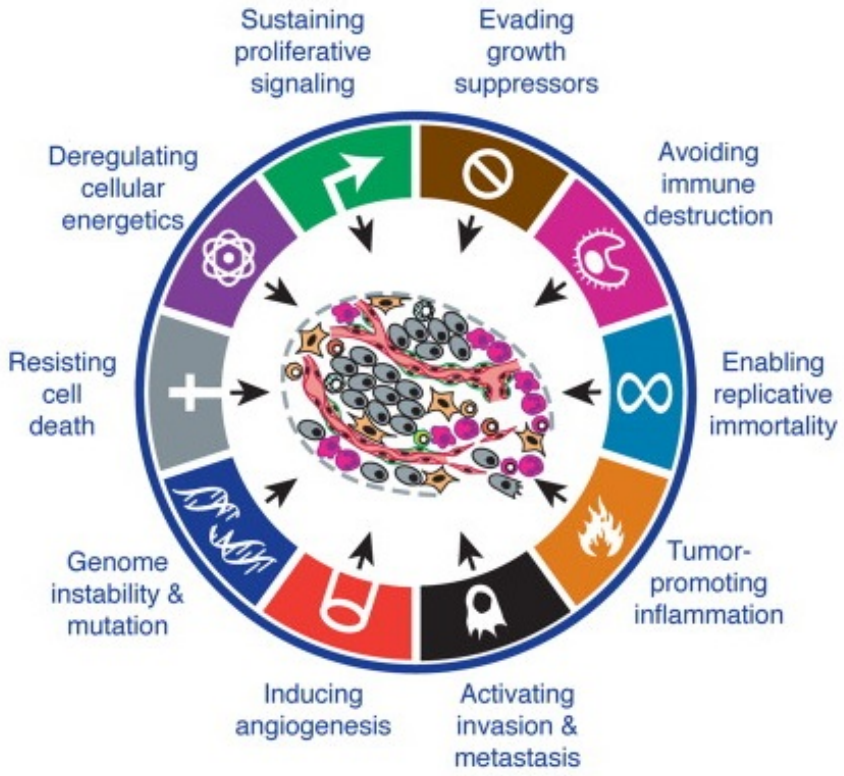

Figure 1.2. The hallmarks of cancer. Adapted from Hanahan & Weinberg 2011[19].

1.2. Tumour Metabolism

Aberrant nutrient uptake and subsequent metabolism is a feature of malignant tumours that results from the increased demand for the synthesis of proteins, nucleic acids, fatty acids and other macromolecules required for increased growth and proliferation. In the revised Hallmarks of Cancer (2011), metabolic reprogramming was

included as an “emerging hallmark”, a slightly bizarre classification given that metabolic reprogramming of tumours was first described nearly half a century prior to the discovery of the first proto-oncogene, *SRC*[19, 20]. In 1924 Otto Warburg observed that tumour cells preferentially metabolised glucose to lactate in the presence of normoxia instead of utilising the TCA cycle[21]. Warburg concluded that cancer was caused by mitochondrial dysfunction and while we now know that to be largely untrue, the Warburg Effect, or aerobic glycolysis, is observed in most tumours. In terms of bioenergetics, the Warburg Effect is highly inefficient, producing only two molecules of ATP per molecule of glucose versus approximately thirty ATP molecules if the TCA cycle and oxidative phosphorylation are utilised[22]. Consequently, tumours often consume glucose and produce lactate in large quantities, the latter being used as a substrate for the TCA cycle or exported from the cell *via* monocarboxylate transporters[23]. It is possible that the switch to aerobic glycolysis is simply a response to the fluctuating supply of oxygen from a disordered blood supply, or alternatively that it confers a proliferative advantage. Pyruvate kinase (PK) catalyses the conversion of phosphoenolpyruvate to pyruvate in the last step of glycolysis. The predominant isoform of PK found in tumours is PKM2, which exists in two forms – a dimer with low affinity for phosphoenolpyruvate and a tetramer with high affinity and high enzymatic activity. Predominance of the dimeric state results in an accumulation of upstream metabolites that can then enter other pathways including the pentose phosphate pathway (PPP), the hexosamine pathway, the serine synthesis pathway and glycogenesis, the products of which are essential for proliferation[24, 25]. As well as producing ribose-5-phosphate, required for nucleic acid synthesis, the PPP is also a key source of NADPH and reduced glutathione, required to restore the redox balance that is disrupted by increased generation of ROS in tumours[26].

As well as their importance in the generation of ATP, TCA cycle metabolites are precursors for numerous macromolecules including lipids. Almost constant intracellular levels of TCA cycle metabolites are maintained by rapid replenishment, predominantly from pyruvate and glutamine. Pyruvate can enter the TCA cycle *via* acetyl-CoA or be carboxylated to oxaloacetate and both of these pathways can be upregulated in tumours[23, 27]. Glutamine uptake is increased in many cancer cell lines and some tumours[27-29]. Glutamine contributes to TCA cycle anaplerosis predominantly by conversion to glutamate, in the reaction catalysed by glutaminase, and subsequent deamination to generate α-ketoglutarate. It also serves as an important nitrogen source for the synthesis of non-essential amino acids, nucleotide bases and glutathione[30].

1.2.1. Oncometabolites

Mutation of metabolic enzymes leading to a change in function and subsequent accumulation of metabolites at supra-physiological concentrations has been proposed recently as a trigger of tumourigenesis, as Warburg suggested nearly a century ago.

Loss of function mutations in fumarate hydratase (FH) results in accumulation of fumarate and is seen in a subset of hereditary renal cancers. Loss of succinate dehydrogenase (SDH) function and subsequent accumulation of succinate is associated with various tumours including neuroendocrine, renal, and gastrointestinal stromal tumours. Both fumarate and succinate are competitive inhibitors of the α-ketoglutarate (α-KG)-dependent dioxygenases, which include the hypoxia inducible factor (HIF) prolyl hydroxylases, ten-eleven translocation proteins (TETs) and the histone lysine demethylases. The consequent stabilisation of HIF, even in the presence of oxygen, and the methylation changes that result from the accumulation of

these metabolites have been proposed as a mechanism for tumourigenesis. Additionally, fumarate upregulates the mTOR/HIF1α pathway and the NF-KB pathway, both frequently stimulated in cancers[31, 32].

Isocitrate dehydrogenase (IDH)-1 and IDH2, the cytosolic and mitochondrial form of the enzyme respectively, are mutated in a majority of gliomas and some acute myeloid leukaemias[33, 34]. Wild-type isocitrate dehydrogenase (IDH) catalyses isocitrate decarboxylation to α-ketoglutarate (α-KG) but the most common mutation of IDH leads to a neomorphic function where it reduces α-KG to 2-hydroxyglutarate (2-HG). In normal tissues 2-HG is kept at very low levels but in IDH-mutant tissues its concentration rises to millimolar (mM) levels. By inhibition of α-KG-dependent dioxygenases, as seen with fumarate and succinate accumulation, 2-HG induces widespread methylation changes and HIF stabilisation[35, 36].

1.2.2. Control of metabolism

The control of metabolism in tumours is multi-faceted, complex and incompletely understood. The supply of metabolites is dependent on highly variable factors in tumours including proximity to blood vessels, viability of those blood vessels and the extracellular microenvironment, all of which are heterogeneous in a solid tumour. A degree of control is exerted on metabolic enzymes by the abundance of the substrate, co-factors, product and pH. Furthermore, the expression of enzymes of the key metabolic pathways is partly regulated by signalling pathways that also control proliferation and contain some of the most commonly mutated genes in cancer. Some of the common mutations that influence glucose metabolism are shown in Figure 1.3.

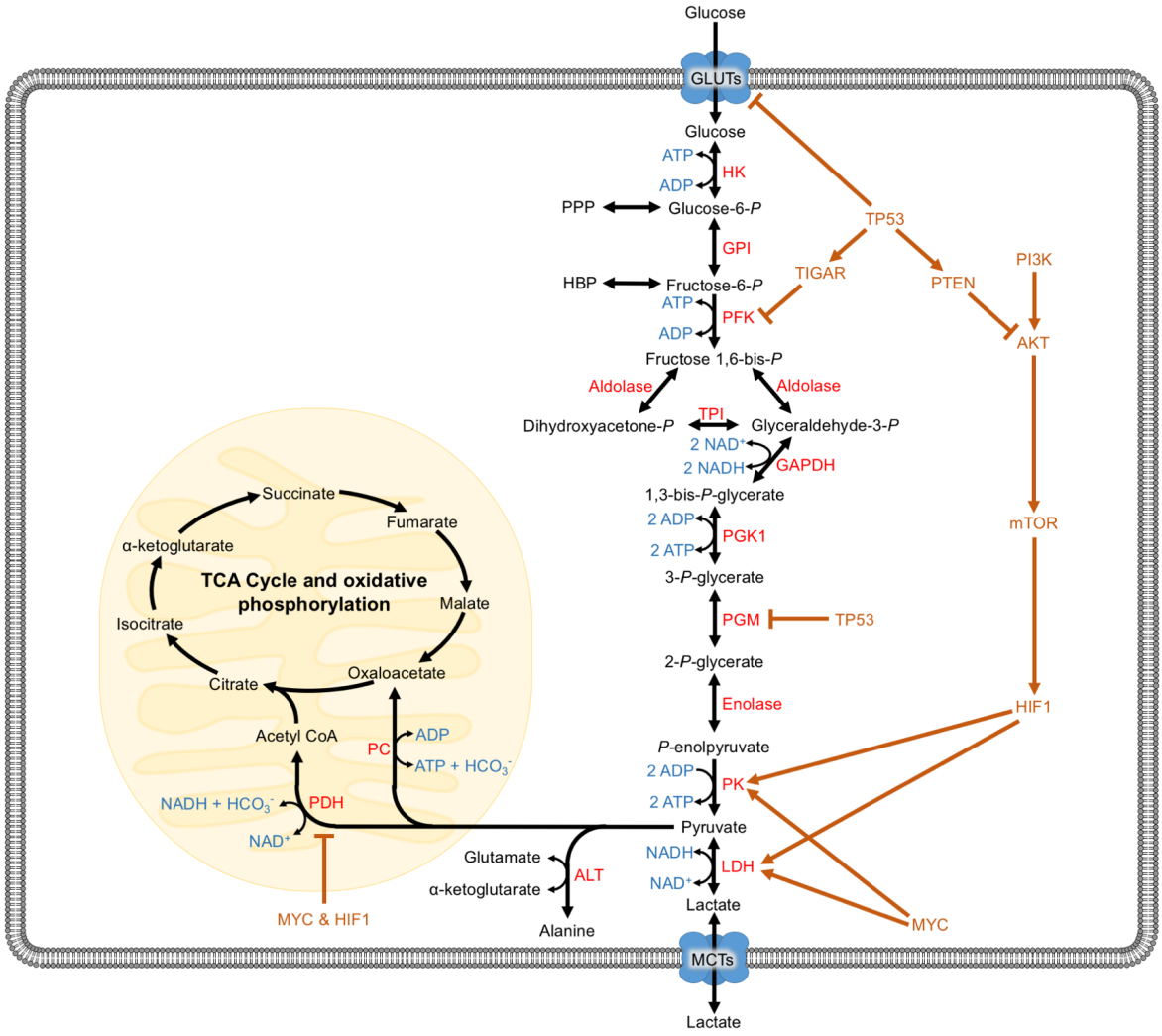

Figure 1.3. Glycolysis and some of the major regulators. Black – metabolic intermediates; red – enzymes; light blue – cofactors, by-products and redox substrates/products; orange – expression regulation: arrows indicate upregulation while flat-ends indicate down-regulation by the wild-type gene.

Mutated in >50% of human cancers, TP53 helps maintain genomic stability and regulates the expression of numerous genes responsible for cell cycle control, DNA repair and apoptosis as well as having multiple effects on cellular metabolism. By affecting multiple overlapping pathways, wild-type TP53 can both promote and down-regulate glycolysis although the overall picture appears to be one of inhibition of glycolysis and promotion of oxidative phosphorylation. The picture is complicated

further by TP53 mutation resulting in both loss of wild-type function and gain of oncogenic function in cancers[37]. For example, wild-type TP53 decreases expression of glucose transporters (GLUT) 1, 3 and 4, and phosphoglycerate mutase while inducing TP53-induced glycolysis and apoptosis regulator (TIGAR), all of which reduces glycolytic flux. TIGAR has the effect of reducing fructose-2,6-bisphosphate levels, which results in inhibition of phosphofructokinase and directs flux towards the PPP. However, mutant TP53 upregulates hexokinase 2 expression and promotes translocation of GLUT1 to the cell membrane[38, 39]. Downstream, TP53 decreases pyruvate dehydrogenase kinase expression, increasing pyruvate dehydrogenase activity and conversion of pyruvate to acetyl-CoA[40]. Oxidative phosphorylation is further elevated by wild-type TP53 upregulation of synthesis of cytochrome c oxidase 2 (SCO2) synthesis, which is required for assembly of complex IV of the electron transport chain[41].

Aberrant PI3K / AKT / mTOR pathway signalling is common in tumours, often occurring as a result of over-expression of PI3K, inactivation of PTEN, RAS mutation or growth factor receptor mutation. Activation of AKT (protein kinase B) can modulate expression of glycolytic transporters and enzymes both directly and indirectly by regulating a range of transcription factors, e.g. the forkhead box (FOX) family, and via activation of mammalian target of rapamycin (mTOR)[25]. One of the key actions of mTOR is to up-regulate hypoxia-inducible factor (HIF), even in the absence of hypoxia. HIF1 upregulates transcription of most of the glycolytic enzymes and also activates the pyruvate dehydrogenase kinases (PDKs), inhibiting pyruvate dehydrogenase and reducing pyruvate flux into the TCA cycle[25, 42, 43].

The transcription factor MYC is estimated to control the expression of around 15% of human genes in normal cells. MYC lies at the crossroads of several key

signalling pathways, and although the protein itself is rarely mutated, as a result of upstream mutations it is over-expressed in most human cancers. Rather than causing transcription of a new set of genes, it has recently become apparent that MYC accumulates at promoters across the genome, its abnormal expression in tumour cells deregulating transcription of multiple sets of genes[44, 45]. In addition to its role controlling proliferation and apoptosis, MYC exerts effects on angiogenesis, invasion, stromal remodelling and inflammation whilst also having a direct regulatory role in metabolism. It is thought that MYC induces transcription of virtually all glycolytic genes including lactate dehydrogenase A (LDH-A) and PDK1, thus promoting the production of lactate from glycolysis[25, 46, 47].

1.3. Cancer Imaging

In November 1895 the field of medical imaging was born when, quite by accident, Wilhelm Röntgen imaged the bones of his own hand, and shortly afterwards published the first x-ray of his wife's hand, whilst experimenting with a cathode ray tube. Less than a year later x-rays were first applied in cancer imaging when Franz König revealed a sarcoma of the tibia[48]. The invention of x-ray computed tomography (CT) in 1971 and magnetic resonance imaging (MRI) in 1973 revolutionised oncology as, for the first time, three-dimensional, whole body imaging permitted tumours and their metastases to be visualised[49, 50]. These techniques rapidly became, and remain, essential tools for cancer diagnosis, staging and monitoring response to treatment.

1.3.1. Imaging response to treatment

For the majority of solid tumours measurements of tumour size using CT and/or MRI is the best biomarker of response in routine clinical practice. Comparing before-

and after-treatment imaging allows patients to be classified as having a complete response, partial response, stable disease or progressive disease based on criteria such as the Response Evaluation Criteria in Solid Tumours (RECIST 1.1)[51]. However, it is evident that anatomical imaging has its limitations, particularly when assessing response to treatment. The vast heterogeneity of tumour genotypes and phenotypes means that, whilst appearing anatomically and morphologically similar, tumours may behave quite differently, including in their responses to treatment. Anatomical changes following treatment are usually delayed, repeat scans typically being performed at least 6 weeks after commencing therapy[52]. Furthermore, there are now several examples, particularly with the introduction of targeted therapies that may be cytostatic rather than cytotoxic, where no improvements were detectable by the RECIST criteria but significant clinical efficacy was demonstrated[53]. There are also regular instances where size changes are difficult to interpret, for example distinguishing tumour from fibrotic tissue following radiotherapy or chemotherapy. Pseudoprogression, whereby tumours initially increase in size in response to effective treatment, is also an increasingly common problem following the introduction of immunotherapy, the highest rates (up to 8.3%) being reported in melanoma patients treated with the anti PD-1 antibody nivolumab[54-56].

Molecular imaging techniques that report on aspects of tissue biochemistry have the potential to address some of the limitations of anatomical imaging. Following treatment biochemical changes occur prior to changes in tumour volume and therefore molecular imaging could be used to detect treatment response at earlier time points than is currently possible[57]. With the pool of targeted drug therapies slowly growing, early detection of treatment efficacy would allow patients to be rapidly switched to more effective therapeutics as necessary and avoid prolonged use of therapies that

are ineffective, costly and potentially toxic. The next sections will outline the principles of the molecular imaging techniques used in this project.

1.4. Positron Emission Tomography (PET)

Positron emission tomography is a nuclear medicine technique detecting radionuclides that decay by positron emission. Positron emission generates two high-energy photons capable of travelling through body tissues and can be detected by a PET scanner containing a ring of detectors surrounding the patient that generate an electrical signal in response to photon detection. After correction for a number of factors the signals can be reconstructed into a 3D volume where the signal intensity of each voxel is proportional to the amount of radionuclide present. Thus, when radionuclides are used to label biologically relevant molecules, the spatial distribution of their concentration can be quantitatively mapped[58].

1.4.1. Principles of PET

Nuclei with an unequal number of protons or neutrons are unstable and prone to radioactive decay. Nuclei with an excess of protons may decay by positron emission (β^+ decay), whereby a proton is converted into a neutron and a positron (β^+ - the antiparticle of an electron with the same mass but opposite charge) and an electron neutrino (ν_e) are ejected from the nucleus. Fluorine-18 (^{18}F) decays to stable oxygen-18:

$$^{18}_{9}F \longrightarrow {}^{18}_{8}O + \beta^+ + \nu_e$$

Following ejection from the nucleus, the positron follows a tortuous course while rapidly losing kinetic energy by Coulomb interactions with electrons. Upon reaching thermal energy, the positron combines with an electron and annihilates,

simultaneously emitting two gamma photons in opposite directions (very close to 180º apart). As the positron is almost at rest when annihilation occurs, the energy emitted is proportional to the mass of the positron and the electron it annihilates with and equates to two 511 keV gamma photons which are able to pass through tissues to be detected externally. A line of response drawn between simultaneously detected photons (<18 ns apart) passes through the point of annihilation (Figure 1.4). To determine the point along the line of response where an annihilation event occurred, computed tomography algorithms infer the concentration of radioactivity in each voxel based on measurements at different angles through the object, a process that typically requires $>10^6$ coincident events for each PET scan. In modern clinical scanners time-of-flight measurements can be used to localise further the annihilation event along the line of response[58]. Numerous other factors are corrected for during image reconstruction, including decay, scatter, dead time, attenuation and random events. Most modern scanners also incorporate a computed tomography (CT) scan, which is used for anatomical co-registration and attenuation correction[59].

1.4.2. 2-([^{18}F]fluoro)-2-deoxy-D-glucose ([^{18}F]FDG)-PET

^{18}F is by far the most widely used PET radionuclide due to its favourable half-life (Table 1.1), decay to a stable product and ability to form strong covalent or ionic bonds with most elements, especially carbon[60]. [^{18}F]FDG, a glucose molecule in which the 2' hydroxyl group has been substituted with ^{18}F, was the first tracer to be used in humans and remains the most common tracer in clinical use today. The metabolism of [^{18}F]FDG closely mimics the initial metabolism of glucose. After injection into the circulation [^{18}F]FDG enters cells *via* facilitative glucose transporters (GLUTs) and is renally excreted. Upon entering a cell [^{18}F]FDG is phosphorylated to [^{18}F]FDG-6-

phosphate which cannot be isomerised by glucose-6-phosphate isomerase and therefore does not undergo further steps of glycolysis. [^{18}F]FDG-6-phosphate is trapped intracellularly and due to the low rate of de-phosphorylation in most cells, gradual accumulation of ^{18}F label in glucose-avid tissues can be visualised as areas of increased uptake on PET scans. PET is an extremely sensitive technique and tracers are administered in nanomole quantities, meaning that [^{18}F]FDG does not have an inhibitory effect on metabolism[61].

Radionuclide	Half-life (min)	Positron Energy (MeV)	Positron Range (mm)	β^+ Branching Fraction
^{11}C	20.3	0.96	1.1	1
^{13}N	9.97	1.19	1.4	1
^{15}O	2.03	1.70	1.5	1
^{18}F	109.8	0.64	1.0	0.97
^{68}Ga	67.72	1.90	2.9	0.89

Table 1.1. Commonly used PET radionuclides, their half-lives, positron energy, positron range in water and β^+ branching fraction. The positron range is the distance travelled between positron emission and annihilation and is defined by the positron energy, determined in turn by the difference in atomic mass between the parent atom and daughter atom. The β^+ branching fraction refers to the proportion of decay events that result in the emission of a β^+, with electron capture being the other method of decay[58, 62].

Most tumours are highly glycolytic and uptake of [^{18}F]FDG has been used as a marker of increased glucose uptake to screen, diagnose, stage and detect response to treatment in cancer[63]. Many of the fourteen known GLUTs are over-expressed in various human cancers, whereas of the four mammalian isoforms of hexokinase (HK), the over-expression of HK2 is seen most frequently in tumours[64-66]. However, studies

attempting to correlate [^{18}F]FDG uptake and GLUT and/or HK2 expression are inconsistent, suggesting the determinant of [^{18}F]FDG uptake rate is, like so many aspects of biology, complex and multi-factorial[67-73].

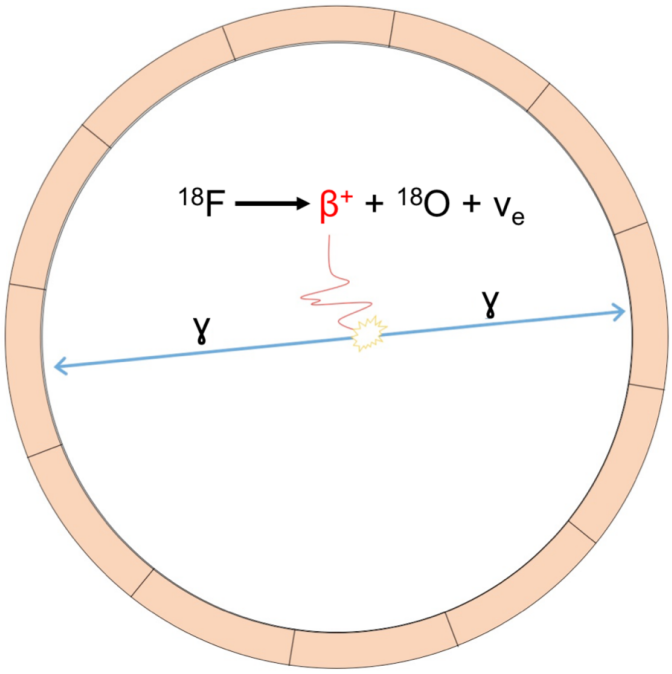

Figure 1.4. The principle of positron emission tomography with ^{18}F. ^{18}F undergoes spontaneous decay to ^{18}O, usually emitting a positron (red) and a neutrino. The positron travels a short distance before annihilation with an electron (yellow). This emits two gamma photons (blue lines) at approximately 180° with respect to each other. A line is drawn between photons arriving at opposite detector rings coincidentally (the line of response) to spatially reconstruct the annihilation event.

The advantages of [^{18}F]FDG-PET include its high sensitivity and the capability of whole-body image acquisition. It is limited by the relatively low resolution that can be achieved in clinical scanners (~5 mm)[74], lack of metabolite specificity, reporting only on the first two steps of glycolysis (uptake and phosphorylation) and by the high

background uptake from normal, glucose-avid tissues that can result in false-positive tumour imaging[75].

1.4.3. [^{18}F]FDG-PET imaging of treatment response

Positive correlation between [^{18}F]FDG uptake and the number of viable tumour cells has been reported and [^{18}F]FDG-PET has successfully detected treatment response and/or recurrence in many cancers in patients, in most cases improving on anatomical imaging for the determination of pathological response[76-80]. In certain cancers - notably lymphoma, oesophageal cancer and gastro-intestinal stromal tumours (GISTs) - the outcome of post-treatment [^{18}F]FDG-PET imaging is used to inform patient management[81, 82]. In GISTs treated with imatinib, a BCR-ABL tyrosine kinase inhibitor, and lymphomas treated with cytotoxic chemotherapy, a reduction in [^{18}F]FDG uptake has been observed days after initiation of therapy and months before changes in tumour size[83, 84]. Furthermore, there is an increasing body of evidence that suggests patients with scans that normalise rapidly after treatment have a better outcome, therefore earlier assessment of tumours post-treatment would be beneficial[78, 79, 85]. Interim PET-CT, after one or two cycles of chemotherapy, has become routine to monitor some subtypes of lymphoma[86].

However, concerns that early ^{18}FDG-PET scans remain inaccurate prognostic indicators have limited its use in prediction of early treatment response. Much of this concern is due to the metabolic “flare” effect, a transient increase in [^{18}F]FDG uptake seen after treatment. This has been largely attributed to inflammatory cell infiltration and activation following tumour cell death[87, 88]. Additionally, breast cancer patients responding to tamoxifen have been shown to have higher [^{18}F]FDG uptake in the first two weeks after initiation of therapy relative to non-responders. This was attributed to

oestrogen receptor modulation by tamoxifen resulting in a transient upregulation of glycolysis[89].

1.5. Nuclear magnetic resonance and magnetic resonance imaging

Nuclear magnetic resonance (NMR) is the phenomenon of nuclei in a magnetic field absorbing and emitting electromagnetic radiation, the discovery of which led to Felix Bloch and Edward Purcell sharing the 1952 Nobel Prize in Physics[90]. Nuclei that do not have even mass and atomic numbers, along with other elementary particles, e.g. electrons, possess an intrinsic angular momentum known as spin. The nuclei of interest here, namely ^{1}H and ^{13}C, are examples of spin ½ systems and in the presence of an external magnetic field (B_0) their nuclei populate two quantized energy levels. Spins in the lower energy level correspond to magnetic moments that align parallel with B_0 while spins in the higher energy level align anti-parallel with B_0 (Figure 1.5)[91, 92]. Spins precess around B_0 at the Larmor frequency (ω_0) given by:

$$\omega_0 = \gamma B_0$$

where γ is the gyromagnetic ratio, a constant for each nucleus. At thermal equilibrium the number of spins in the lower energy level slightly outnumber those in the higher energy level. The difference in energy between the two levels is given by the equation (h = Planck's constant; v = frequency):

$$\Delta E = hv$$

Nuclei are able to transition between energy levels if exactly ΔE is applied to them. In NMR this is achieved by applying a radiofrequency (RF) oscillating magnetic field at the resonant frequency. Nuclei absorb the energy which induces flipping between energy levels. Due to the slight predominance of nuclei in the lower energy state, the net result of an RF pulse is to increase the number of nuclei occupying the

higher energy state. The application of this oscillating magnetic field in the form of a resonant frequency pulse perpendicular to B_0 flips the net magnetisation into the x-y plane (Figure 1.6). Precession in the x-y plane induces a voltage in a receiver coil that oscillates at the Larmor frequency and produces a free induction decay (FID). The FID is a time-domain signal comprising all of the excited frequencies. After acquisition the signal is digitised and Fourier transform converts the FID into a frequency domain signal[91, 92].

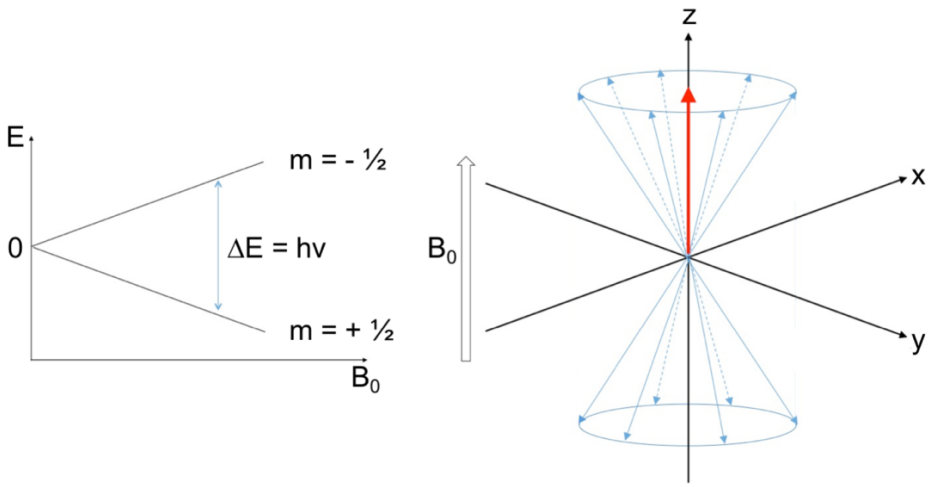

Figure 1.5. Energy levels of a spin ½ system (left) and spin distributions in a magnetic field (right). Spins align with the external magnetic field (B_0) with a slight majority of spins in the lower energy level, parallel to B_0. This results in a net magnetisation vector parallel to B_0.

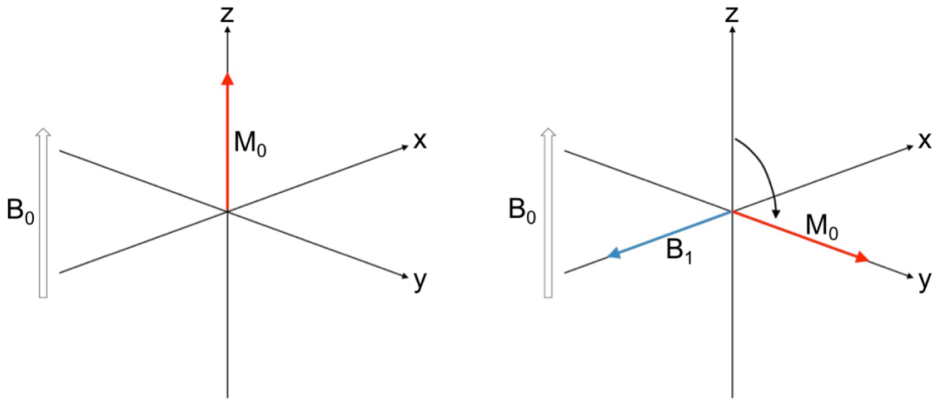

Figure 1.6. Rotation of the net magnetisation vector (M_0) after the application of a 90° pulse. At equilibrium the net magnetisation vector (red arrow) is parallel to B_0

(left). An RF pulse along the x-axis (B_1) (blue arrow) at the Larmor frequency rotates the net magnetisation vector in the y- – z-axis (right). The angle of rotation is dependent on the amplitude and duration of B_1.

1.5.1. Signal decay

After the application of an RF pulse the system gradually returns to thermal equilibrium in a process known as relaxation. Spin-lattice relaxation describes the exponential return of the net magnetisation vector toward its thermal equilibrium value. In quantum terms this occurs because there is a net redistribution of spins from the higher energy state to the lower energy state. The spin-lattice relaxation time, T_1, is defined as the time taken for the net magnetisation vector to return to 63% of its thermal equilibrium value. This occurs by transferring energy to the surrounding molecular environment. Spin-spin relaxation describes relaxation in the x-y plane and the spin-spin relaxation time, T_2, is the time take for the transverse magnetisation to decay to 37% of its initial value. Following an RF pulse, all spins are in phase. Due to the interactions between spins they dephase, resulting in an exponential reduction in the magnetisation vector in the x-y plane. In biological tissues T_2 relaxation occurs at a much faster rate than T_1 relaxation[92].

1.5.2. Magnetic Resonance Imaging (MRI)

The abundance of tissue water protons in biological tissues (approximately 60-80 M) and the high gyromagnetic ratio of the proton permits magnetic resonance imaging at resolutions as high as 50 μm in *in vivo* pre-clinical studies[93, 94]. To produce images instead of spectra, magnetic field gradients are applied that change the magnetic field across an imaging plane. These gradients alter the magnetic field so

that spins can be localised according to their resonance frequency. Gradients can be applied in all three planes. Slice selection is achieved by applying a gradient perpendicular to the plane of interest. All nuclei in a slice experience the same change in magnetic field and can be selectively excited by the simultaneous application of a frequency-selective RF pulse. Phase encoding and frequency encoding gradients are used for spatial localisation in the other two dimensions[92]. In ^{1}H magnetic resonance imaging (MRI) the different rates of T_1 and T_2 relaxation in different molecular environments are exploited to produce contrast between different tissues. Additionally, paramagnetic contrast agents e.g. gadolinium can be introduced that remain in certain fluid compartments and enhance contrast by shortening T_1 and T_2[95].

1.5.3. Magnetic Resonance Spectroscopy (MRS)

Depending on the immediate electronic environment of the nucleus the resonant frequency changes by a few kHz. Therefore, nuclei in different molecules resonate at slightly different frequencies, an effect known as chemical shift. The frequency of the chemical shift can be expressed in parts per million (ppm) of the spectrometer operating frequency, where the chemical shift of each molecule is referenced to a standard[92]. ^{1}H magnetic resonance spectroscopy (MRS) can differentiate between steady-state tissue metabolites in the millimolar range *in vivo*, but the inherent insensitivity of NMR limits the spatial and temporal resolution of scans to around 1 cm^3 and 5 – 10 min, respectively[96-98].

Metabolic fluxes can be studied by introduction of isotopically labelled substrates[99]. ^{13}C represents only 1.1% of all carbon and has been used to label numerous substrates for *in vivo* studies of metabolic fluxes[100]. Signal-to-noise ratio (SNR) can be increased by using higher field strengths to increase the difference

between spin populations and by indirect detection *via* spin-coupled protons. However, the signal is still too limited to permit imaging[96].

1.5.4. Dissolution Dynamic Nuclear Polarisation (DNP)

A further transient increase in NMR signal by >10^4 is made possible by dynamic nuclear polarisation (DNP)[101]. Although it can in principle be used with any NMR-active nucleus, the majority of studies have been performed with ^{13}C-labelled molecules because of their relatively long polarisation lifetime and the possibility of measuring metabolic fluxes with ^{13}C-labelled cell metabolites. In DNP the substrate to be polarised is mixed with a stable radical (a source of unpaired electrons). The sample is then cooled to ~1 K to form a solid and placed in a magnetic field, typically >3 Tesla. For DNP to be effective the radical must be distributed homogeneously throughout the sample, therefore the sample must form a glass and not crystallise. Depending on the substrate it may be necessary to add a solvent such as DMSO to achieve this. At ~1 K and high magnetic field the electron spins are nearly 100% polarised. Microwave irradiation at the resonant frequency of the electron partly transfers the electron spin polarisation to the nuclei[96, 101-103]. The addition of gadolinium (Gd^{3+}) ions shortens the electron T_1 spin-lattice relaxation time and can improve sample polarisation by up to 300%[104].

At room temperature the nuclear T_1 in the presence of the radical is very short. In 2003 the dissolution step was invented that allows a sample to be rapidly heated to room temperature. A buffered solvent, heated and pressurised to ~180 °C and 10 bar, flushes the sample out of the hyperpolariser[101]. The procedure from the start of dissolution to injection into a subject can be comfortably accomplished in <15s in pre-clinical studies. Once heated to room temperature the polarisation starts to decay at a

rate dictated by the T_1 of the nucleus. The hyperpolarisation afforded by DNP has permitted *in vivo* measurement of metabolic fluxes by spectroscopy and spectroscopic imaging. For example, [1-^{13}C]pyruvate has a T_1 of around 40 s at 9.4 T and >60% polarisation has been achieved using custom-built high-field polarisers, meaning the signal can last >3 min *in vivo*, permitting the measurement of [1-^{13}C]lactate, 1[^{13}C]alanine, and ^{13}C-bicarbonate, the immediate products of its metabolism[105-108].

1.6. Investigating cancer metabolism with hyperpolarised ^{13}C-labelled substrates

Numerous hyperpolarised ^{13}C-labelled substrates have been used in pre-clinical studies of cancer metabolism, although limited levels of polarisation and short T_1s in the liquid state make few clinically translatable (Table 1.2 and Figure 1.7)[109]. Owing to its position in the glycolytic pathway and favourable polarisation properties, [1-^{13}C]pyruvate has been the most commonly used substrate and it has also been used in clinical studies[110, 111]. The ability to non-invasively image real-time metabolic fluxes has the potential to impact on many aspects of cancer management from screening, diagnosis and phenotyping to prognostication. However, to translate to routine use in clinical oncology, hyperpolarised MRI must provide novel information that influences clinical management. Here we will discuss the recent applications of hyperpolarised MRI in oncology.

1.6.1. Screening, diagnosis and disease progression

Financial and time constraints limit population-based screening with any cross-sectional imaging technique, let alone hyperpolarised MRI. However, it may be feasible for highly stratified groups such as patients with hereditary cancer syndromes,

especially in conjunction with pre-screening strategies based upon new, more sensitive and specific circulating biomarkers. Patients identified by these methods could then potentially undergo multi-modality molecular imaging to confirm the diagnosis, improve staging and identify potential therapeutic targets.

Metabolite	T_1 (s)	Polarisation	Measurable products	Measures	Refs
[1-^{13}C]pyruvate	40 (9.4 T)	>60%	[1-^{13}C]lactate ^{13}C-bicarbonate [1-^{13}C]alanine	LDH, PDH and ALT activity, MCT expression, NADH availability	105, 107
[1,4-$^{13}C_2$]fumarate	24 (9.4 T)	26 – 35%	[1,4-$^{13}C_2$]malate	Necrosis – leakage of fumarase from necrotic cells increases conversion of [1,4-$^{13}C_2$]fumarate to [1,4-$^{13}C_2$]malate	112
[1-^{13}C]lactate	45 (3 T)	7%	[1-^{13}C]pyruvate [1-^{13}C]alanine ^{13}C-bicarbonate	MCT expression, LDH, PDH and ALT activity, NAD^+ availability,	113
[1-^{13}C]alanine	66 (3 T)	25	[1-^{13}C]pyruvate [1-^{13}C]lactate	NADH availability, LDH and ALT expression	114
[1-^{13}C]α-ketoglutarate	52 (3 T)	16.3 ± 3%	[1-^{13}C]2-hydroxyglutarate	Mutant IDH expression, NADPH availability	115
[1-^{13}C]glutamine	31 (1 T)	34.7 ±7%	[1-^{13}C]2-hydroxyglutarate	Mutant IDH expression	116
[5-^{13}C]glutamine	16 (9.4 T)	5%	[5-^{13}C]glutamate	Glutaminase activity, glutamine transport	117
[1-^{13}C]glutamate	34 (9.4 T)	28%	[1-^{13}C]α-ketoglutarate	ALT activity, pyruvate availability	118
[U-^{2}H, U-^{13}C]glucose	9 (7 T)	15%	[1-^{13}C]lactate [1-^{13}C]6-phosphogluconate [2-^{13}C]dihydroxyacetone phosphate ^{13}C-bicarbonate	Glycolysis	119
ɣ-glutamyl-[1-^{13}C]glycine	30 (9.4 T)	5.4%	[1-^{13}C]glycine	GGT activity	120

Table 1.2. The properties of some hyperpolarised substrates that have been used in cancer studies. The numbers in parentheses after the T_1 values are the field strengths at which these relaxation times were measured. Abbreviations: MCT – monocarboxylate transporter; LDH – lactate dehydrogenase; PDH – pyruvate dehydrogenase; ALT – alanine transaminase; IDH – isocitrate dehydrogenase; GGT – ɣ-glutamyltransferase.

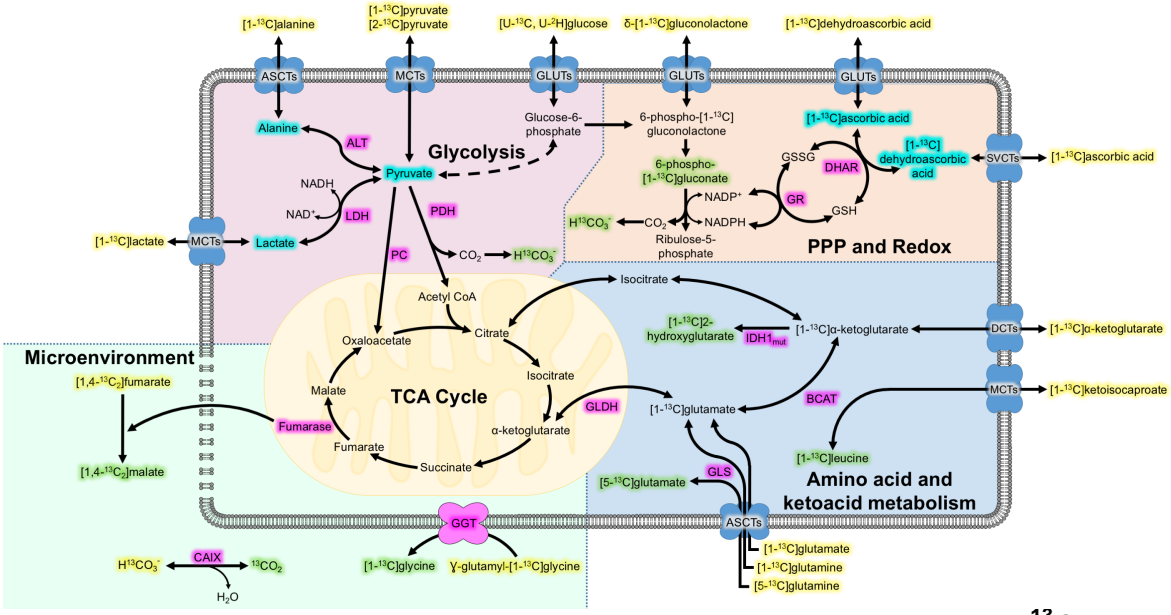

Figure 1.7. Metabolic processes targeted with hyperpolarised ^{13}C-labelled metabolites. Colour coding: pink – enzymes; yellow – hyperpolarised ^{13}C-labelled substrates; green – measurable hyperpolarised ^{13}C-labeled products; cyan – hyperpolarised ^{13}C labelled substrates and measurable products (depending on the substrate injected). Abbreviations: ALT – alanine transaminase; ASCTs – alanine, serine, cysteine transporters (there are also several other transporters that can transport glutamine into cells); BCAT – branched-chain amino acid aminotransferase; CAIX – carbonic anhydrase 9; DCTs – dicarboxylate transporters; DHAR – dehydroascorbate reductase; GGT – ɣ-glutamyltransferase; GLDH – glutamate dehydrogenase; GLS – glutaminase; GLUTs – glucose transporters; GR – glutathione reductase; GSH – glutathione; GSSG – glutathione disulfide; IDH – isocitrate dehydrogenase; LDH – lactate dehydrogenase; MCTs – monocarboxylate transporters; PC – pyruvate carboxylase; PDH – pyruvate dehydrogenase; PPP – pentose phosphate pathway; SVCTs – sodium-ascorbate co-transporters.

In prostate cancer there is a requirement for new approaches to determine tumour aggressiveness. 30-70% of men over sixty are estimated to have prostate cancer but the vast majority require no treatment[121]. However, 30% of patients defined as being low-risk actually harbour higher-grade tumours that would benefit from early treatment[122]. Multi-parametric ^{1}H MRI has As four out of five cases present with localised disease, imaging with hyperpolarised [1-^{13}C]pyruvate is a potentially useful tool for determining the aggressiveness of these tumours[123]. This was illustrated in the first-in-man study in which, following injection of hyperpolarised [1-^{13}C]pyruvate, an elevated [1-^{13}C]lactate/[1-^{13}C]pyruvate ratio was observed in tumour regions. in one patient a biopsy-proven tumour was identified by hyperpolarised imaging but not by multi-parametric ^{1}H-MRI[111].

In a study using a transgenic mouse model of prostate adenocarcinoma (TRAMP), co-polarisation of [1-^{13}C]pyruvate and ^{13}C-urea (an agent for imaging perfusion) showed both to be capable of differentiating high- and low-grade tumours, with high-grade tumours showing increased lactate labelling and reduced perfusion but higher vascular permeability and ^{13}C urea washout[124].

Pancreatic cancer has a >90% mortality within 5 years of diagnosis and survival prospects that are dependent on early detection and surgery[123]. The injection of hyperpolarised [1-^{13}C]pyruvate into genetically engineered mouse models of pancreatic ductal adenocarcinoma showed the [1-^{13}C]alanine/[1-^{13}C]lactate ratio decreased with disease progression[106]. If hyperpolarised [1-^{13}C]pyruvate can differentiate neoplastic lesions from inflammatory and pre-neoplastic lesions in patients, it could have a significant impact on patient management.

Similarly, hepatocellular carcinoma has a mortality rate in excess of 95%, making it the second most common cause of cancer mortality worldwide. However,

localised tumours suitable for resection or ablation have a good prognosis[125]. Differentiation of small malignant tumours from benign tumours and cirrhotic liver is challenging but may be aided by metabolic imaging. In hepatoma cells glutamine uptake is 10-30 fold greater than in normal hepatocytes[126-128]. The hydrolysis of hyperpolarised [5-^{13}C]glutamine to [5-^{13}C]glutamate differentiated *in vivo* rat hepatomas from normal liver[117, 129]. However, the short T_1 and poor polarisation of [5-^{13}C]glutamine may ultimately limit clinical translation[130].

1.6.2. Tumour phenotyping

Metabolic phenotyping could dictate patient management and improve prognostication. Several new approaches to tumour metabolic phenotyping with hyperpolarised substrates are discussed below.

1.6.2.1. Isocitrate dehydrogenase (IDH)

Wild-type IDH catalyses oxidative decarboxylation of isocitrate to produce α-ketoglutarate (α-KG). As noted earlier, the most common IDH mutation promotes the reduction of α-KG to the oncometabolite D-2-hydroxyglutarate (2-HG)[36]. IDH1, the cytosolic isoform, is mutated in >70% of low-grade gliomas[33] and non-invasive determination of IDH1 mutational status would change the approach to surgical resection. [1-^{13}C]2-HG has been observed in tumour models *in vivo* following injection of hyperpolarised [1-^{13}C]α-KG and [1-^{13}C]glutamine[115, 116]. Mutations in IDH1 have also been associated with down-regulation of PDH activity and reduced [5-^{13}C]glutamate labelling following injection of hyperpolarised [2-^{13}C]pyruvate has been demonstrated[131, 132].

1.6.2.2. Branched-chain aminotransferase (BCAT)

Intracellular levels of branched-chain amino acids (BCAAs) are tightly controlled, with defective catabolic pathways leading to severe neurological damage and death if untreated. The first step in BCAA catabolism is the transfer of an α-amino group to α-KG catalysed by branched-chain aminotransferase (BCAT) that, under the control of MYC, is over-expressed in a number of cancers correlating with higher rates of proliferation and poorer prognosis[133-135]. In glioblastoma wild-type IDH promotes upregulation of BCAT1. Mutant IDH not only produces 2-HG and depletes the α-KG pool but also down-regulates BCAT1 by hypermethylation of its main promoter region[135]. Hyperpolarised α-keto-[1-^{13}C]isocaproate (KIC) is transaminated to [1-^{13}C]leucine in the reversal of BCAA catabolism and leucine has been detected in EL4 murine T-cell lymphoma tumours[136]. Furthermore, transported by MCTs, KIC crosses the blood brain barrier and is detectable in normal brain[137]. With favourable polarisation and T_1 relaxation parameters, hyperpolarised KIC imaging of BCAT function has the potential to differentiate between high and low grade glioma and to phenotype other solid tumours.

1.6.2.3. ɣ-glutamyl-transpeptidase (GGT)

GGT is bound to the outer aspect of the plasma membrane and catalyses degradation of extracellular glutathione to its constituent amino acids (glutamate, cysteine and glycine), which can then be transported intracellularly for glutathione synthesis. GGT is over-expressed in a variety of tumours where it may play a role in progression, invasion and drug resistance[138]. Cleavage of hyperpolarised ɣ-glutamyl-[1-^{13}C]glycine to [1-^{13}C]glycine, catalysed by GGT, has been measured in normal rat

organs[120]. The next step will be to determine whether tumour over-expression of GGT can be detected.

1.6.3. Imaging pH

The acidic extracellular environment of tumours results from excessive lactate and CO_2 production from upregulated metabolic pathways, dysregulated buffering systems and poor perfusion (Figure 1.1)[139]. In addition to cancer, clinical imaging of pH could have implications for detection and treatment response monitoring in infectious, inflammatory and ischemic diseases. Injection of hyperpolarised ^{13}C-bicarbonate results in the production of $^{13}CO_2$ in the reaction catalysed by carbonic anhydrase. From the $H^{13}CO_3^-/^{13}CO_2$ ratio the extracellular pH and carbonic anhydrase activity can be determined, as demonstrated in mouse models of lymphoma and colorectal cancer [140, 141].

Several hyperpolarised probes that exhibit pH-dependent chemical shifts have also been proposed. $^{15}N_2$-imidazole and several ^{15}N-pyridine derivatives have been hyperpolarised and used *in vitro*, with chemical shifts of up to 60 ppm per pH unit [142, 143]. More recently [1,5-^{13}C]zymonic acid was discovered as a contaminant of pyruvic acid and found to have a pH sensitive, but temperature and concentration independent, chemical shift of approximately 3 p.p.m. per pH unit. *In vivo* imaging of multiple tissues including tumours in rats, with nominal in-plane resolution of 3.75 mm, returned similar pH values to those measured by ^{31}P MRS and a tissue pH electrode[144].

1.6.4. Imaging redox status

Oxidative stress plays a key role in carcinogenesis by directly causing DNA damage and cancers generally have elevated levels of reactive oxygen species (ROS)

which promote tumour development and resistance to therapy [145]. Homeostatic mechanisms respond to increased ROS levels by increasing antioxidant production and several hyperpolarised probes have been used to monitor these regulatory mechanisms. For example, [1-^{13}C]alanine has been used to measure the lactate/pyruvate ratio as a surrogate for the NAD^+/NADH ratio[114]. The PPP also produces NADPH, required by glutathione reductase to maintain levels of reduced glutathione, a key anti-oxidant. Flux through the PPP has been estimated in tumours by measuring [U-^{2}H, U-^{13}C]glucose conversion to 6-phosphogluconate, a PPP intermediate, and recently the production of $H^{13}CO_3^-$ was detected in mouse liver following injection of δ-[1-^{13}C]gluconolactone[146, 147].

In addition to being an important enzyme co-factor, ascorbic acid (AA) can also be oxidised to dehydroascorbic acid (DHA) to reduce oxidative stress. DHA can then be reduced back to AA *via* glutathione or NADPH-dependent reactions. Hyperpolarised [1-^{13}C]dehydroascorbic acid and measurement of its reduction to [1-^{13}C]ascorbic acid has been used to probe intracellular redox status in a number of animal models of cancer [148].

1.6.5. Technical developments

The transient nature of hyperpolarisation limits its use to metabolic events occurring on a timescale of seconds to minutes. Furthermore, each excitation required to produce a spectrum or image results in further depletion of the hyperpolarisation, a significant factor in the design of pulse sequences. Recent 3D imaging sequences have reported nominal spatial resolutions in lactate and pyruvate images of ≤0.003 cm^3, and temporal resolutions <2 s[149, 150]. Initial signal availability has been enhanced by new polarisers and improved injection protocols[102, 105]. Prolongation of the

polarisation lifetime has been achieved by removal of the radical[151, 152]. Provided the sample remains at low temperature and in a relatively high magnetic field, T_1s of greater than 20 h are possible[151]. This would permit centralised hyperpolarisation of substrates followed by transport to multiple locations for clinical use, in a similar fashion to ^{18}F PET tracers, dispensing with the requirement for a hyperpolariser in close proximity to the MRI scanner.

Transferring polarisation from hyperpolarised ^{13}C nuclei to spin-coupled ^{1}H nuclei can be used to further enhance signal detection. Dynamic ^{1}H imaging of lactate methyl protons following injection of [1-^{13}C]pyruvate was recently demonstrated *in vivo*[153]. The resulting signal enhancements are likely to be greater at the lower magnetic field strengths used in the clinic.

1.6.6. Imaging treatment response using hyperpolarised ^{13}C-labelled substrates

Using hyperpolarised ^{13}C-labelled substrates to detect treatment response has several potential benefits over anatomical imaging and PET methods. First, the ability to estimate the rate of a metabolic reaction rather than simply measuring tracer accumulation may improve sensitivity and specificity to early post-therapy changes. Second, several hyperpolarised substrates can be used simultaneously or sequentially allowing multiple metabolic processes to be followed[124]. This is only possible with PET using radionuclides with different half-lives and requires dynamic imaging or multiple static acquisitions. Finally, for patient studies it is desirable to avoid repeated exposure to ionising radiation. Despite the complete lack of evidence of health effects, decades of radiation policy to the contrary has left many clinicians and patients irreparably distrustful of repeated medical radiation exposure[154, 155].

So far hyperpolarised [1-^{13}C]pyruvate has been the most thoroughly investigated hyperpolarised substrate for treatment response monitoring. In animal models chemotherapy and radiotherapy have been observed to alter hyperpolarised [1-^{13}C]pyruvate metabolism, usually leading to a decrease in lactate production (Table 1.3). Several methods have been used to quantify the exchange of labelled pyruvate and lactate, most frequently measuring the apparent forward reaction rate constant, k_{pl}[107]. The [1-^{13}C]lactate/[1-^{13}C]pyruvate area-under-the-curve ratio, which avoids compartmental modelling, has also been widely used and shown to correlate with k_{pl}[156].

A range of mechanisms, often co-existing, have been proposed to explain the decrease in pyruvate to lactate exchange. These include decreased LDH expression [157-160], apoptosis-induced PARP activation with subsequent depletion of the NADH pool [107, 112, 161] and decreased cellularity and size of the exchangeable lactate pool [107, 159], decreased expression of MCTs [159, 160, 162, 163] and decreased pyruvate kinase M2 (PKM2) expression (which leads to a decrease in size of the lactate pool)[158, 164].

Detection of treatment response has been reported in a total of four prostate cancer patients undergoing androgen deprivation therapy[110, 165]. After six weeks of therapy there were only small anatomical changes visible on ^{1}H MRI but hyperpolarised [1-^{13}C]lactate was virtually undetectable in responding patients. Perhaps more significantly, the production of [1-^{13}C]lactate continued to increase in a non-responding patient[165]. Whilst these are useful proof-of-principle examples, it should be noted that there is little scope for improving treatment response monitoring in prostate cancer where a combination of PSA and multiparametric ^{1}H MRI is already effective surveillance[166]. Indeed, in these four patients, changes in hyperpolarised [1-^{13}C]pyruvate metabolism correlated with changes in PSA level[110, 165].

Tumour model	Therapeutic	Metric	Reference
EL4 murine lymphoma	Etoposide	Apparent k_{pl}	69, 107
EL4 murine lymphoma	Combretastatin-A4-phosphate	Apparent k_{pl}	167
LoVo and HT-29 colorectal adenocarcinoma	Bevacizumab	Apparent k_{pl}	168
MDA-MB-231 triple-negative breast cancer	Doxorubicin	Apparent k_{pl}	161
C6-glioma	Whole brain irradiation (15 Gy)	Apparent k_{pl}	169
GS-2 glioblastoma	Everolimus	[1-13C]lactate/pyruvate ratio	170
C6-glioma	B20.4.1.1 (anti-VEGF mAb)	[1-^{13}C]lactate/bicarbonate ratio	171
C3H mouse mammary tumor	Combretastatin-A4-phosphate	[1-^{13}C]lactate/bicarbonate ratio	172
SKOV3 ovarian cancer	Pazopanib	[1-^{13}C]lactate/(lactate + pyruvate ratio)	173
SCCVII squamous cell carcinoma, HT-29 colorectal adenocarcinoma	Irradiation (10 Gy, and 10 Gy x 3)	[1-^{13}C]lactate:pyruvate ratio	159
SCCVII, MiaPaCa-2 human pancreatic tumor xenografts	Sunitinib	[1-^{13}C]lactate/pyruvate ratio and [1-^{13}C]lactate/total ^{13}C	174
U-HTH83 anaplastic thyroid carcinoma	Irradiation (5 Gy)	Apparent k_{pl}	175
C6-glioma	Dichloroacetate	[1-^{13}C]lactate/bicarbonate ratio	176
MDA-MB-231	Irradiation (16 Gy)	[1-^{13}C]lactate/pyruvate ratio	177
McA-RH7777 hepatocellular carcinoma	Transarterial embolisation	Apparent k_{pl}	178

Table 1.3. *In vivo* pre-clinical studies demonstrating treatment response with hyperpolarised [1-^{13}C]pyruvate.

However, a number of studies have failed to detect treatment response with [1-^{13}C]pyruvate or shown that it is less sensitive than tumour size measurements[173, 178, 179]. In these instances sensitivity may be improved by use of a different substrate. In areas of necrosis a decrease in cell membrane integrity results in an increase in membrane permeability to fumarate and leakage of fumarase into the extracellular space. An increased rate of malate production catalysed by the hydration of fumarate by fumarase has been seen in areas of necrosis following injection of hyperpolarised [1,4 $^{13}C_2$]fumarate[112, 178]. High levels of tumour necrosis have been associated with resistance to some chemotherapeutics and therefore hyperpolarised [1,4

$^{13}C_2$]fumarate may be useful to guide therapy[180]. For monitoring response to treatment it has the significant advantage of being a positive contrast agent.

1.7. HyperPET: combined hyperpolarised ^{13}C MRI and PET

PET-MRI combines improved soft tissue contrast with the functional information provided by both PET and MRI and is likely to be of particular use in instances where MRI is already the anatomical imaging technique of choice, for example in brain, liver and prostate [181]. The high sensitivity of [^{18}F]FDG, which permits whole body imaging, could be combined with targeted tumour imaging using [1-^{13}C]pyruvate for improved metabolic phenotyping. The feasibility of imaging with [^{18}F]FDG and hyperpolarised [1-^{13}C]pyruvate in a single session has been demonstrated in pre-clinical studies, largely in dogs[103, 182-184]. In a single animal the improved specificity of [1-^{13}C]pyruvate for the Warburg effect permitted differentiation of tumour from glycolytic muscle, which was not possible with [^{18}F]FDG[182]. Albeit with small cohorts, comparison of different tumour types (sarcomas and carcinomas) suggests that [^{18}F]FDG uptake and [1-^{13}C]pyruvate metabolism may provide different metabolic information, and the relationship between the two may be specific to tumour type[184].

[^{68}Ga]-labelled prostate specific membrane antigen ([^{68}Ga]PSMA) is an emerging PET technique with improved sensitivity for primary tumours and metastases over anatomical imaging and other PET tracers e.g. [^{18}F]fluoromethylcholine[185, 186]. In three patients with prostate cancer combined imaging using [^{68}Ga]PSMA and hyperpolarised [1-^{13}C]pyruvate provided complementary information. [^{68}Ga]PSMA successfully identified primary and metastatic lesions whilst the rate of pyruvate to lactate exchange correlated with Gleason scoring and response to anti-androgen therapy[165].

1.8. Project aims

The primary aim of this project was to compare [^{18}F]FDG-PET with hyperpolarised [1-^{13}C]pyruvate for the early detection of response to treatment. Measurement of hyperpolarised [1-^{13}C]pyruvate metabolism has several theoretical advantages over [^{18}F]FDG-PET for detecting early tumour response to treatment. First, measurement of [1-^{13}C]pyruvate reduction to lactate has greater tumour specificity than [^{18}F]FDG uptake. [^{18}F]FDG uptake in normal tissue could therefore mask tumour response particularly if there is a treatment-induced inflammatory reaction. Second, by only measuring uptake and phosphorylation [^{18}F]FDG may initially be insensitive to any changes that occur in subsequent steps of glycolysis. Conversely, any decrease in activity of a glycolytic enzyme is likely to rapidly result in reduced lactate concentration detectable using [1-^{13}C]pyruvate. Third, measurement of kinetic reaction rates may be more sensitive to early changes in metabolism than measurement of [^{18}F]FDG accumulation. Hyperpolarised MRI is able to readily estimate kinetic reaction rates whereas calculation of the rate of uptake and inference of glucose consumption rates using [^{18}F]FDG-PET requires prolonged dynamic acquisitions not suitable for routine clinical use. However, evidence on whether hyperpolarised [1-^{13}C]pyruvate can improve on [^{18}F]FDG-PET for detection of response to treatment is currently lacking. To date, there have been two preclinical studies with differing conclusions. Ravoori et al. reported that in SKOV3 ovarian tumours two days of treatment with a tyrosine kinase inhibitor, pazopanib, resulted in significant increases in [1-^{13}C]lactate/([1-^{13}C]pyruvate + [1-^{13}C]lactate) ratio but no change in [^{18}F]FDG % injected dose per gram. At two weeks this difference was no longer observed and at both times differences in tumour volume between control and pazopanib-treated mice were more convincing than any metabolic change[173].

Witney et al. observed similar reductions in k_{pl}, the rate constant for hyperpolarised [1-^{13}C]pyruvate reduction to [1-^{13}C]lactate, and uptake of 2-fluoro-2-deoxy-D-[U-^{14}C]glucose ([^{14}C]FDG) in EL4 tumours 24 h after treatment with etoposide[69]. This project would improve on the work by Witney et al. by:

i. Using *in vivo* [^{18}F]FDG-PET, as per clinical imaging, rather than *ex vivo* scintillation counting of [^{14}C]FDG.
ii. Comparison of hyperpolarised [1-^{13}C]pyruvate and [^{18}F]FDG for the detection of treatment response using the same cohort of animals for both imaging modalities.
iii. Using spectral-spatial pulse sequences capable of imaging hyperpolarised [1-^{13}C]pyruvate and [1-^{13}C]lactate with 3D spatial resolutions up to 1.25 × 1.25 × 2.5 mm and a temporal resolution of 2 s[149]. This permits spatial comparisons of [^{18}F]FDG uptake and [1-^{13}C]lactate production.

In this thesis four different tumour models are used to compare the ability of [^{18}F]FDG-PET and MRI with hyperpolarised [1-^{13}C]pyruvate to detect responses within 24 h of treatment with the following agents:

i. EL4, a murine T-cell lymphoma cell line, treated with 67 mg/kg etoposide.
ii. Eμ-*Myc*, an autochthonous murine model mimicking human Burkitt's lymphoma, treated with 200 mg/kg cyclophosphamide.
iii. Colo205, a metastatic human colorectal adenocarcinoma cell line engineered to express luciferase and mStrawberry reporter genes, treated with 0.4 mg/kg MEDI3039, an experimental TNF-related apoptosis-inducing ligand (TRAIL) agonist.

iv. MDA-MB-231, a triple negative human breast adenocarcinoma cell line engineered to express luciferase and mStrawberry reporter genes, also treated with 0.4mg/kg MEDI3039.

Additionally, a chapter of this thesis is devoted to a study aiming to develop a standardised protocol for [^{18}F]FDG-PET acquisition in mice. By performing 3 – 4 hr dynamic [^{18}F]FDG-PET scans in different tumour models, the aim was to improve on previous work, notably by Fueger et al., to optimise animal handling and timing of static [^{18}F]FDG-PET acquisitions[187]. The models used for this work were:

i. EL4, murine T-cell lymphoma.
ii. Eμ-*Myc,* pre-B cell autochthonous lymphoma.
iii. Colo205, metastatic human colorectal adenocarcinoma.

2. Methods

Methods described here are common to two or more chapters. Methods unique to a chapter are described within that chapter.

2.1. Animal licence statement

Animal experiments were performed in compliance with a project licence issued under the Animals (Scientific Procedures) Act of 1986. Protocols were approved by the Cancer Research UK, Cambridge Institute Animal Welfare and Ethical Review Body.

2.2. EL4 cell culture, tumour growth and treatment

EL4 TIB-39 murine T-cell lymphoma cells (ATCC, Manassas, VA, USA) were cultured in RPMI 1640 medium (Gibco, Waltham, MA, USA) supplemented with 10% foetal bovine serum and 2 mM L-glutamine. Cell number and viability were monitored using Vi-Cell® automated trypan blue staining (Beckman Coulter, Brea, CA, USA). 5×10^6 EL-4 cells suspended in 200 µL phosphate-buffered saline (PBS) were injected subcutaneously into the flanks of female C57BL/6J mice (Charles River, Wilmington, MA, USA). Tumours were imaged when they were ~ 1.5 cm in diameter (typically after 8 – 10 days). Mice were treated with 67 mg/kg etoposide administered intraperitoneally.

2.3. Colo205 cell culture, tumour growth and treatment

Colo205 metastatic colon adenocarcinoma cells (ATCC) were transduced with a lentiviral vector in which mStrawberry red fluorescent protein and luciferase expression were under the control of the EF1 promoter[188]. Cells were cultured in RPMI medium (Gibco) supplemented with 2 mM L-glutamine and 10% heat-inactivated foetal bovine serum (FBS, Gibco). 5×10^6 cells were resuspended in 0.2 mL PBS. The

cell suspensions were implanted subcutaneously into the flanks of female BALB/c nude mice (Charles River). Tumours were imaged when they reached ~0.8 cm^3, typically 6 – 8 weeks after implantation. Mice were treated with 0.4 mg/kg MEDI3039 administered intravenously.

2.4. MDA-MB-231 cell culture, tumour growth and treatment

MDA-MB-231 triple-negative breast adenocarcinoma cells (ATCC) were transduced with a lentiviral vector in which mStrawberry red fluorescent protein and luciferase expression were under the control of the EF1 promoter[188]. Cells were cultured in Dulbecco's Modified Eagle Medium (Gibco) containing 4 mM L-glutamine, 25 mM D-glucose and 10% FBS. 5×10^6 cells were resuspended in a 50:50 mix of Matrigel (Corning, NY, USA) and complete DMEM. The cell suspensions were implanted subcutaneously into the flanks of female BALB/c nude mice (Charles River). Tumours were imaged when they reached ~0.8 cm^3, typically 6 – 8 weeks after implantation. Mice were treated with 0.4 mg/kg MEDI3039 administered intravenously.

2.5. Eμ-*Myc* transgenic mouse breeding, genotyping and treatment

Heterozygous Eμ-*Myc* transgenic mice were bred by the CRUK – CI BRU core facility. The presence of the *c-Myc* transgene and *IgH* enhancer was confirmed by real-time polymerase chain reaction (RT-PCR) for the transgene sequence CCAGCCTCAATCTCA[189]. The forward and reverse primer sequences were CCAGATATTGAAGCAGAACGCAAAA and CAAAACGTCGGCTACAGTAACTTT, respectively (Transnetyx, Cordova, TN, USA). Adult mice were assessed twice weekly for spontaneous development of cervical and axillary tumours[189]. Mice were treated with 200 mg/kg cyclophosphamide.

2.6. Anaesthesia of mice

For all imaging and procedures requiring intravenous cannulation mice were anaesthetised by inhalation of 1 – 2.5% isoflurane (Isoflo, Abbotts Laboratories, Maidenhead, UK) in a 50:50 mix of air (1 L/min) and oxygen (1 L/min). Temperature and respiratory rate were monitored throughout anaesthesia using a rectal thermometer and breathing pad (SAII, Stony Brook, NY, USA).

2.7. Hyperpolarisation of [1-^{13}C]pyruvate

A 44 mg sample of [1-^{13}C]pyruvic acid (Cambridge Isotope Laboratories, Tewkesbury, MA, USA) containing 15 mM of OX063 trityl radical (GE Healthcare, Amersham, UK) and 1.5 mM of gadoterate meglumine (DOTAREM, Guerbet, Roissy, France) was hyperpolarised at ~ 1.2 K by microwave irradiation at 94.110 GHz and 100 mW in a 3.35 T Hypersense polariser (Oxford Instruments, Abingdon, UK) for approximately 1 h. The frozen sample was rapidly dissolved in 6 mL buffer containing 40 mM HEPES, 94 mM NaOH, 30 mM NaCl and 100 mg/L EDTA heated to 180 ºC and pressurised to 10 bar.

2.8. Western blotting

Freeze-clamped tumour samples were homogenised in 10 µL/mg modified RIPA buffer (50 mM HEPES, 1 mM EDTA, 0.7% sodium deoxycholate, 1% Nonidet P-40, 0.5 M lithium chloride, pH 7.6, 1 cOmplete mini EDTA-free protease inhibitor) using a Precellys 24 homogeniser (Precellys, Bertin Instruments, Montigny-le-Bretonneux, France). Proteins were separated by SDS-PAGE and transferred to a nitrocellulose membrane (iBlot 2, Thermofisher Scientific). Membranes were blocked with 1:1 Odyssey blocking buffer and Tris-buffered saline (TBS) and incubated with antibody

solutions at 4 ºC overnight. Antibodies were detected using multiplexed IRDye secondary antibodies and images acquired using an Odyssey CLx (LI-COR Biosciences, NE, USA). Quantification was performed using Image Studio 5.2.5 (LI-COR Biosciences, NE, USA). The antibodies used are listed in Table 2.1.

Antibody Target	Primary Antibody	Manufacturer	Secondary Antibody and dilution
LDH-A	Rabbit polyclonal IgG	Santa-Cruz (sc-33781)	Donkey anti-rabbit 1:15000
MCT1	Rabbit polyclonal IgG	Atlas (HPA003324)	Donkey anti-rabbit 1:15000
MCT4	Rabbit polyclonal IgG	Santa-Cruz (sc50329)	Donkey anti-rabbit 1:15000
HK2	Rabbit mAb	Cell Signalling (C64G5)	Donkey anti-rabbit 1:15000
GLUT1	Goat polyclonal IgG	Santa-Cruz (sc-1603)	Donkey anti-goat 1:5000
GLUT3	Goat polyclonal IgG	Santa-Cruz (sc-7582)	Donkey anti-goat 1:5000
PARP	Rabbit polyclonal IgG	Abcam (ab-6079)	Donkey anti-rabbit 1:15000
β-actin	Mouse mAb	Abcam (ab-6276)	Donkey anti-mouse 1:20000
β-tubulin	Mouse mAb	Cell Signalling (D3U1W)	Donkey anti-mouse 1:20000
GAPDH	Mouse mAb	Abcam (ab9484)	Donkey anti-mouse 1:20000

Table 2.1. Antibodies used for western blotting.

2.9. Lactate dehydrogenase (LDH) activity assay

Extracts in RIPA buffer were prepared from freeze-clamped tumours as above. Samples were diluted so as to achieve a linear reduction in absorbance at 340 nm (A_{340}) over 10 min. 1 µL of sample was added to 167.2 µL Tris-NaCl buffer containing 80 mM Tris, 200 mM NaCl and 0.4 mM NADH. The reaction was started by the addition of 31.8 µL 1.6 mM pyruvate. The change in NADH concentration was monitored by ΔA_{340} using a PHERAstar FS microplate reader (BMG Labtech, Aylesbury, UK). LDH activity was calculated using Beer-Lambert's law:

$$\Delta C = \frac{\Delta A_{340}}{\varepsilon l}$$

where ΔC is the change in concentration of NAD(H) (mol^{-1} L^{-1} min^{-1}), ε is the molar extinction coefficient for NADH at 340 nm (6220 $M^{-1}cm^{-1}$) and l is the path length

(0.6061 cm). One unit of LDH activity was defined as the amount of enzyme that catalyses the oxidation of 1 μmol NADH min^{-1} at pH 7.2 and 23 ºC (room temperature).

2.10. Immunohistochemistry (IHC)

Tumours were excised immediately post-mortem, immersed in neutral buffered formalin and after 24 h transferred to 70% ethanol. Immunohistochemistry was performed by Jodi Miller and the Histopathology Core Facility, CRUK Cambridge Institute. Tumour sections, 6 μm thick, were de-waxed and rehydrated using a Leica ST5020 Multistainer (Leica, Wetzler, Germany) and stained for cleaved caspase-3 (CC3) and terminal deoxynucleotidyl transferase nick-end labelling (TUNEL). CC3 staining was performed using a Bond Polymer Refine Detection Kit (DS9800, Leica, Wetzlar, Germany) and a 1:200 dilution of CC3 rabbit monoclonal antibody (9664, Cell Signalling Technology, Danvers, MA, USA). TUNEL staining was performed using a combination of a Bond Polymer Refine Detection Kit (DS9800, Leica, Wetzlar, Germany) and a DeadEnd Colorimetric TUNEL System (G7130, Promega, Madison, WI, USA). Analysis was performed using Aperio ImageScope 12.3.3 (Leica, Wetzlar, Germany). TUNEL % positivity was calculated using an automated positive pixel count and subtracting the % positivity of the negative control slide from the positive stained slide. CC3 % positivity was calculated using an automated positive pixel count.

2.11. Statistical analysis

Graphical and statistical analyses were performed using Prism v 6.0 (GraphPad Software, La Jolla, CA, USA). Statistical tests performed were paired or unpaired two-tailed *t*-tests with errors representing standard deviation, unless stated otherwise. *P*

values are summarised in figures as: <0.0001, ****; 0.0001 – 0.001, ***; 0.001 – 0.01, **, 0.01 to 0.05 *.

3. Optimisation of [^{18}F]FDG-PET imaging in mice

3.1. Introduction

PET imaging with [^{18}F]FDG is used in pre-clinical studies as a surrogate for glucose uptake in normal tissues and tumours. Widespread clinical use of [^{18}F]FDG-PET, particularly in oncology, has resulted in its use as a gold standard for determining the performance of many new imaging agents[182, 190]. [^{18}F]FDG-PET is affected by numerous factors that can be attributed to variations in animal biology, scanner and hardware performance, acquisition and reconstruction settings and methods of image analysis. Failure to adequately control the external variables results in poor reproducibility, a lack of comparability between studies and potentially erroneous conclusions. This chapter will focus on the importance of controlling biological factors and the timing of static PET acquisitions.

In clinical practice guidelines such as those produced by the European Association of Nuclear Medicine (EANM) and the Quantitative FDG-PET Biomarker Committee outline how many factors should be controlled during PET imaging[191, 192]. Prior to clinical [^{18}F]FDG studies, patients are kept in a warm, non-stimulating environment and asked to avoid physical activity to minimise background uptake by normal muscle and brain tissue. Patients also undergo a period of fasting prior to imaging. The aim of this is two-fold: i) to reduce competition from high levels of circulating glucose and ii) to maintain steady levels of insulin, variation of which may change the distribution of [^{18}F]FDG uptake. The presence of fasting hyperglycaemia (>7 mmol/L) can delay imaging as it is considered to alter [^{18}F]FDG distribution and reduce the quality of [^{18}F]FDG-PET images although the evidence is not conclusive[193-196]. The uptake and slow accumulation of [^{18}F]FDG in tissues is a dynamic process, but most clinical PET studies are static acquisitions. The timing of the acquisition is therefore of vital importance and the majority of scans are acquired at 60 min after

intravenous injection of [^{18}F]FDG, with a tolerance of 55 – 75 min[191, 192]. This time point is a compromise between best contrast and speed as almost all imaging studies suggest that the tumour-to-blood ratio (TBR) continues to increase with acquisition time[197-203].

Although clinical guidelines do not necessarily optimise [^{18}F]FDG-PET, they permit repeat studies acquired on the same scanner (or on cross-calibrated scanners) to be adequately compared for answering most clinical questions, which are often simple and do not require absolute quantification[204].

In pre-clinical imaging no such guidelines exist and, particularly when being used for benchmarking of novel imaging tests, there is a requirement to optimise [^{18}F]FDG-PET to avoid potential bias. The work of Fueger et al. is commonly cited and has led to the partial standardisation of animal handling[187]. However, Fueger et al. mainly investigated the effects of altered animal handling on [^{18}F]FDG biodistribution in normal, non-anaesthetised mice and their investigation of tumours was limited to two conditions (fasted and warmed vs. not fasted and not warmed)[187]. Similarly to clinical studies, the timing of static preclinical [^{18}F]FDG-PET acquisitions is typically 60 min post-injection. The rationale for this time point in rodent studies appears to be convenience rather than optimisation, as most studies indicate that TBR continues to increase with time[187, 205-207]. [^{18}F]FDG kinetics may also be different in subcutaneous xenograft, orthotopic xenograft and autochthonous tumours[205].

Focussing on tumour imaging, the first aim of this study was to investigate the separate effects of pre-warming and fasting on [^{18}F]FDG biodistribution in mice. Dynamic 4 h [^{18}F]FDG-PET scans of EL4 murine T-cell lymphoma tumour-bearing mice demonstrated that fasting increased tumour uptake and decreased myocardial uptake of [^{18}F]FDG, whilst there was no significant effect of pre-warming.

To define an optimal time point for static PET acquisition, dynamic scans of mice bearing subcutaneous EL4 T-cell lymphomas and Colo205 human colon adenocarcinomas demonstrated that subcutaneous tumour SUV_{mean} and TBR continued to increase up to 170 min post-injection with more pronounced increases in uptake over time in fasted mice. In Eμ-*Myc* autochthonous lymphomas there was no significant increase in uptake after 30 min post-injection. These results suggest that static PET scans 60 min after injection significantly underestimate maximal SUV in subcutaneous tumours and later timepoints would increase tumour contrast.

3.2. Methods

The following methods described in "Chapter 2 - Methods" are used in this chapter:

2.1. Animal licence statement

2.2. EL4 cell culture, tumour growth and treatment

2.3. Colo205 cell culture, tumour growth and treatment

2.5. Eμ-*Myc* transgenic mouse breeding, genotyping and treatment

2.6. Anaesthesia of mice

2.11. Statistical analysis

3.2.1. Animal preparation

The effects of animal handling on [^{18}F]FDG-PET of EL4 tumour-bearing mice was studied by varying conditions according to Table 3.1. For fasting, mice were transferred to a new cage without food for 6 – 10 h. Mice in the fed group were transferred to a new cage 6 – 10 h prior to imaging with food freely available. All mice had water freely available at all times. For pre-warming mice were placed in a chamber heated to 31 ºC, the thermoneutral temperature of mice, for approximately 60 min prior

to anaesthesia[208]. Mice not warmed remained at 18 – 21 ºC, the ambient temperature of the animal house, up to induction of anaesthesia. Henceforth pre-warmed mice are referred to as “warmed” mice and mice not pre-warmed are referred to as “cold” mice.

Number of mice	Conditions
3	Fasting, pre-warmed 31 ºC
5	Fasting, no warming
5	Fed, pre-warmed 31 ºC
3	Fed, no warming

Table 3.1. Animal handling conditions for EL4 tumour-bearing mice.

Mice were anaesthetised with isoflurane as described in Methods 2.6. After induction of anaesthesia all mice were kept on a heating pad for intravenous tail vein cannulation prior to being transferred to the heated bed on a nanoScan PET/CT (Mediso, Budapest, Hungary). Throughout imaging, the temperature and respiratory rate of mice were measured using a rectal temperature probe and breathing pad, respectively (SAII, Stony Brook, NY, USA). Heating was adjusted to maintain rectal temperature between 36 and 37.5 ºC whilst anaesthesia was titrated to maintain a respiratory rate of 80 – 120 breaths per min. Venous glucose concentration was measured using a StatStrip Xpress glucose meter (Nova Biomedical, Waltham, MA, USA) prior to imaging.

Colo205 mice (n = 8) were imaged following a period of fasting and pre-warming as described above. Eμ-*Myc* mice (n = 4) were pre-warmed but were not fasted as the mice did not tolerate fasting.

3.2.2. [^{18}F]FDG-PET imaging

3 h (Colo205 and Eμ-*Myc*) and 4 h (EL4) PET acquisitions were started just prior to intravenous injection over 30 s of [^{18}F]FDG into each tumour-bearing mouse. Data were acquired in list-mode format. A CT image was acquired for anatomic co-registration and attenuation correction. Scans were reconstructed with an isotropic voxel size of 0.6 mm using a three-dimensional ordered-subset expectation maximization method, two iterations and six subsets. Images were normalised and corrected for decay, dead-time, random events and attenuation. 3 h scans were reconstructed into 91 time frames (5 s × 24, 0 – 2 min; 15 s × 12, 2 – 5 min; 30 s × 10, 5 – 10 min; 1 min × 10, 10 – 20 min; 2 min × 20; 20 – 60 min; 5 min × 6, 60 – 90 min and 10 min × 9, 90 – 180 min). 4 h scans were reconstructed into 97 time frames of the above durations with an additional six × 10 min segments from 180 – 240 min.

3.2.3. Image analysis

The images were analysed using Vivoquant 3.0 software (InviCRO, Massachusetts, USA). An image-derived arterial input function (AIF) was acquired from a 3D ROI drawn manually over the inferior vena cava. To minimize spill-in effects the ROI was drawn between the level of the kidneys and diaphragm, where contributions from other organs are relatively low, and thresholded at 75% of the maximum in the 5 s time frames. A 3D ROI drawn manually over the tumour was Otsu thresholded on the last time frame to delineate the tumour. A 3D ROI drawn manually over the heart was thresholded above 75% of the maximum to try to define the myocardium while minimising spill-in effects. SUV was calculated as:

$$SUV = \frac{c_{img}}{ID/BW}$$

where c_{img} is the activity concentration (MBq/mL) derived from the image ROI, ID is the injected dose (MBq) and BW is the body weight (g) of the animal.

Patlak graphical analysis was used to estimate the net rate of [^{18}F]FDG uptake (K_i) from the linear portion of the graph between 20 and 60 min[209]. Patlak multiple-time graphical analysis assumes irreversible uptake of a tracer into a tissue compartment. The rate of accumulation of tracer in a tissue ROI (R) at a time (t) after tracer injection can be expressed as:

$$R(t) = K_i \int_0^t C_p(\tau)d\tau + V_0 C_p(t)$$

where C_p is the plasma activity, V_0 is the blood and interstitial volume (the reversible compartment) of the ROI and C_p is the plasma input function. This can be rearranged as:

$$\frac{R(t)}{C_p(t)} = K_i \frac{\int_0^t C_p(\tau)d\tau}{C_p(t)} + V_0$$

When plotted graphically, the slope becomes linear after the free [^{18}F]FDG in the reversible compartments has equilibrated with the [^{18}F]FDG in plasma and has a gradient equal to K_i.

3.3. Results

Twenty-eight mice were injected with 12.75 ± 4.2 MBq [^{18}F]FDG and completed dynamic 3 – 4 h PET imaging. Sixteen mice had subcutaneous EL4 tumours, eight had subcutaneous Colo205 tumours and four were Eμ-*Myc* mice.

3.3.1. Fasting reduces blood glucose in EL4 tumour-bearing mice

Blood glucose was measured in tail vein samples prior to intravenous cannulation. Blood glucose was 8.3 ± 1.8 mmol/L (n = 8) in animals allowed access to

food up until anaesthesia and 5.2 ± 1.4 mmol/L (P = 0.0029, n = 8) in fasted animals (Figure 3.1). Pre-warming animals did not have a significant effect on venous glucose concentration.

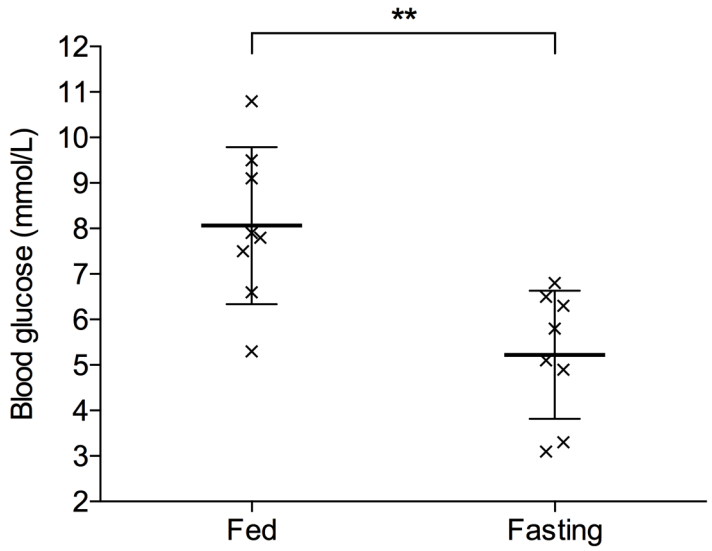

Figure 3.1. Blood glucose measurements in fed vs. fasted mice.

3.3.2. [^{18}F]FDG biodistribution in EL4 tumour-bearing mice

EL4 tumour-bearing mice were injected with [^{18}F]FDG intravenously and underwent 4 h dynamic PET scans. The exact timing of injection varied slightly and the peak activity seen in the inferior vena cava ROI occurred between 10 and 30 s after the start of the scan. The tissues irreversibly accumulating the most [^{18}F]FDG were the myocardium, tumours and, to a lesser extent, Harderian glands (Figures 3.2 – 3.6). Initially, perfusion of the liver resulted in a liver SUV_{mean} peak of 2.57 ± 0.5 at the 40 s time frame but this decreased from to 0.12 ± 0.1 by the 230 – 240 min time frame, indicating very little irreversible uptake. Similarly, there was rapid renal perfusion and excretion of [^{18}F]FDG but SUV_{mean} decreased from 6.64 ± 0.6 after 1 – 1.5 min to a minimum SUV_{mean} in the final time frame of 0.46 ± 0.1, again indicating minimal tracer uptake. The SUV_{mean} of the brain cortex peaked at 2.53 ± 0.2 between

12 and 24 min and then decreased over the duration of the scan, reaching a minimum of 0.85 ± 0.06 in the last time frame. This decrease may be partially due to a large vascular component in the brain ROI but the slower rate of decrease compared to the liver and blood pools suggests that this decrease is due to slow de-phosphorylation of [^{18}F]FDG-6*P* and partially reversible trapping.

3.3.3. Effect of animal handling on myocardial and tumour [^{18}F]FDG uptake

The SUV_{mean} values in the 230 – 240 min time frame were used to compare final uptake between EL4 tumour-bearing mice under different conditions. Pre-warming had no significant effect on tumour or myocardial [^{18}F]FDG uptake. However, fasting resulted in suppression of myocardial uptake and an increase in tumour uptake (Figure 3.3 – 3.8). In cold and fed animals myocardial SUV_{mean} was 13.5 ± 2.9 (n = 3) but in cold and fasted animals was 4.90 ± 1.67 (n = 5, P = 0.0015). The pattern was similar in warmed mice where myocardial SUV_{mean} was 9.88 ± 3.6 (n = 5) in fed mice and reduced to 5.28 ± 0.3 (n = 3) in fasted mice, although due to one outlier in the fed group this was not quite significant (P = 0.075) (Figure 3.7 and 3.8). Tumour SUV_{mean} was 4.09 ± 0.39 (n = 3) in cold and fed mice and 5.13 ± 0.4 (n = 5; P = 0.01) in fasted mice. Similarly in pre-warmed mice tumour SUV_{mean} was 3.47 ± 0.7 (n = 5) in fed mice and 4.71 ± 0.4 (n = 3, P = 0.034) in fasted mice.

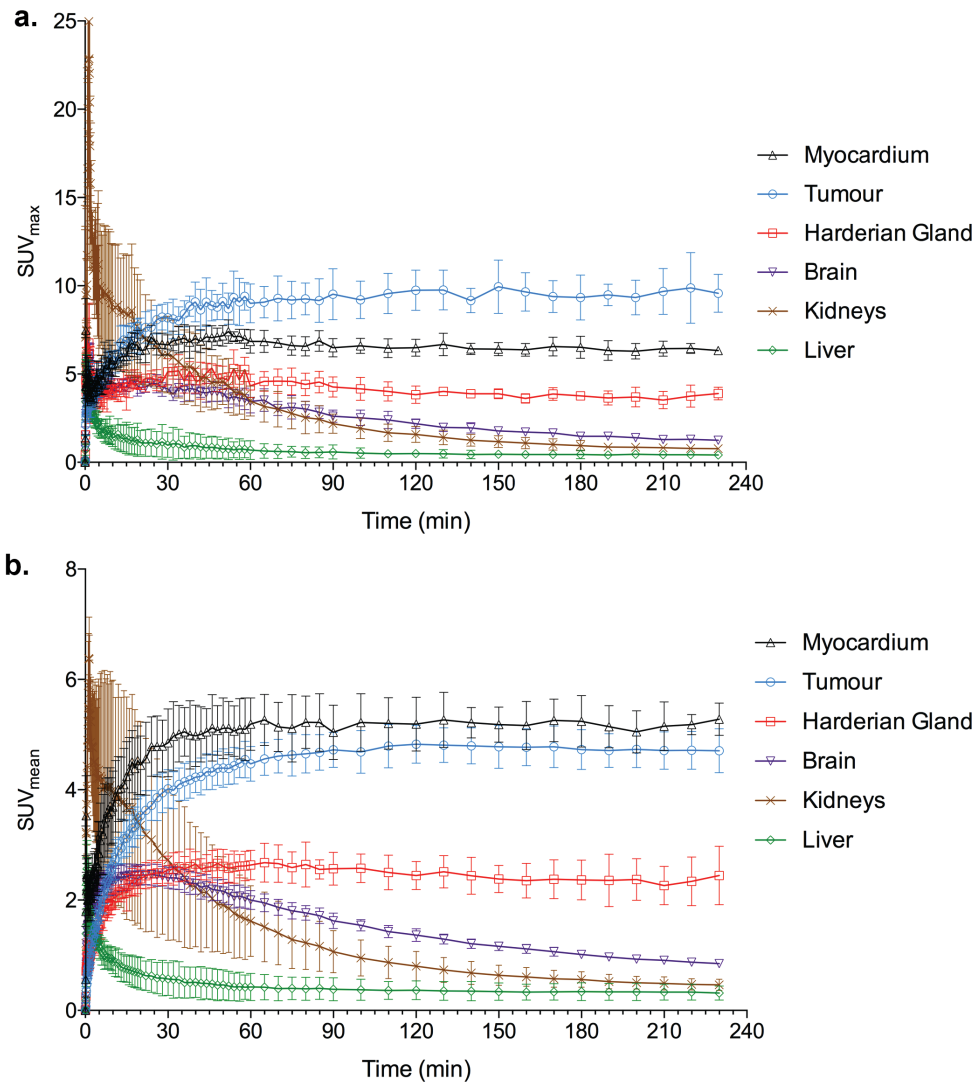

Figure 3.2. Time courses of dynamic [^{18}F]FDG-PET scans in warmed and fasted EL4 tumour-bearing mice (n = 3). (a) SUV_{max} and **(b)** SUV_{mean}.

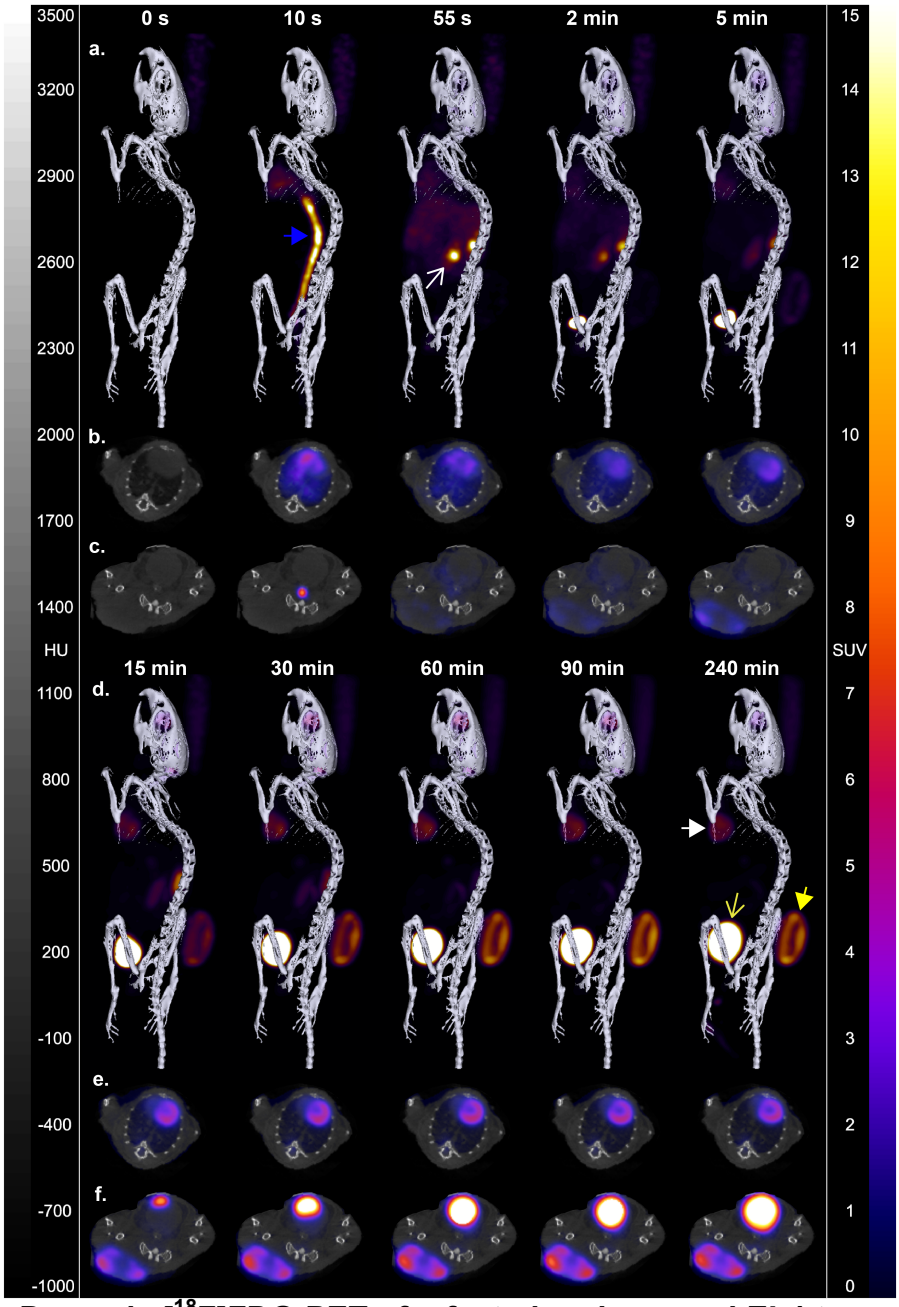

Figure 3.3. Dynamic [^{18}F]FDG-PET of a fasted and warmed EL4 tumour-bearing mouse demonstrating low myocardial uptake and high tumour uptake. (Rows a & d) 3D reconstructions of bone CT and [^{18}F]FDG-PET. Solid blue arrow – inferior vena cava (10 s); outline white arrow – right kidney (55 s); solid white arrow – heart (240 min); solid yellow arrow – tumour (240 min); outline yellow arrow – bladder (240 min). Axial [^{18}F]FDG-PET/CT slice through **(rows b & e)** heart and **(rows c & f)** tumour. The PET voxels covering the bladder are saturated in the later time frames to allow the other organs to be visualised.

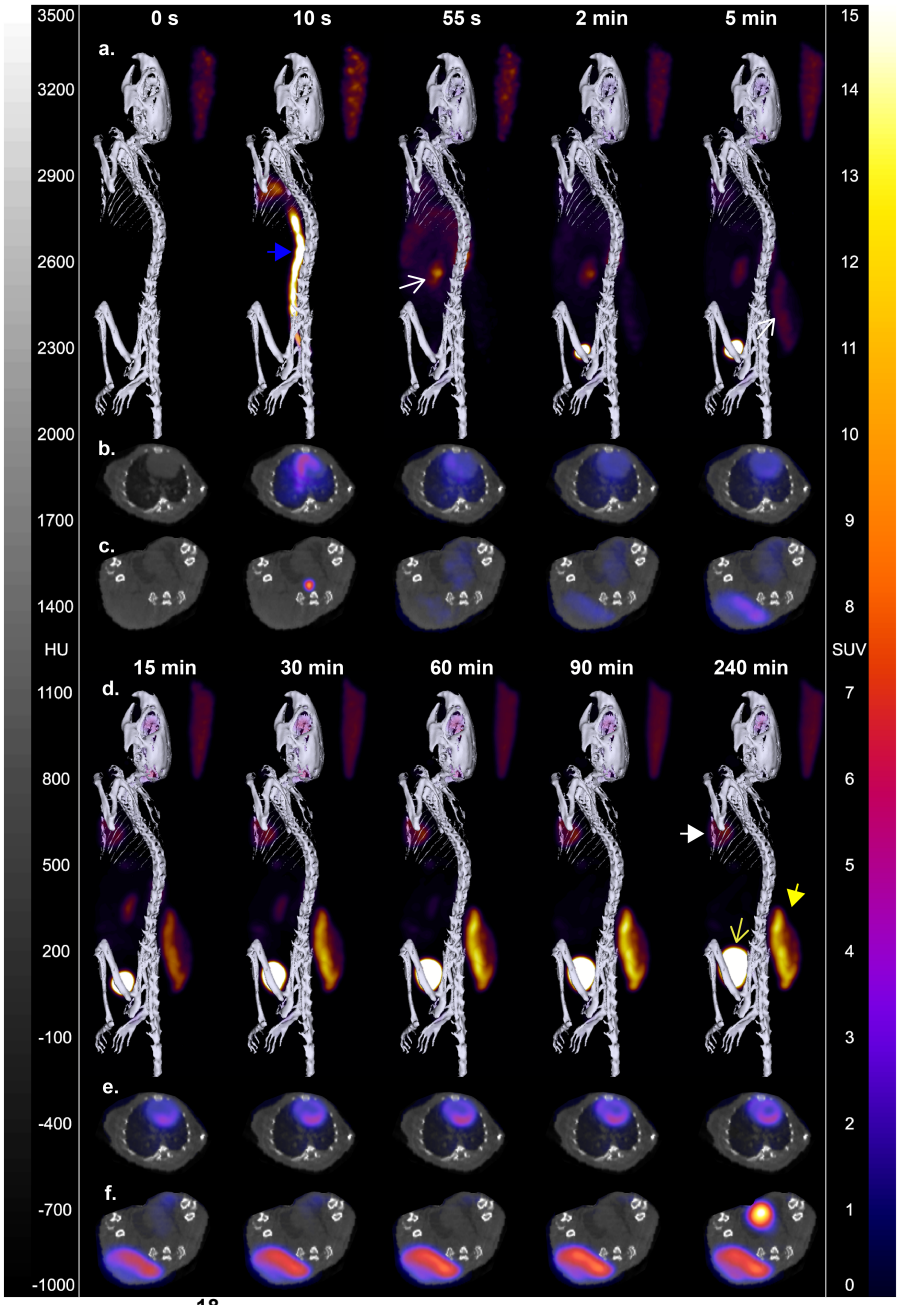

Figure 3.4. Dynamic [^{18}F]FDG-PET scans of a fasted and not warmed EL4 tumour-bearing mouse demonstrating low myocardial uptake and high tumour uptake. (Rows a & d) 3D reconstructions of bone CT and [^{18}F]FDG-PET. Solid blue arrow – inferior vena cava (10 s); outline white arrow – right kidney (55 s); solid white arrow – heart (240 min); solid yellow arrow – tumour (240 min); outline yellow arrow – bladder (240 min). Axial [^{18}F]FDG-PET/CT slice through **(rows b & e)** heart and **(rows c & f)** tumour. The PET voxels covering the bladder are saturated in the later time frames to allow the other organs to be visualised.

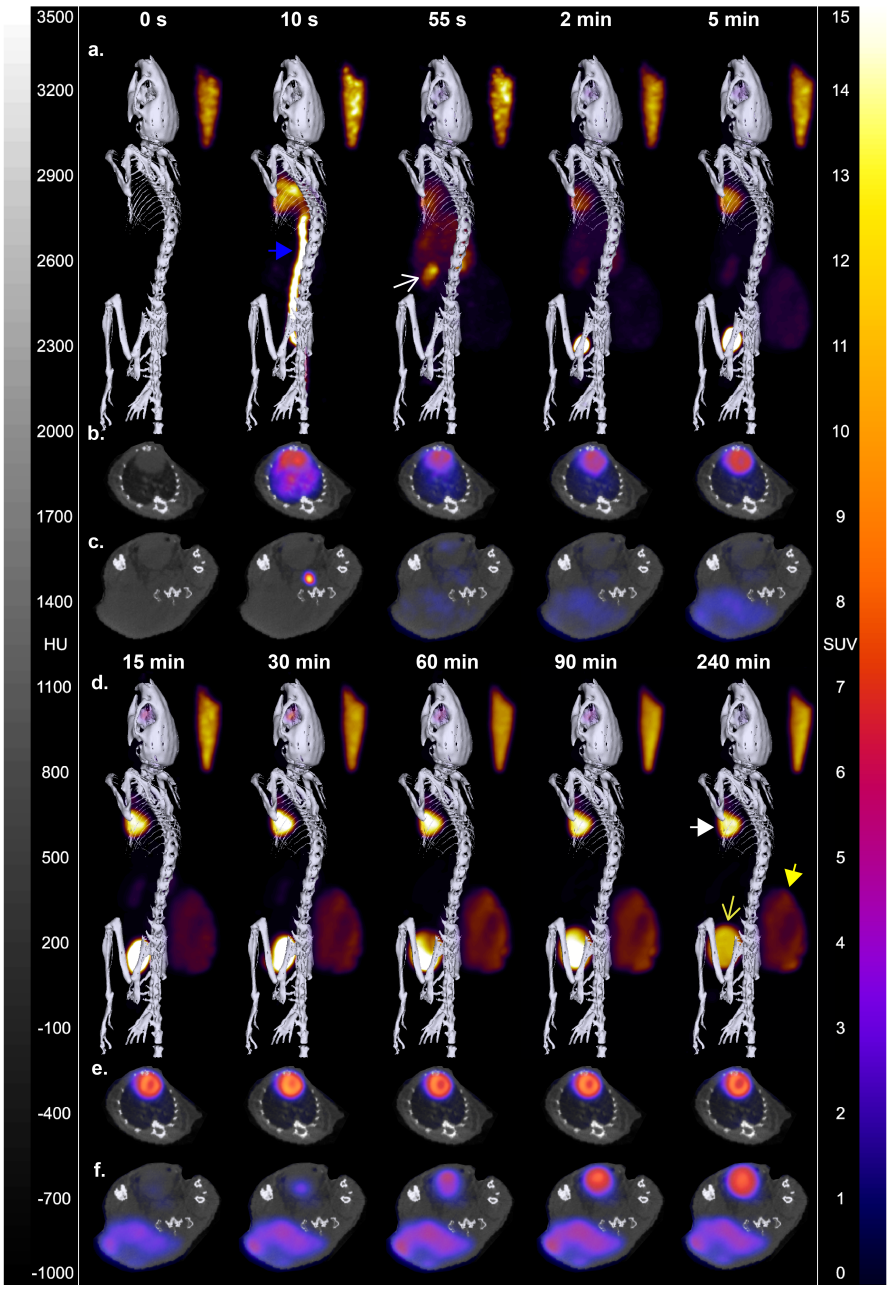

Figure 3.5. Dynamic [^{18}F]FDG-PET of a fed and warmed EL4 tumour-bearing mouse demonstrating high myocardial uptake and low tumour uptake. (Rows a & d) 3D reconstructions of bone CT and [^{18}F]FDG-PET. Solid blue arrow – inferior vena cava (10 s); outline white arrow – right kidney (55 s); solid white arrow – heart (240 min); solid yellow arrow – tumour (240 min); outline yellow arrow – bladder (240 min). Axial [^{18}F]FDG-PET/CT slice through **(rows b & e)** heart and **(rows c & f)** tumour. The PET voxels covering the bladder are saturated in the later time frames to allow the other organs to be visualised.

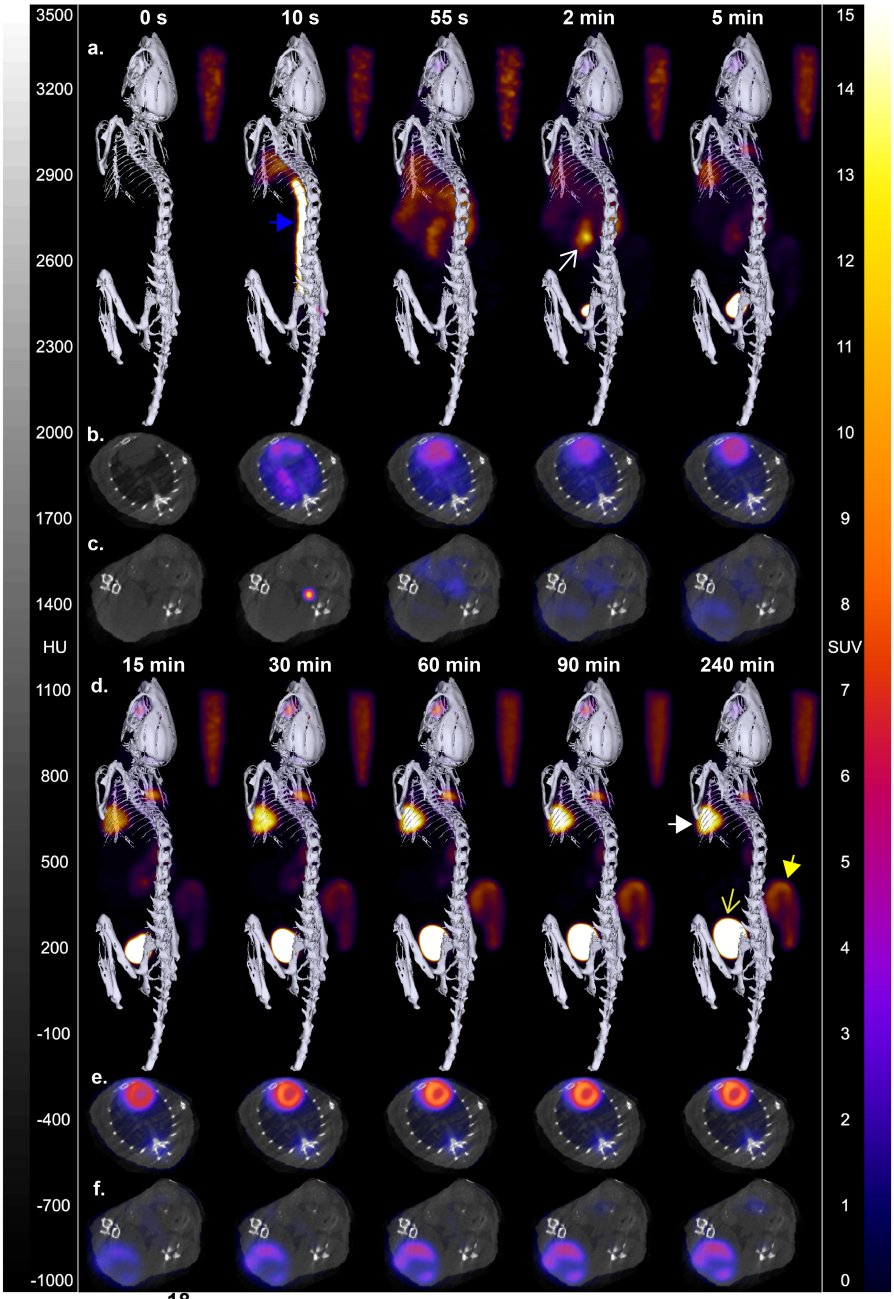

Figure 3.6. Dynamic [^{18}F]FDG-PET of a fed and not warmed EL4 tumour-bearing mouse demonstrating high myocardial uptake and low tumour uptake. (Rows a & d) 3D reconstructions of bone CT and [^{18}F]FDG-PET. Solid blue arrow – inferior vena cava (10 s); outline white arrow – right kidney (2 min); solid white arrow – heart (240 min); solid yellow arrow – tumour (240 min); outline yellow arrow – bladder (240 min). Axial [^{18}F]FDG-PET/CT slice through **(rows b & e)** heart and **(rows c & f)** tumour. The PET voxels covering the bladder are saturated in the later time frames to allow the other organs to be visualised.

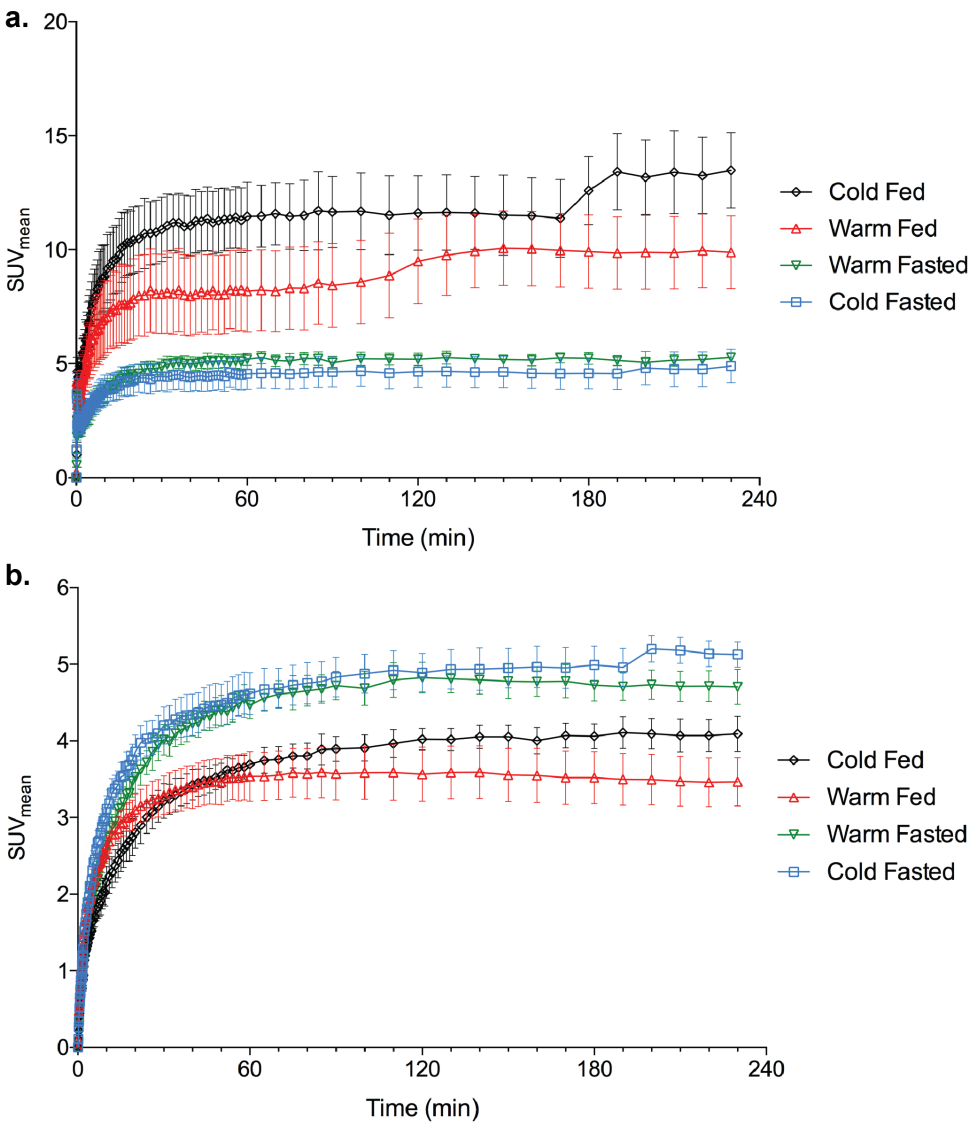

Figure 3.7. Mean dynamic SUV_{mean} for animals under different handling conditions in the (a) myocardium and (b) EL4 tumours. The occasional steps in the time-activity curves (TACs) that can be seen, for example in the myocardium for cold and fed mice at 180 min, are movement artefacts. Error bars are SEM.

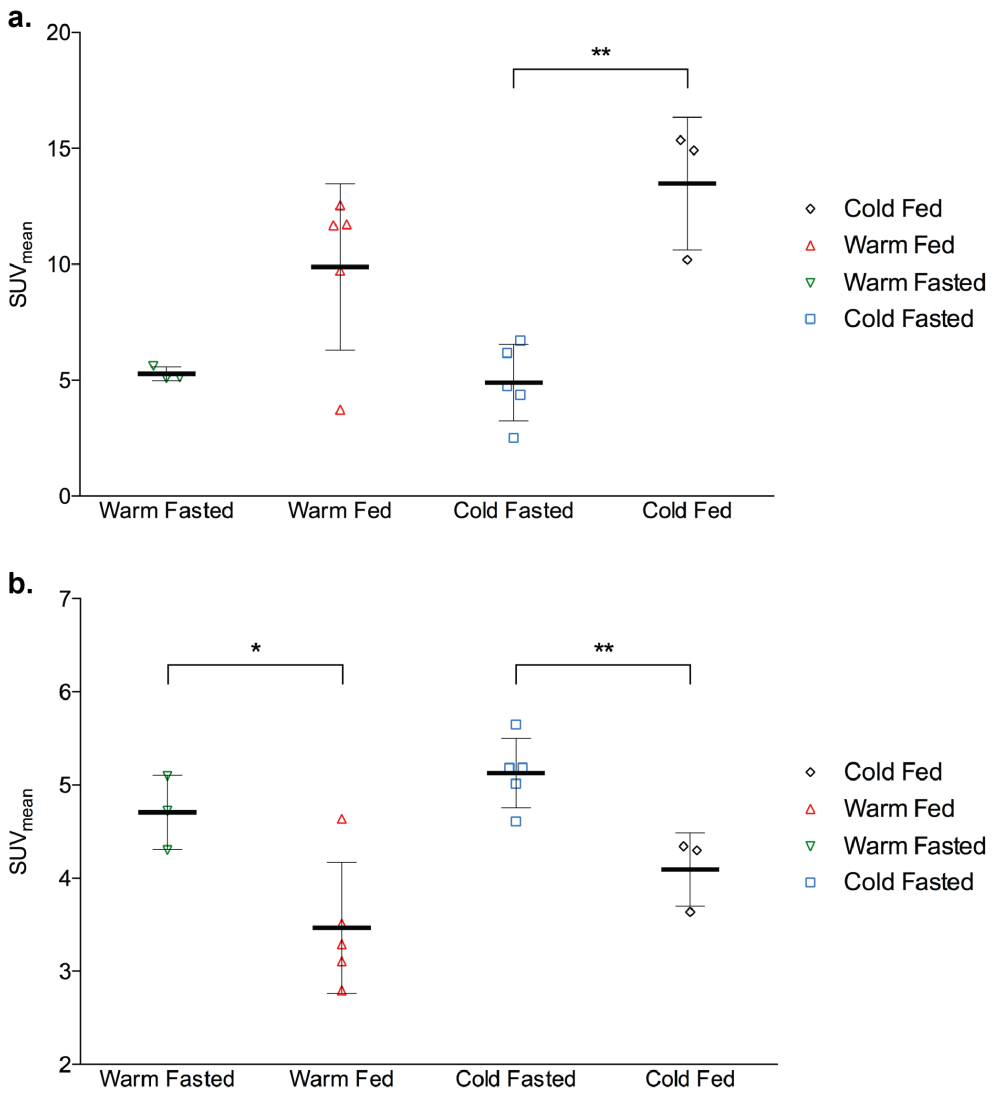

Figure 3.8. SUV_{mean} in the last time frame (230 – 240 min) for all animals (a) myocardium and (b) EL4 tumours under different animal handling conditions.

3.3.4. Comparison of [^{18}F]FDG uptake in different tumour models and animal handling conditions

To find an optimal time point for static [^{18}F]FDG-PET in mouse tumours, uptake was compared between EL4, Colo205 and Eμ-*Myc* models (Figure 3.9). Colo205 tumour-bearing mice were warmed and fasted prior to imaging, as this was presumed to be the optimum conditioning, but Eμ-*Myc* mice were fed throughout due to the high

morbidity of the model. Eμ-*Myc* cervical tumours were used for comparison although uptake in cervical, axillary and inguinal tumours was almost identical (Figure 3.10). In cold and fasted mice significant increases in EL4 tumour SUV_{mean} were observed up to 170 min post-injection (Figure 3.11 c). In warm and fasted mice and cold and fed mice, EL4 tumour SUV_{mean} increased significantly from 60 – 90 min (Figure 3.11 a & d). Although there were further small increases under these conditions up to 170 min, these were not significant. In warm and fed EL4 mice and Colo205 mice there was only a significant increase in tumour SUV_{mean} from 30 – 60 min post-injection (Figure 3.12 b & e). In Eμ-*Myc* tumours there were no significant changes in SUV_{mean} between 30 – 170 minutes and the small decrease in SUV_{mean} seen after 60 min was also primarily due to a movement artefact.

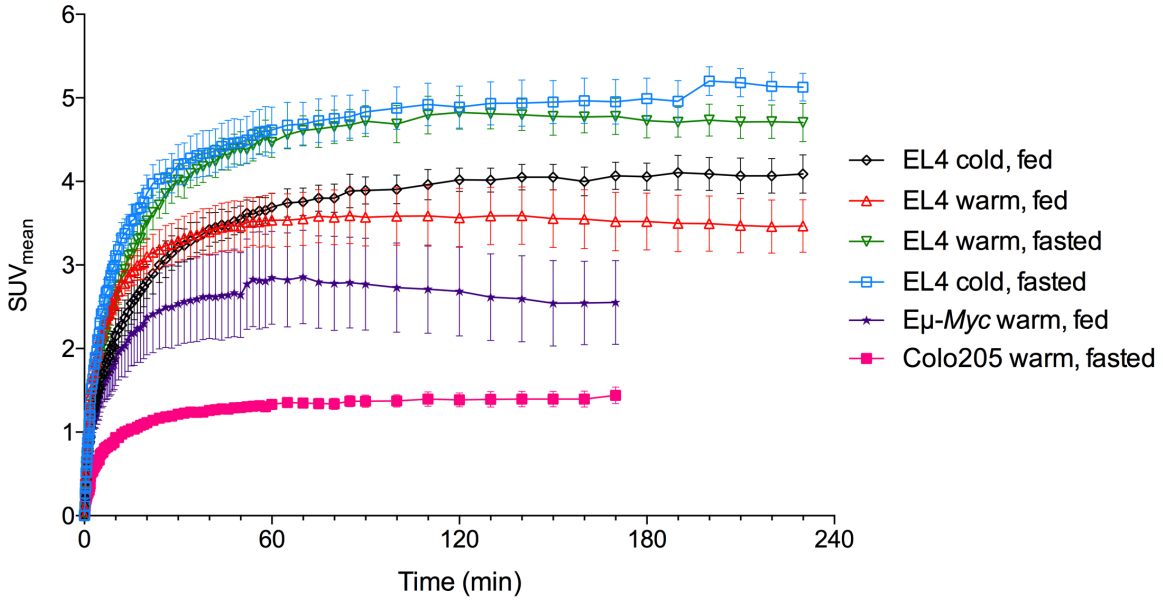

Figure 3.9. Tumour SUV_{mean} over time for the different tumour models and EL4 tumours imaged under different animal handling conditions. Error bars are SEM.

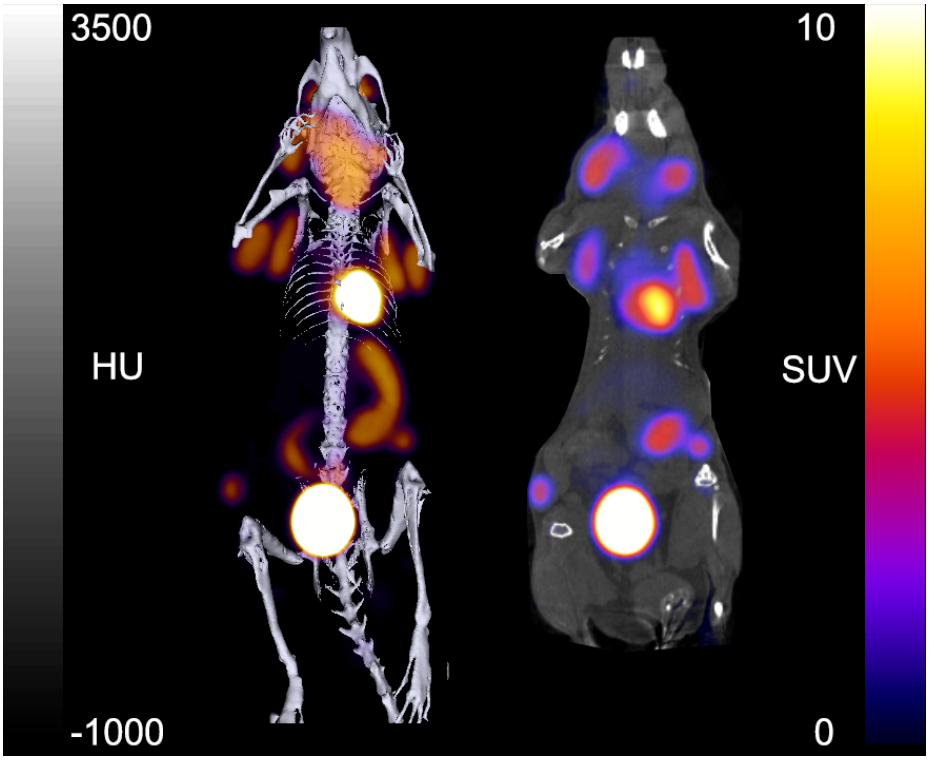

Figure 3.10. Uptake in an Eμ-*Myc* at 90 min post-injection of [^{18}F]FDG. Cervical, axillary and inguinal tumours are visible on both the maximum intensity projection (MIP) (left) and coronal slice (right). High uptake in the spleen is also visible in the MIP.

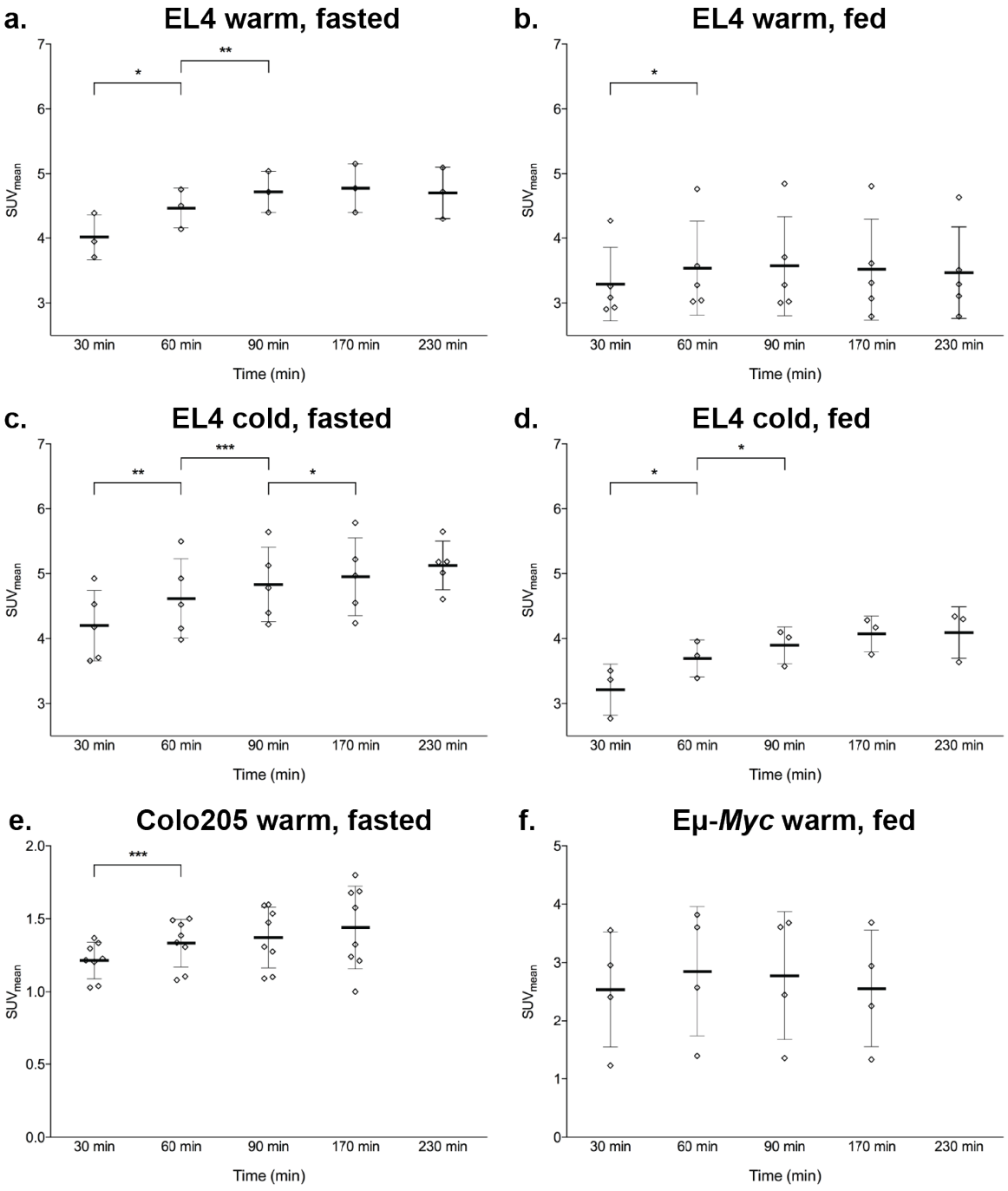

Figure 3.11. Tumour SUV_{mean} at 30, 60, 90, 170 and 230 min for the different models and different animal handling conditions.

3.3.5. Tumour-to-blood SUV_{mean} ratios in the different tumour models

Tumour-to-blood ratios have been shown to correlate more closely with [^{18}F]FDG K_i than to SUV[210]. Furthermore, tumour-to-blood ratios provide an indication of tumour-to-background contrast, irrespective of any background tissue uptake. The input function derived from the vena cava was highly reproducible and after the initial peak, decreased up to approximately 100 min post-injection (Figure 2.12). Thus, tumour-to-blood ratio and tumour SUV_{mean} followed similar trends.

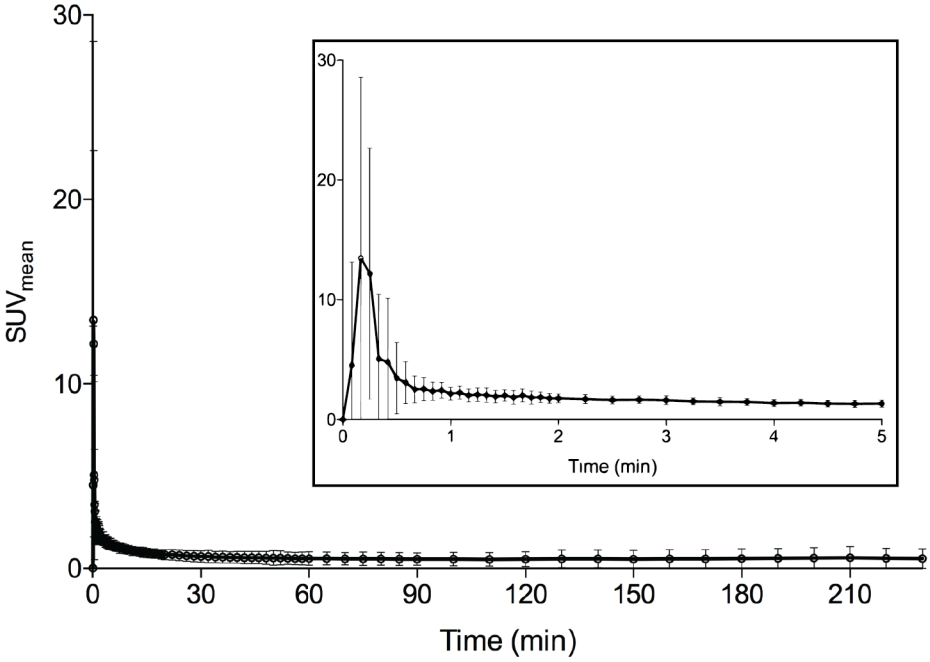

Figure 3.12. Image derived input function from the inferior vena cava (n = 28). The inset shows the SUV_{mean} between 0 and 5 min.

Tumour-to-blood [^{18}F]FDG ratios increased up to 170 min post-injection in all fasted mice, although in EL4 warm, fasted mice the low numbers meant that the increase was statistically significant only between 90 and 170 min (Figure 2.13 and 2.14). The increases were less apparent in fed mice. In autochthonous Eμ-*Myc*

tumours the insignificant decrease in tumour-to-blood ratio after 60 minutes was primarily due to movement artefact in one animal.

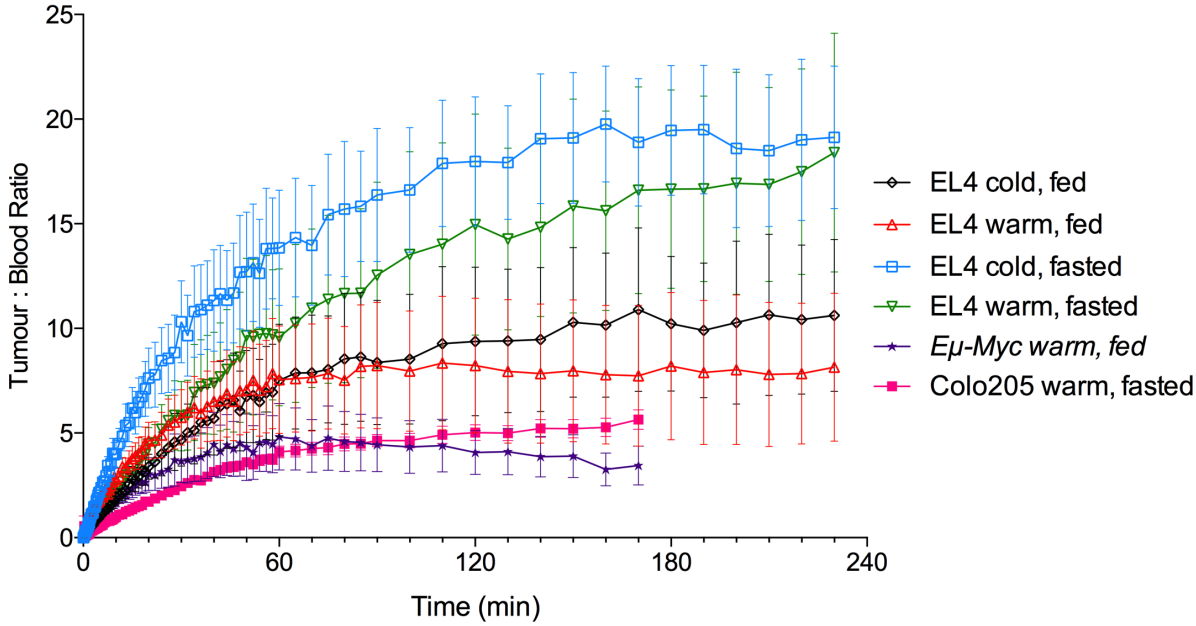

Figure 3.13. Tumour-to-blood SUV_{mean} ratios in different tumour models under different animal handling conditions. Error bars are SEM.

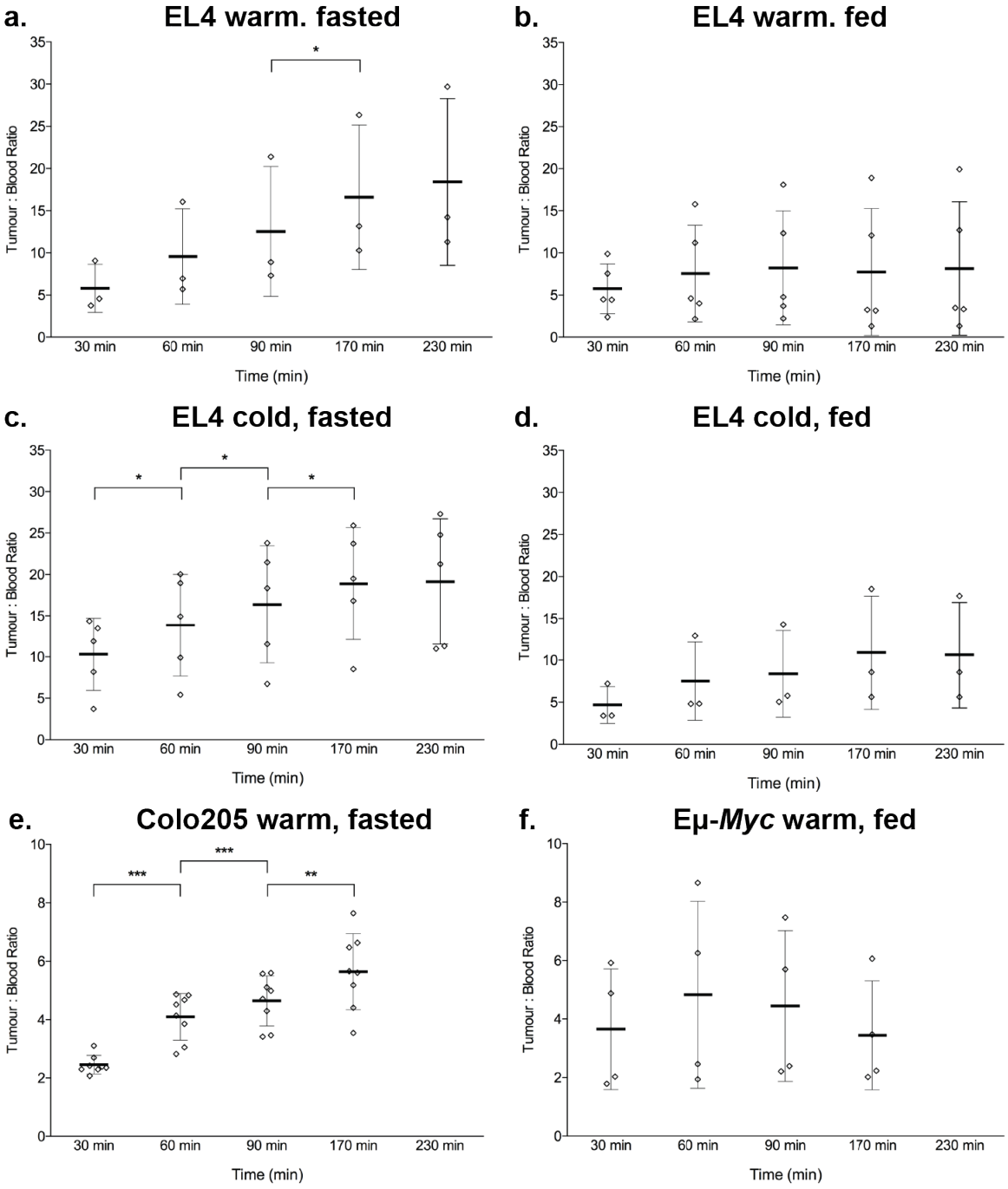

Figure 3.14. Tumour-blood ratios at 30, 60, 90, 170 and 230 min for the different models and different animal handling conditions. These are the same data as used in Figure 2.13.

3.4. Discussion

Patient studies have shown that delaying [^{18}F]FDG-PET acquisition beyond the standard 60 min post-injection may be beneficial. In glioma patients scans performed up to 8 h post-injection yielded improved contrast between normal brain and tumour due to the higher glucose-6-phosphatase activity in normal brain[199]. In non-small cell lung cancer patients dynamic studies and simulation estimated a time to plateau for the tumour SUV of between 130 – 500 min[198]. Similar results in lymphoma, breast and bone cancers suggest that improved tumour-to-background ratio and differentiation of malignancy from benign lesions can be achieved by imaging ≥ 2 h post-injection[200-203].

In rodents the effect of PET acquisition timing has only been studied over shorter periods, typically ≤60 min[187, 205]. Rat mesotheliomas could be differentiated from inflammatory lesions at 90 min, but not 45 min, post-injection[207]. Our study demonstrates that in autochthonous Eμ-*Myc* tumours [^{18}F]FDG uptake peaked around 60 min but in subcutaneous tumours, under most animal handling conditions, it continued to accumulate beyond 60 min and up to 170 min post-injection. The slower uptake in subcutaneous tumours may indicate their relatively poorer perfusion compared to autochthonous tumours. In all tumours, [^{18}F]FDG uptake was irreversible up to 4 h. Other than tumours, only the myocardium and Harderian glands exhibited significant irreversible [^{18}F]FDG uptake. Brain, liver and kidney SUV_{mean} decreased with time. In normal brain this suggests significant glucose-6-phosphatase activity[211]. Liver TACs closely followed those of the inferior vena cava, meaning [^{18}F]FDG retention in the liver was minimal, corroborating previous studies[212, 213]. Although there was rapid urinary clearance of [^{18}F]FDG in all mice, there was very little retention [^{18}F]FDG in the kidneys. The decreasing activity of normal brain, liver and kidney with time has significant implications for tumour imaging, particularly for orthotopic and

autochthonous tumours in those organs as an improved tumour-to-background ratio could be expected at later time points.

This study investigated [^{18}F]FDG biodistribution when mice were fasted and warmed to thermoneutral temperature for 1 h prior to anaesthesia, aiming to refine previous studies[187, 214-216]. The anaesthetic regimen was the same for all mice and all were warmed immediately following anaesthesia to avoid sub-physiological temperatures. Fasting resulted in a 25 – 35% increase in [^{18}F]FDG uptake in EL4 tumours. The increase in tumour uptake in fasted animals has previously been attributed to decreased competition with plasma glucose, although in a rodent study supraphysiological hyperglycaemia (>50 mmol/L) was required to demonstrate this[214]. In contrast, fasting decreased myocardial uptake by 47 – 64%, presumably reflecting the heart's ability to utilise other metabolic substrates, such as fatty acids and lactate, when blood glucose is suppressed[217]. Further depression of myocardial [^{18}F]FDG uptake may be possible by using sevoflurane anaesthesia[216]. Pre-warming mice for 1 h prior to anaesthesia had no significant effect on myocardial or tumour [^{18}F]FDG uptake. Therefore one might expect any added benefit of 1 h pre-warming to be small. However, pre-warming mice did have the subjective benefit of improving the ease of tail-vein cannulation.

This study was limited by the relatively low numbers of mice in each group. Therefore the trends seen for some animal-handling conditions did not reach significance. Nevertheless, a high degree of repeatability was observed between animals. There was one significant outlier in the EL4 warm, fed group. The myocardial and tumour uptake in this animal correlated strongly with the EL4 warm, fasting group, fuelling speculation that the mouse may not have been taking advantage of the freely available food prior to the scan. Furthermore, in most fasted mice tumour-to-blood

ratios continued to rise throughout these scans. Owing to animal licence restrictions it was not possible to study mice continuously for ≥4 h.

In eleven of the twenty-eight scans phantoms containing approximately 1 MBq [^{18}F]FDG were included to ensure linearity throughout the 4 h acquisitions. This demonstrated that in time frames of ≤1 min in duration activity was under-estimated (Figure 3.16). This reflects a limitation of the PET scanner when reconstructing scans based on fewer counts. Consequently, the plasma integral was disproportionately underestimated and Patlak analysis was not possible. Time frames after 20 min post-injection were ≥2 min in duration, therefore the SUV and tumour-to-blood ratios reported are valid. Data were acquired in list-mode format and could be reconstructed in 2 min time frames from the start to permit kinetic analysis.

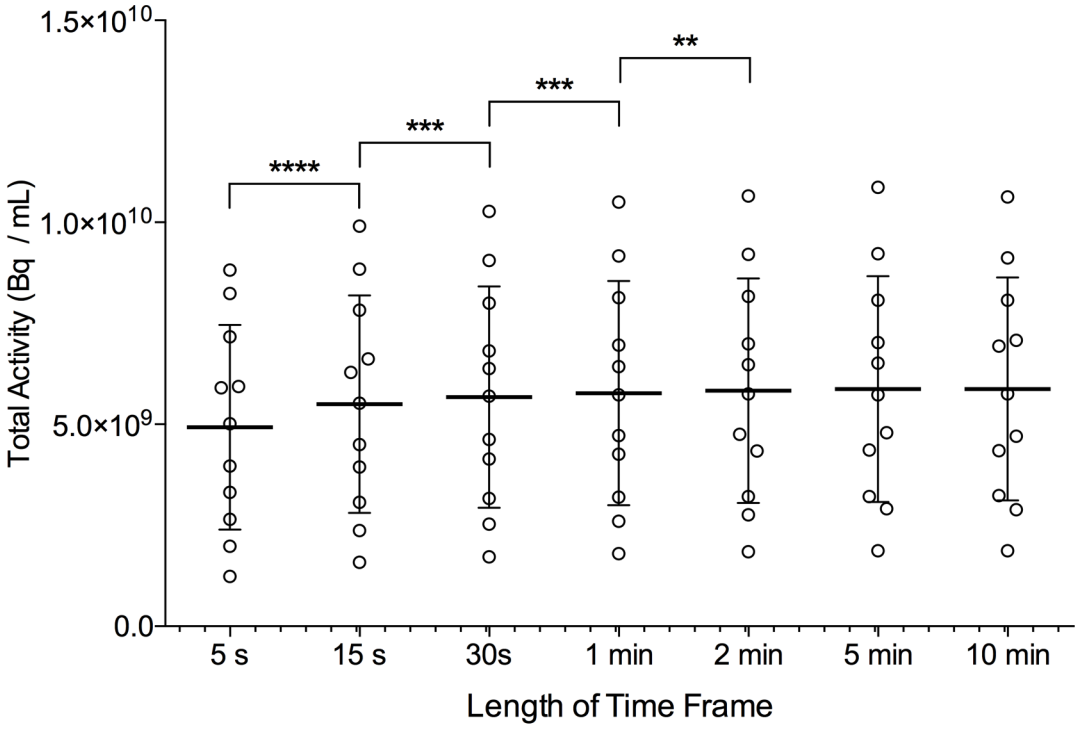

Figure 3.16. Underestimation of [^{18}F]FDG phantom activity (n = 11) in time frames of ≤1 min in duration.

Kinetic analysis would have been further aided by blood sampling, but this is technically challenging in mice. Previous studies have used a variety of different models to derive an input function from the vena cava, liver and left ventricle. Spill-in from the myocardium precluded the use of the left ventricle blood-pool and activity in the vena cava was found to be reproducible between studies, particularly at later time points. It should be noted that the limited PET resolution means that, despite locating the ROI in the upper abdomen where there was minimal uptake in nearby tissues, the vena cava ROI will also have contributions from other tissues, especially the aorta. This will limit absolute quantification of metabolic rates from [^{18}F]FDG uptake. However, these effects and the partial volume effect can be assumed to be similar between mice, permitting kinetic comparisons within this study.

3.5. Conclusions

These data demonstrate that animal handling has a significant effect on tumour [^{18}F]FDG-PET imaging, corroborating the findings of previous studies and permitting further refinement of a pre-clinical imaging protocol. Mice should be fasted prior to imaging, warmed when anaesthetised and, as per Fueger et al., should remain anaesthetised throughout the uptake and imaging period[187]. This suppresses background muscle and heart uptake and also increases tumour [^{18}F]FDG uptake. Warming prior to anaesthesia does not have a significant effect on imaging but should be considered to improve ease of cannulation.

For many purposes static imaging at 60 min post-injection is adequate. In this study uptake in autochthonous tumours had plateaued by this time but this was not the case for subcutaneous tumours. If optimal imaging is desired, studies performed

at later time-points will maximise tumour [^{18}F]FDG uptake and tumour-to-background ratios, particularly for mice in the fasted state.

4. Imaging treatment response with hyperpolarised [1-^{13}C]pyruvate and [^{18}F]FDG in EL4 murine lymphomas

4.1. Introduction

This is the first of three chapters investigating detection of treatment response in tumours using combined hyperpolarised [1-^{13}C]pyruvate and [^{18}F]FDG-PET imaging (hyper-PET). It describes imaging subcutaneous EL4 murine T-cell lymphomas before and 24 h after treatment with etoposide, a topoisomerase II inhibitor. Topoisomerase II relieves DNA supercoiling by causing transient double strand breaks, passing an intact helix through the gap and then re-ligating the helix. Etoposide inhibits the re-ligation step, the result being an accumulation of topoisomerase II-induced double stranded DNA breaks, activating apoptosis[218, 219]. Additionally, etoposide induces mitochondrial ROS accumulation which inhibits oxidative phosphorylation in a complex-I dependent manner and enhances activation of apoptosis[220]. 24 h after etoposide treatment EL4 tumours have previously been shown to decrease in size and there is decreased lactate/pyruvate exchange and [^{14}C]FDG uptake[69, 107]. This chapter builds on this previous work by comparing hyperpolarised [1-^{13}C]pyruvate and [^{18}F]FDG in the same cohort of animals and using [^{18}F]FDG-PET imaging instead of *ex vivo* scintillation counting of [^{14}C]FDG.

Fourteen EL4 tumour-bearing mice completed hyper-PET imaging before and after treatment. There was a decrease in tumour [^{18}F]FDG uptake in all animals after treatment. Initially, labelled lactate/pyruvate ratios were calculated from magnetic resonance spectroscopy measurements but these were superseded by the development of 2D spectral-spatial (SpSp) echo planar imaging (EPI) and 3D SpSp dual spin echo (DSE) imaging sequences[149, 221]. With all three methods tumour [1-^{13}C]lactate/[1-^{13}C]pyruvate ratio changed variably in response to treatment. These results were partially explained from *ex vivo* tumour protein expression data showing that treatment decreased GLUT1 and GLUT3 expression but did not change

expression of MCT1, MCT4 and LDH or tumour lactate concentration. Poly(ADP-ribose) polymerase (PARP) cleavage, previously correlated with a decrease of NAD(H) availability in tumour cells *in vitro*, was unchanged by treatment in tumours *in vivo*[69]. Furthermore, before and after treatment there was highly variable terminal deoxynucleotidyl transferase nick-end labelling (TUNEL) and cleaved caspase 3 (CC3) staining, histological markers of cell death, potentially accounting for the variable response to treatment detected using hyperpolarised [1-^{13}C]pyruvate[69, 107].

4.2. Methods

The following methods described in "Chapter 2 - Methods" are used in this chapter:

2.1. Animal licence statement

2.2. EL4 cell culture, tumour growth and treatment

2.6. Anaesthesia of mice

2.7. Hyperpolarisation of [1-^{13}C]pyruvate

2.8. Western blotting

2.9 Lactate dehydrogenase (LDH) activity assay

2.10. Immunohistochemistry (IHC)

2.11. Statistical analysis

4.2.1. Animal preparation

EL4 tumour-bearing mice were fasted for 8 – 12 h prior to anaesthesia and imaging. The tail vein was cannulated and 10.2 ± 1.0 MBq [^{18}F]FDG injected intravenously.

4.2.2. Tumour volume estimates

Tumour volumes were estimated from calliper measurements using the equation:

$$\text{Volume} = \frac{xy^2}{2}$$

where x and y are the maximum tumour diameters of two perpendicular planes[222].

4.2.3. ^{13}C MR spectroscopy of EL4 tumours

Experiments were performed in a 7.0 T horizontal bore magnet (Agilent, Palo Alto, CA, USA) using an actively decoupled dual-tuned ^{13}C/^{1}H volume transmit coil (Rapid Biomedical, Rimpar, Germany) and a 20 mm diameter ^{13}C receiver coil (Rapid Biomedical). For anatomical reference, T_2-weighted ^{1}H images were acquired using a fast spin-echo (FSE) pulse sequence. Twenty axial images were acquired with a slice thickness of 1 mm, repetition time (TR) 2.24 s, echo time (TE) 48 ms, 2 – 4 averages, data matrix 256 × 256, FOV 40 × 40 mm. Coronal and sagittal ^{1}H images had a slice thickness of 2 mm, TR 2.05 s, TE 48 ms, 2 averages, data matrix 512 × 256, FOV 80 × 40 mm. Injection of [1-^{13}C]pyruvate was delayed until at least 40 minutes after [^{18}F]FDG injection to minimise the possible effect of pyruvate on [^{18}F]FDG uptake. Immediately after injection of 200 µL ~75mM [1-^{13}C]pyruvate, single transient spectra were acquired each second for three minutes from a 10 mm thick slice through the tumour using a slice-selective excitation pulse with nominal 5° flip angle, spectral width of 6010 Hz and 1024 spectral points. Spectra were summed, peak-fitted and the labelled lactate/pyruvate area under the curve (AUC) ratios calculated using MATLAB (MathWorks, Natick, MA, USA).

4.2.4. 2D echo planar imaging (EPI) of hyperpolarised [1-^{13}C]pyruvate and [1-^{13}C]lactate

A 6 mm axial ^{1}H reference slice was acquired using the FSE sequence as above. The ^{13}C imaging sequence acquired a 2D EPI *k*-space, starting with a spectral-spatial (SpSp) excitation pulse and slice selection gradient, followed by a train of 20 bipolar readout gradients and, simultaneously, a train of 19 blipped phase-encoding gradients (Figure 4.1). A 6 mm axial slice was selected covering the tumour with a FOV 40 × 40 mm. The acquisition matrix was 32 × 32, but only four *k*-space lines were acquired before the centre of *k*-space in order to minimise the echo time (TE) and enhance the SNR. Hence, only 20 bipolar readout gradients were used (acquiring 62.5% of *k*-space). The SpSp RF pulse alternately excited the [1-^{13}C]pyruvate and [1-^{13}C]lactate resonances with a TR of 2 s for each metabolite. The RF pulse had a duration of 15.936 ms, 200 Hz passband width, 1412 Hz between replicate bands and a targeted a 15° flip angle using a peak RF power of 0.0386 Gauss. The receiver bandwidth was set to 125 kHz with an echo spacing of 536 μs and bandwidth per pixel in the phase encoding direction of 58.3 Hz. The sequence was started immediately following injection of [1-^{13}C]pyruvate[221]. Images were acquired over 60 s and analysed in MATLAB (Mathworks, Natick, MA, USA). A 2D ROI over the tumour was defined using the ^{1}H reference scan. Labelled lactate/pyruvate AUC ratios were calculated from the area under the curve of their respective time courses.

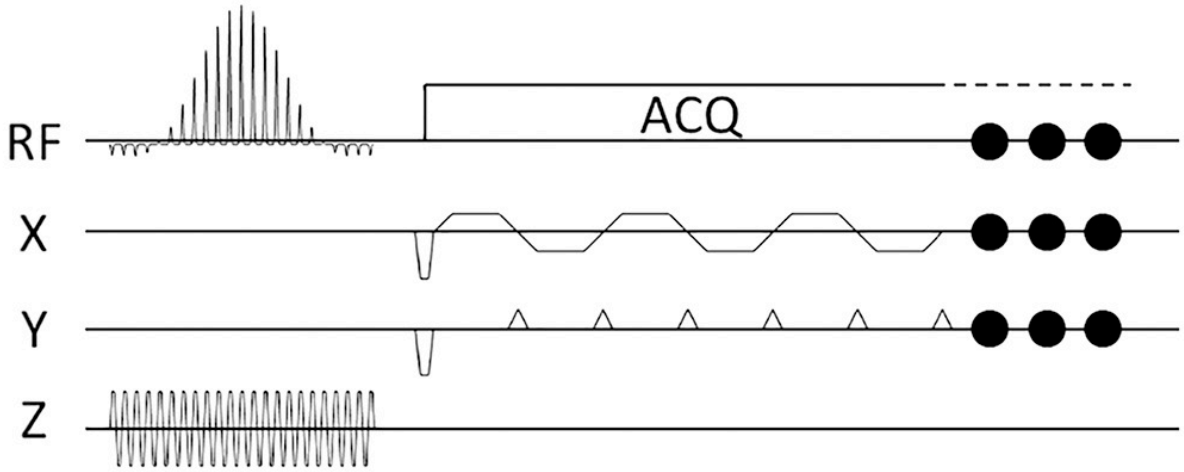

Figure 4.1. EPI sequence for 2D ^{13}C imaging.

4.2.5. 3D dual spin echo (DSE) ^{13}C imaging of [1-^{13}C]pyruvate and [1-^{13}C]lactate

^{13}C images were acquired using a SpSp pulse sequence and 3D spiral DSE acquisition (Figure 4.2)[223]. The SpSp excitation pulse alternately excited [1-^{13}C]pyruvate and [1-^{13}C]lactate resonances (calculated from the measured water proton frequency) at a temporal resolution of 2 s per metabolite. The eighth pair of acquisitions was used as a reference scan where the z-gradients were turned off except for the slice selection gradient and the spoiler. A spherical stack of spirals was acquired at two spin echoes after a single excitation pulse. Flip angles were 15º for [1-^{13}C]pyruvate and 90º for [1-^{13}C]lactate, respectively, FOV was 40 × 40 × 20 mm with a nominal spatial resolution was 1.25 × 1.25 × 2.5 mm in the x, y and z planes, respectively. In initial experiments the sequence started immediately after rapid injection of hyperpolarised [1-^{13}C]pyruvate (15 mL/kg). [1-^{13}C]pyruvate and [1-^{13}C]lactate images were acquired alternately each second for 90 s and analysed in MATLAB (Mathworks, Natick, MA, USA). A 3D region of interest (ROI) over the tumour was defined on the T_2-weighted image. The [1-^{13}C]lactate/[1-^{13}C]pyruvate signal ratio was calculated from the area under the curve of their respective time courses.

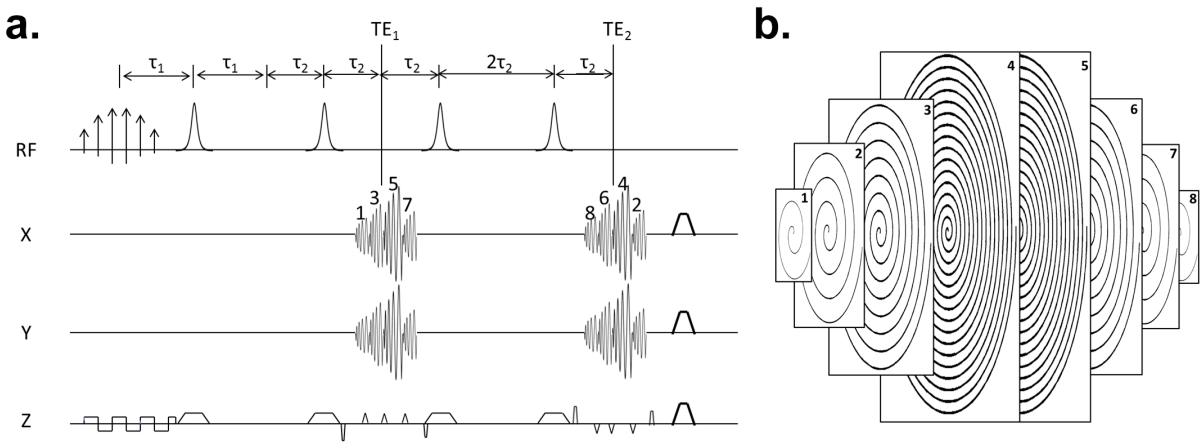

Figure 4.2. (a) 3D ^{13}C imaging pulse sequence and (b) its 3D *k*-space trajectory.

4.2.6. [^{18}F]FDG-PET imaging

After MR acquisition the bed with the mouse *in situ* was transferred to a NanoPET/CT (Mediso, Budapest, Hungary) for a 30 min PET acquisition starting at 60 min post [^{18}F]FDG injection. A helical CT was acquired for anatomical reference and attenuation correction (acquisition settings: 65 kVp, 1100 ms exposure, maximum FOV, 360 projections). Static PET images, with a nominal isotropic resolution of 0.3 mm, were reconstructed using a 3D ordered-subset expectation maximization method using a one to three coincidence mode, eight iterations and six subsets. Images were normalised and corrected for decay, dead time, random events and attenuation. Images were analysed using VivoQuant v2.00 software (InviCRO, Boston, MA, USA). A 3D region of interest (ROI) was drawn manually over the tumour and Otsu thresholding used to delineate the tumour. For semi-quantitative analysis, mean and maximum standardized uptake values (SUV) were calculated using:

$$SUV = \frac{c_{img}}{ID/BW}$$

where c_{img} is the activity (expressed as MBq/mL) derived from the image ROI, ID is the injected dose (MBq) and BW is the body weight (g) of the animal.

4.2.7. Tumour lactate quantification

Tumour extracts were deproteinised by the addition of 5 µL/mg tissue 2 M perchloric acid (PCA) and homogenisation using a Precellys 24 homogeniser (Stretton Scientific, Stretton, UK). Samples were centrifuged at 13,000 *g* for 2 min and the supernatant pH corrected to 7.0 with 2 M KOH. Samples were centrifuged at 13,000 *g* for 15 min and the supernatant taken for analysis. Colourimetric quantification of lactate was performed using an L-lactate assay kit (ab65331, Abcam, Cambridge, UK) and the A_{450} measured using a PHERAstar FS microplate reader.

4.3. Results

4.3.1. *In vitro* response of EL4 cells to etoposide treatment

The response of EL4 cells to etoposide was confirmed *in vitro* by the addition of 15 µM etoposide to cell suspensions (Figure 4.3). After 8 h the cell proliferation ratio (number of viable cells at t = x / number of viable cells at t = 0) was 1.5 ± 0.3 (n = 6) in untreated flasks and 1.2 ± 0.1 (n = 12, P = 0.004) in those treated with etoposide. After 20 h of culture the cell proliferation ratio increased to 3.1 ± 0.7 (n = 6) in untreated flasks but dropped to 0.77 ± 0.1 (n = 12) in etoposide-treated flasks, representing a significant inhibition of proliferation (P = <0.0001).

4.3.2. *In vivo* volume response of EL4 tumours to etoposide treatment

Tumours were grown by subcutaneous implantation of EL4 cells in the flanks of mice. Tumours increased in volume up to nine days post-implantation and were then treated with a single dose of etoposide i.p. (Figure 4.4). Treatment resulted in a decrease in volume of all tumours within 24 h, with a mean decrease of 19.5 ± 11% (n = 8, P = 0.0014). In six out of eight tumours the decrease in volume was sustained

and tumours disappeared completed in <18 days. In two mice tumours started to grow 5 – 6 days after treatment. Treatment also resulted in a decrease in bodyweight in all mice from 22.4 ± 1.7 to 20.4 ± 1.0 g (n = 9; *P* = 0.0003) 24 h after treatment.

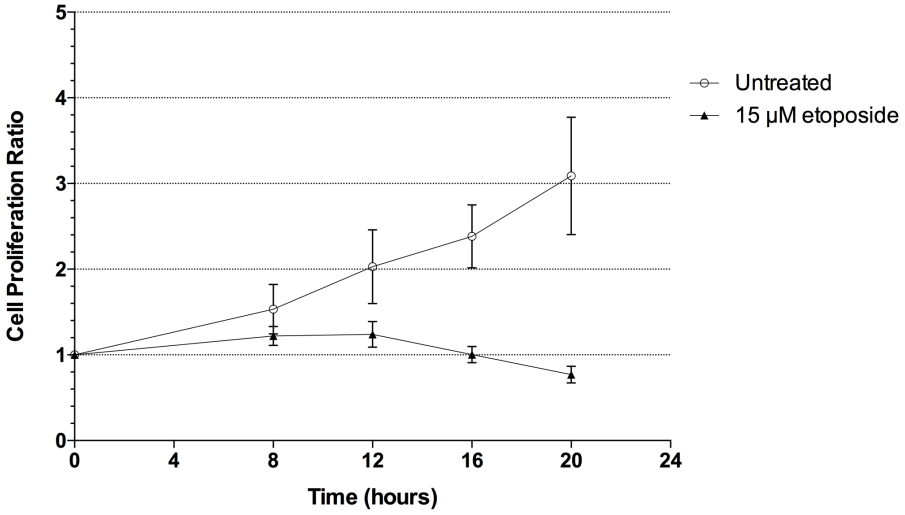

Figure 4.3. The change in number of viable EL4 cells in response to 15 μM etoposide *in vitro.* The cell proliferation ratio is the (number of viable cells at t = x / number of viable cells at t = 0).

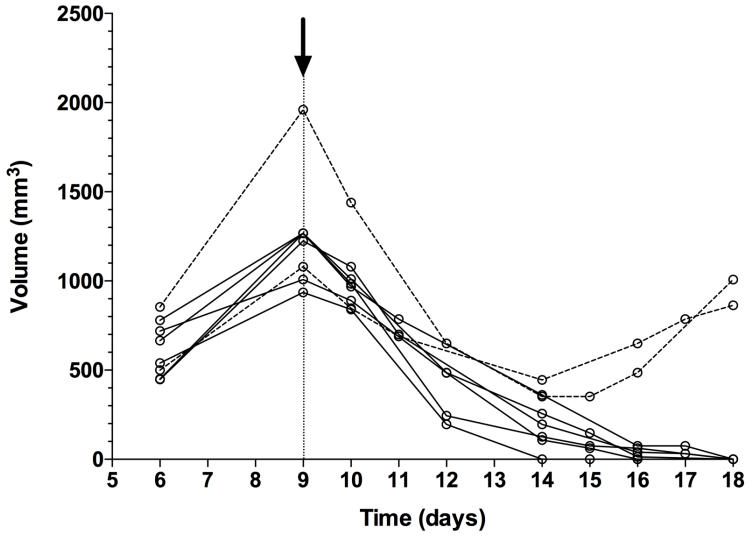

Figure 4.4. Response of EL4 tumours etoposide. Mice (n = 8) received a single intraperitoneal dose of 67 mg/kg etoposide at day 9 (arrow) post-implantation. The solid lines indicate mice that responded completely to etoposide while the dotted lines indicate two mice with tumours that started to grow again 5 – 6 days after treatment.

4.3.3. Imaging of early treatment response with hyperpolarised [1-^{13}C]pyruvate and [^{18}F]FDG-PET

MR and [^{18}F]FDG-PET imaging was completed in fourteen EL4 tumour-bearing mice. [^{18}F]FDG uptake decreased in all tumours 24 h after etoposide treatment, with SUV_{max} decreasing from 8.8 ± 1.8 pre-treatment to 5.2 ± 0.84 post-treatment (n = 14, *P* = <0.0001) (Figure 4.5).

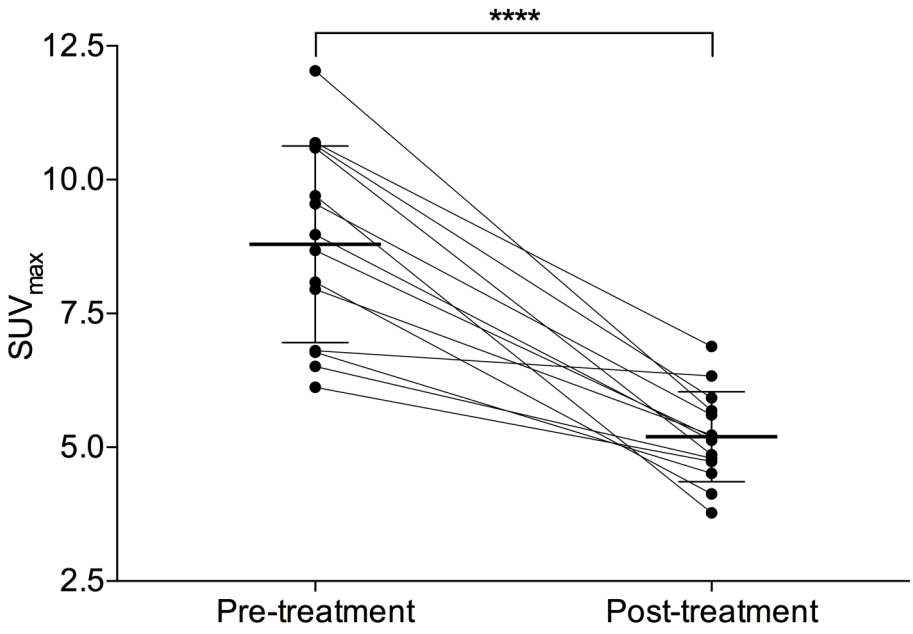

Figure 4.5. EL4 tumour SUV_{max} before and 24 h after treatment with etoposide.

MR spectroscopy, 2D SpSp EPI ^{13}C imaging and 3D DSE ^{13}C imaging was performed in seven, four and three mice, respectively (Figure 4.6). There was no significant change in mean [1-^{13}C]lactate/[1-^{13}C]pyruvate ratio in EL4 tumours which were 1.87 ± 1.1 before and 1.73 ± 1.0 after treatment. Despite the lack of reduction in labelled lactate/pyruvate ratio after treatment, the imaging methods demonstrated a similar distribution of [^{18}F]FDG uptake and [1-^{13}C]lactate production (Figure 4.6).

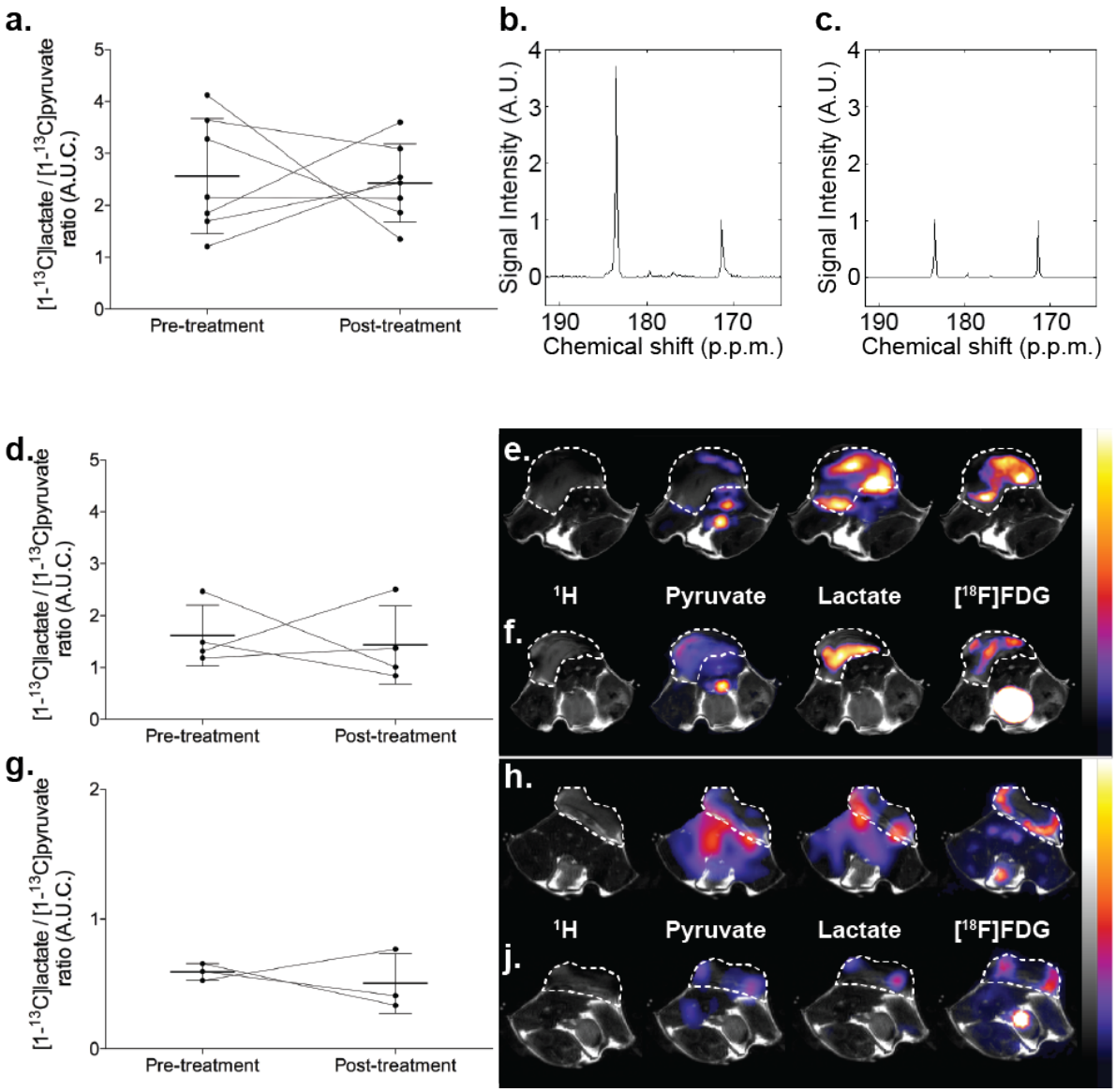

Figure 4.6. EL4 tumour [1-^{13}C]lactate/[1-^{13}C]pyruvate ratio before and 24 h after etoposide treatment. (a) Tumour lactate/pyruvate ratios measured using magnetic resonance spectroscopy; **(b)** example summed spectrum before and **(c)** after treatment. The [1-^{13}C]pyruvate and [1-^{13}C]lactate resonances are at 173 p.p.m. and 185 p.p.m., respectively. **(d)** Tumour lactate/pyruvate ratios measured using 2D EPI ^{13}C imaging and example images **(e)** before and **(f)** after treatment **(g)** Tumour lactate/pyruvate ratios measured using 3D DSE ^{13}C imaging (note the reduced scale) and an example axial slice through the middle of the tumour **(h)** before and **(j)** after treatment. Pre- and post-treatment images are on the same scale.

4.3.4. The effect of etoposide treatment on protein expression, LDH activity and lactate concentration in EL4 tumours

Tumour expression of the enzymes and transporters involved in [^{18}F]FDG uptake and [1-^{13}C]pyruvate uptake and reduction to [1-^{13}C]lactate were investigated by western blotting (Figure 4.8). GLUT1 expression decreased (relative to β-actin) from 0.035 ± 0.009 (n = 5) to 0.016 ± 0.006 (n = 9, *P* = 0.0006) 24 h after etoposide treatment. GLUT3 expression also decreased after treatment from 0.020 ± 0.007 (n = 5) to 0.007 ± 0.005 (n = 9, *P* = 0.0012). HK2, responsible for phosphorylation and subsequent trapping of [^{18}F]FDG, was not affected by etoposide treatment. The expression of MCT1 and MCT4, responsible for pyruvate and lactate membrane transport, were not significantly altered by treatment although there was a non-significant increase in MCT1 expression after treatment (*P* = 0.08). LDH expression, activity and the tumour lactate concentration were not affected by treatment (Figure 4.7 and 4.8). There was also no change in PARP cleavage, previously correlated with NAD(H) depletion *in vitro*[69, 107].

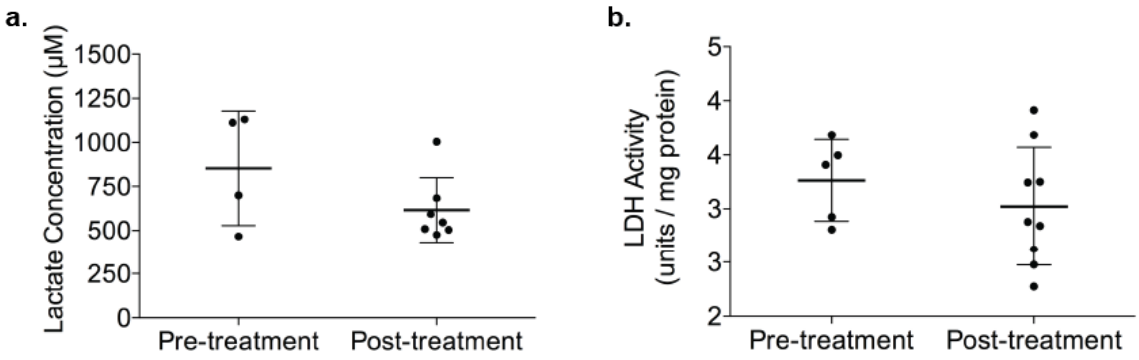

Figure 4.7. (a) EL4 tumour lactate concentration and (b) LDH activity before and after etoposide treatment.

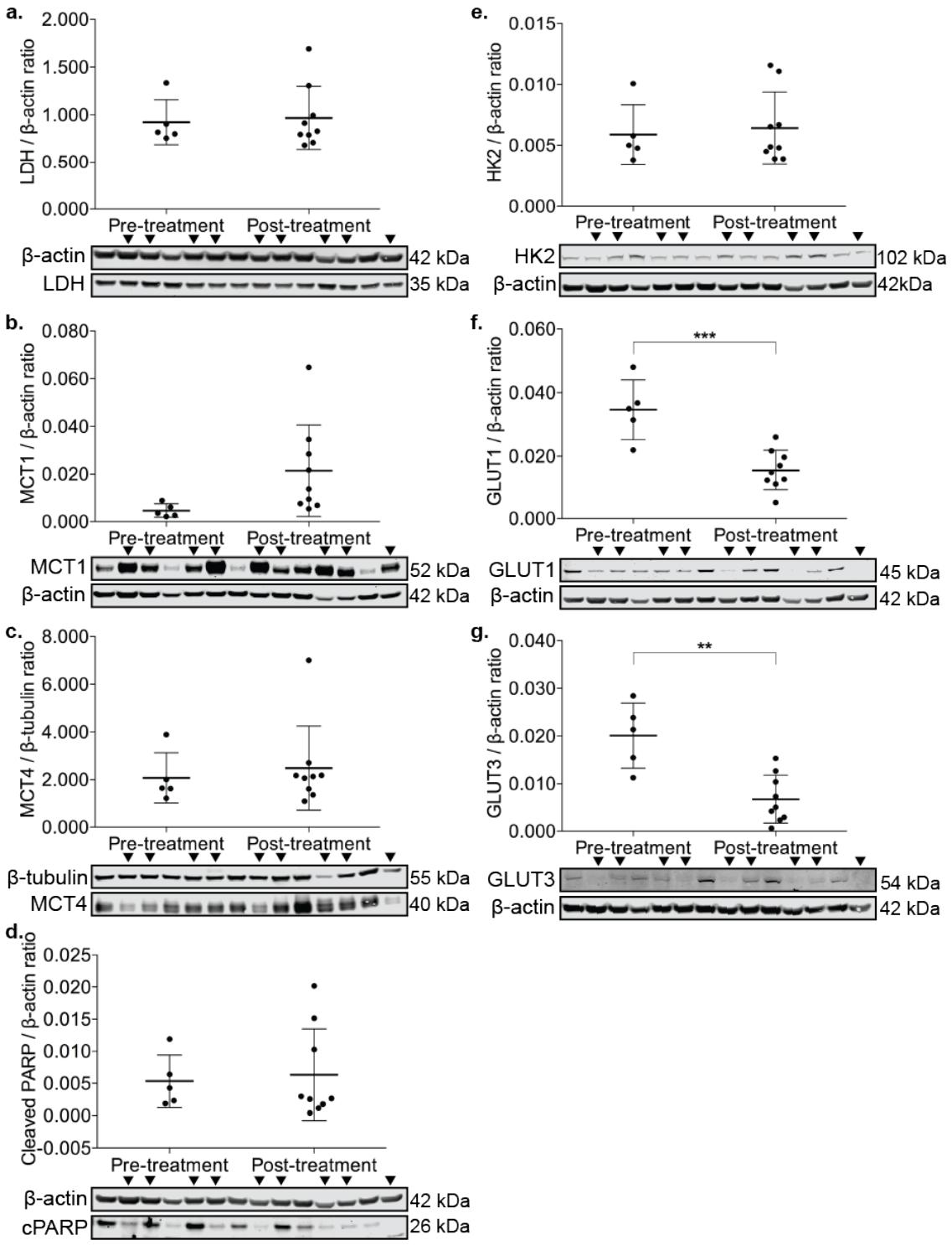

Figure 4.8. Changes in membrane transporter and enzyme expression in EL4 tumours 24 h after etoposide treatment. Arrows above the western blots indicate post-treatment tumour samples. Expression of: **(a)** LDH-A; **(b)** MCT1; **(c)** MCT4; **(d)** cleaved PARP; **(e)** HK2; **(f)** GLUT1; **(g)** GLUT3 expression and **(h)** HK2 expression. Abbreviations: cPARP – cleaved PARP.

4.3.5. TUNEL and CC3 IHC in EL4 tumours

Histological markers of cell death did not manifest a significant effect of etoposide treatment (Figure 4.9).

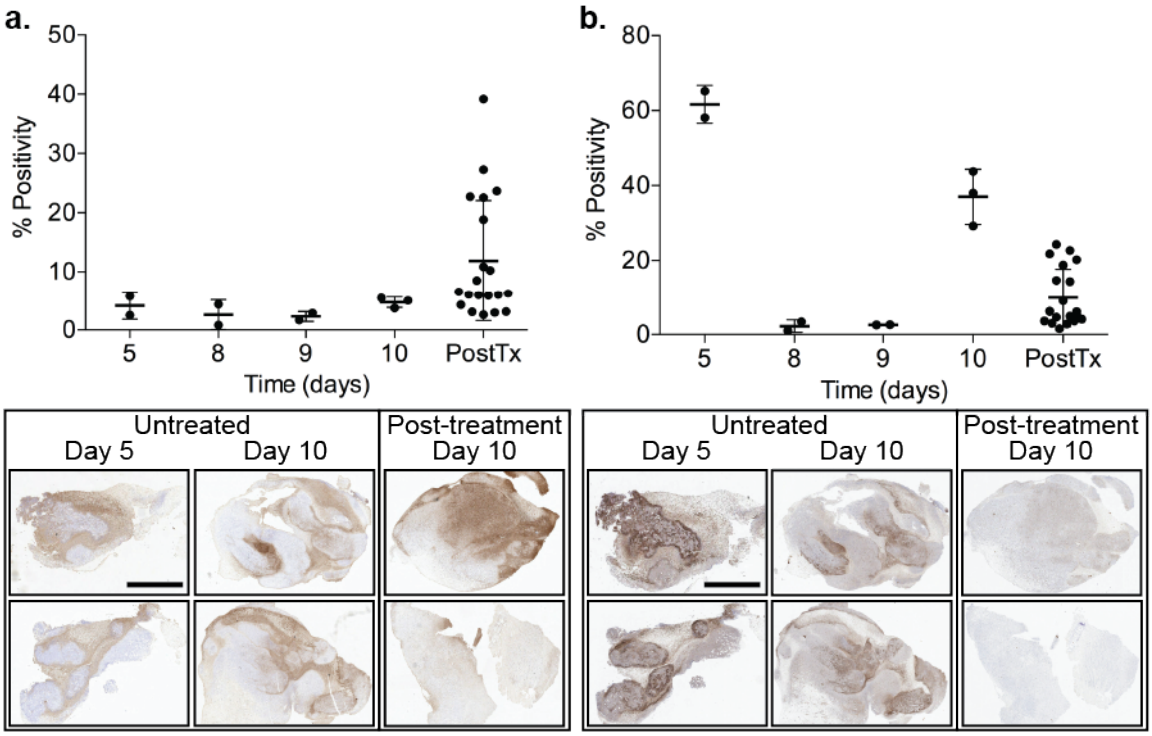

Figure 4.9. (a) TUNEL and (b) CC3 immunohistochemistry in untreated and etoposide-treated tumours with corresponding sections for each stain underneath each graph. Two sections are shown from different tumours excised at day five and day ten pre-treatment and day ten post-treatment. All images are identically scaled and the scale bars are 5 mm. Abbreviations: PostTx – post-treatment.

± 1.7% in tumours excised after eight days. By day ten it had increased to 37 ± 7.4% in untreated tumours but was only 9.9 ± 7.7% in post-treatment tumours. The implication from the histopathology results is that, independent of etoposide treatment, cell death in EL4 tumours is highly variable, particularly when assayed by CC3 immunohistochemistry.

Tumours were excised at five, eight, nine and ten days post-implantation in untreated mice. Mice were treated on day nine with etoposide and tumours excised 24 h later (day ten post-implantation). TUNEL positivity was fairly constant in untreated tumours excised between five and ten days and increased non-significantly from 4.75 ± 0.9 % in day ten untreated tumours to 11.84 ± 10.2 % in post-treatment tumours. CC3 staining was highly variable in untreated tumours. At day five CC3 positivity was 61.65 ± 5.0% but was only 2.26

4.4. Discussion

This study demonstrates the feasibility of imaging mice using hyperpolarised [1-^{13}C]pyruvate MRI/S and [^{18}F]FDG-PET in a single session (<2 h) before and after treatment. Furthermore, the use of ^{13}C imaging techniques allowed the spatial distributions of [1-^{13}C]pyruvate, [1-^{13}C]lactate and [^{18}F]FDG to be compared. Lacking a combined PET/MRI scanner, this was achieved by transferring the mouse bed between the MRI and PET/CT, permitting co-registration of MR and PET/CT images. The limited resolution of the ^{13}C images, particularly in the z dimension (6 mm for the 2D EPI sequence and a nominal 2.5 mm for the 3D DSE sequence) is a limiting factor when comparing with PET images. Nevertheless, the distribution of [^{18}F]FDG uptake and [1-^{13}C]lactate production were similar in 2D and 3D images.

To compare detection of tumour treatment response between the two metabolic imaging techniques the EL4 tumour model was chosen for its rapid growth, sensitivity to the topoisomerase II inhibitor etoposide and availability of similar previous studies[69, 107]. Treatment resulted in a decrease in tumour size of approximately 20% in 24 h, replicating the findings of Day et al.[107]. Treatment also resulted in a 41% decrease in [^{18}F]FDG uptake, very similar to the 38% decrease in [^{14}C]FDG uptake observed by

Witney et al.[69]. In that study the decrease in [^{14}C]FDG uptake was attributed to decreased plasma membrane expression of GLUT1 and GLUT3, observed *in vitro*. In contrast, in this study there was decrease in *total* GLUT1 and GLUT3 expression in the tumours *in vivo*.

Unexpectedly, this study failed to demonstrate a consistent decrease in exchange between labelled pyruvate and lactate, contrary to the findings of Witney et al. and Day et al. who reported decreases in flux between pyruvate and lactate of 38 and 25%, respectively[69, 107]. Notably, Witney et al. reported a significant reduction in [^{18}F]FDG uptake at only 16 h post-treatment, preceding a decrease in pyruvate/lactate exchange[69]. However, *ex vivo* tumour analysis revealed important differences between the EL4 models used in this study and the previous work. Previously cell death after etoposide treatment was reported to increase by approximately 32%[107]. In the current study TUNEL staining only increased by approximately 7% and at day 10 CC3 positivity decreased by approximately 27%. The EL4 cells used in the current study were derived from cells obtained from ATCC in 2014 and were not the same as those used in previous studies. In studies (including this one) using the new cells we have observed highly variable pre-treatment cell death. Furthermore, treatment did not result in reductions in LDH activity, lactate concentration, LDH and MCT expression, that would limit flux between pyruvate and lactate. Over-activation of PARP in response to etoposide-induced DNA damage has previously been correlated with NAD(H) depletion and subsequent reduction in pyruvate to lactate flux *in vitro*[69, 107]. PARP inactivation by caspase-3 is a hallmark of apoptosis and has been observed on a similar timescale[69]. Again, this study did not demonstrate any difference in PARP cleavage before and after treatment with etoposide.

In addition to the biological explanations for the lack of treatment response detectable using hyperpolarised [1-^{13}C]pyruvate, there were also technical limitations. The fast imaging sequences developed here enabled 3D *in vivo* spatial comparisons between [1-^{13}C]pyruvate, [1-^{13}C]lactate and [^{18}F]FDG. Initially, the SNR and reproducibility of the 3D DSE sequence was low. The high flip angles (15º and 90º for [1-^{13}C]pyruvate and [1-^{13}C]lactate, respectively) and imaging from the start of injection resulted in depletion of the polarisation and available signal in <15 s. Improvements were made by three alterations to the sequence and injection protocol. The flip angles were reduced to 5º and 45º for [1-^{13}C]pyruvate and [1-^{13}C]lactate, respectively. The injection protocol was changed to an infusion over 8 s, instead of a rapid bolus, and the imaging sequence was commenced 2 s after the start of injection. Five [1-^{13}C]pyruvate images were acquired with a 2 s frame rate for the first five seconds before the first acquisition of a [1-^{13}C]lactate image. Thereafter [1-^{13}C]pyruvate and [1-^{13}C]lactate images were acquired alternately each second. These alterations improved SNR and preserved signal for >60 s. This improved version of the sequence and injection protocol is used in Chapters 5 & 6.

4.5. Conclusions

This study demonstrates the feasibility of combined *in vivo* imaging using hyperpolarised [1-^{13}C]pyruvate MRI and [^{18}F]FDG-PET. Here these measurements were used to detect response of EL4 tumours to etoposide. 24 h after treatment there was a reduction in tumour volume and [^{18}F]FDG uptake. Contrary to previous findings, treatment did not consistently decrease flux between [1-^{13}C]pyruvate and [1-^{13}C]lactate, possibly due to variable amounts of cell death before and after treatment.

This study indicates that, for some tumours and chemotherapeutic agents, [^{18}F]FDG may be a more sensitive marker of response to treatment than [1-^{13}C]pyruvate.

5. Imaging treatment response with hyperpolarised [1-^{13}C]pyruvate and [^{18}F]FDG in Eμ-*Myc* lymphomas

5.1. Introduction

The vast majority of *in vivo* pre-clinical imaging studies have been performed using subcutaneous models. Most models are fast growing and reproducible, allowing large numbers of tumours to be grown at relatively low cost. Subcutaneous implants permit tumour growth to be monitored non-invasively and, of particular importance for MRI studies, tumours can be fixed externally to minimise movement artefacts and optimise SNR. However, the artificial site, lack of diversity in the tumour microenvironment, poor perfusion, a rodent immune system (which is immunocompromised when used for human tumour cell lines) and frequent use of cell lines that have been passaged for decades leads to most subcutaneous tumours bearing little resemblance to the human disease they model[224, 225]. Orthotopic models offer an improvement by growing at a more natural site but still have the other limitations of implanted tumours.

Of all the available models genetically engineered mouse (GEM) cancer models provide the most complete representation of tumour development, progression, stroma, immune system interaction and angiogenesis[226]. Although the "natural" development of autochthonous tumours has significant advantages for modelling disease, the models are invariably challenging to work with. Animals have many of the associated morbidities associated with cancer, e.g., ascites, neurological deficits and respiratory compromise. This is particularly challenging for imaging research as the mice often poorly tolerate prolonged anaesthesia. Relatively slow and variable rates of tumour development are often combined with a small window of opportunity between the appearance of tumours and study-limiting morbidity. Furthermore, the greater heterogeneity of tumours that develop is not always an advantage in a pre-clinical setting[226].

The Eμ-*Myc* GEM model was developed in the late 1980s by injection of the Eμ-*Myc* transgene into the pronucleus of fertilized mouse eggs[189, 227]. The transgene consists of a normal *Myc* gene coupled to the Ig heavy chain (*IgH*) enhancer mimicking the t(8;14) translocation seen in most Burkitt's lymphomas. The transgene is expressed exclusively in B lymphocytes of the mice and results in development of pre-B and B lymphomas. Typically within six months mice develop lymphomas (inguinal, axillary, cervical, para-thymic and para-aortic), thymomas, small bowel and intracranial tumours and a subset also have a leukaemia component to their disease[189]. Furthermore, sensitivity of Eμ-*Myc* tumours to cyclophosphamide, a nitrogen mustard that alkylates guanine residues of DNA leading to apoptosis, has been described previously[228, 229].

The aim of this study was to compare hyperpolarised [1-^{13}C]pyruvate and [^{18}F]FDG-PET as methods to detect response 24 h after treating Eμ-*Myc* tumours with cyclophosphamide. ^{13}C MRS and CSI with [1-^{13}C]pyruvate were used in an initial cohort of six mice as the experiments pre-dated the development of more sophisticated sequences. The MRS measurements suggested that treatment resulted in a mean decrease of 71% in the apparent k_{PL} in cervical tumours. However, in a separate cohort imaged with [^{18}F]FDG-PET, although there was an obvious decrease in the size of all tumours, [^{18}F]FDG uptake in the cervical tumours was difficult to interpret due to significant uptake in normal surrounding tissues, particularly in muscle and the salivary glands. The effect of contributions of surrounding tissues was elucidated by autoradiography and co-registered histology. Subsequently, by drawing a small ROI over the tumour regions, spill-in was avoided and a 42% decrease in [^{18}F]FDG uptake was observed.

In the initial cohort, mice were awake during the [^{18}F]FDG uptake period due to concerns about the animals tolerance of prolonged anaesthesia. In a cohort of mice undergoing simultaneous 3D MRI with hyperpolarised [1-^{13}C]pyruvate and [^{18}F]FDG-PET the uptake in normal tissues was substantially reduced by mice remaining anaesthetised throughout the uptake period. Similar decreases in labelled pyruvate to lactate exchange, [^{18}F]FDG uptake and tumour volume were observed in this cohort. Unfortunately there were significant limitations of the model. Not only was there a high mortality rate from imaging but the effect of animal handling and anaesthesia resulted in control mice having similar decreases in tumour volume, pyruvate to lactate exchange and [^{18}F]FDG uptake to mice treated with cyclophosphamide.

5.2. Methods

The following methods described in "Chapter 2 - Methods" are used in this chapter:

2.1. Animal licence statement

2.5. Eμ-*Myc* transgenic mouse breeding, genotyping and treatment

2.6. Anaesthesia of mice

2.7. Hyperpolarisation of [1-^{13}C]pyruvate

2.11. Statistical analysis

5.2.1. Animal preparation

Mice were kept in a warmed chamber (31 ºC) for 1 h prior to anaesthesia before all procedures requiring intravenous injection or imaging.

5.2.2. Hyperpolarised [1-^{13}C]pyruvate MRS and chemical shift imaging (CSI)

NMR / MRI was performed in a 7.0 T horizontal bore magnet (Agilent, Palo Alto, CA, USA) using an actively decoupled dual-tuned ^{13}C/^{1}H volume transmit coil (Rapid Biomedical, Rimpar, Germany) and a 20 mm diameter ^{13}C receiver coil (Rapid Biomedical). For anatomical reference, T_2-weighted ^{1}H images were acquired using a fast spin-echo (FSE) pulse sequence. Twenty axial images were acquired with a slice thickness of 1 mm, repetition time (TR) 2.245 s, echo time (TE) 48 ms, 2 – 4 averages, data matrix 256 × 256, FOV 40 × 40 mm. Coronal and sagittal ^{1}H images had a slice thickness of 2 mm, TR 2.05 s, TE 48 ms, 2 averages, data matrix 512 × 256, FOV 80 × 40 mm. Spectroscopic measurements were made using a 10 mm oblique slice through the cervical tumour. Immediately after injection of 400 µL hyperpolarised [1-^{13}C]pyruvate single transient spectra were acquired each second for three minutes from a 10 mm thick slice through the tumour using a slice-selective excitation pulse with a nominal 5° flip angle, spectral width of 6010 Hz and 1024 data points. ^{13}C spectroscopic data were processed using MATLAB (MathWorks, Natick, MA, USA). The integrated peak intensities of hyperpolarised [1-^{13}C]pyruvate and [1-^{13}C]lactate were fitted to the modified Bloch equations for two-site exchange to obtain the rate constants, k_{LP} and k_{PL}, and the apparent spin-lattice relaxation rates:

$$\mathrm{L} \underset{k_{PL}}{\overset{k_{LP}}{\rightleftharpoons}} \mathrm{P}$$

$$\frac{dL_Z}{dt} = -R_{1,L}(L_Z - L_\infty) + k_{PL}P_Z - k_{LP}L_Z$$

$$\frac{dP_Z}{dt} = -R_{1,P}(P_Z - P_\infty) + k_{LP}L_Z - k_{PL}P_Z$$

where L is lactate, P is pyruvate, L_Z and P_Z are the z-magnetisations of the ^{13}C nucleus for the lactate and pyruvate carboxyl carbons, t is time, $R_{1,L}$ and $R_{1,P}$ are the spin-

lattice relaxation rates ($1/T_1$) for lactate and pyruvate, respectively, and L_∞ and P_∞ are their equilibrium magnetisations, which are effectively equivalent to their concentrations. The relaxation rates were assumed to be the same for lactate and pyruvate.

Chemical shift images were acquired from a 6 mm axial slice through the tumour between 20 and 50 s after injection of hyperpolarised [1-^{13}C]pyruvate. The imaging sequence was the same as that used for the spectroscopic measurements, with additional phase-encoding gradients preceding signal acquisition (TR, 30 ms; TE, 0.85 ms; spectral width, 6010 Hz; spectral points, 128; FOV, 40 × 40 mm; data matrix, 32 × 32). ^{13}C MRS was performed by Tiago Rodrigues and Mikko Kettunen.

5.2.3. [^{18}F]FDG-PET imaging

Mice were anaesthetised and 9.4 ± 1.2 MBq of [^{18}F]FDG injected *via* tail vein. Mice were awakened after injection and kept in the warming box before being re-anaesthetised prior to a 10 min PET acquisition at 90 min post-injection. Static PET images, with a nominal isotropic resolution of 0.3 mm, were reconstructed using a 3D ordered-subset expectation maximisation method, a one to three coincidence mode, eight iterations and six subsets. Images were normalised and corrected for decay, dead time, random events and attenuation. Images were analysed using VivoQuant v2.00 software (InviCRO, Boston, MA, USA). A 3D ROI was manually drawn over the cervical tumour and Otsu thresholding used to delineate the tumour.

5.2.4. Combined [^{18}F]FDG-PET and 3D-DSE ^{13}C imaging of [1-^{13}C]pyruvate and [1-^{13}C]lactate

Venous glucose concentration was measured using a StatStrip Xpress glucose meter (Nova Biomedical, Waltham, MA, USA) prior to imaging. [^{18}F]FDG (12.7 ± 0.8 MBq) (Alliance Medical, Guildford, UK) was injected intravenously and mice remained anaesthetised throughout the uptake period. MRI was performed in a 7.0 T horizontal bore magnet (Agilent, Palo Alto, CA) using an actively decoupled dual-tuned ^{13}C / ^{1}H volume transmit coil (Rapid Biomedical, Rimpar, Germany) and a 20 mm diameter ^{13}C receiver coil (Rapid Biomedical) placed under the cervical tumours. To facilitate co-registration between PET and MR images, the receiver coil and hindquarters of the mice were fixed to the mouse bed using R&S Turboflex (CFPM, Aulnay-sous-Bois, France). For anatomical reference, eight axial T_2-weighted ^{1}H images were acquired using a fast-spin echo sequence with a slice thickness of 2.5 mm, FOV 40 × 40 mm, and matrix size of 256 × 256 points. ^{13}C images were generated using a SpSp pulse sequence and 3D DSE acquisition (Figure 5.1)[149]. Flip angles were 7º for [1-^{13}C]pyruvate and 45º for [1-^{13}C]lactate, respectively, FOV was 40 × 40 × 20 mm with a nominal spatial resolution of 1.25 × 1.25 × 2.5 mm in the x, y and z planes, respectively. Five [1-^{13}C]pyruvate images were acquired prior to the first [1-^{13}C]lactate image after which each metabolite was excited at a temporal resolution of 2 s per metabolite (Figure 5.1c). The eighth pair of acquisitions was used as a reference scan where the z-gradients were turned off except for the slice selection gradient and the spoiler. At 1 h after injection of [^{18}F]FDG hyperpolarised [1-^{13}C]pyruvate (15 mL/kg) was infused intravenously over 8 s and the pulse sequence was started 2 s after the start of the infusion. Five [1-^{13}C]pyruvate images were acquired prior to the first [1-^{13}C]lactate image in order to minimise off-resonance effects and maximise SNR

(Figure 5.1). Images were acquired over 90 s and analysed in MATLAB (Mathworks, MA, USA). A 3D ROI over the tumour was defined on the T_2-weighted image. The [1-^{13}C]lactate/[1-^{13}C]pyruvate signal ratio was calculated from the area under the curve of their respective time courses.

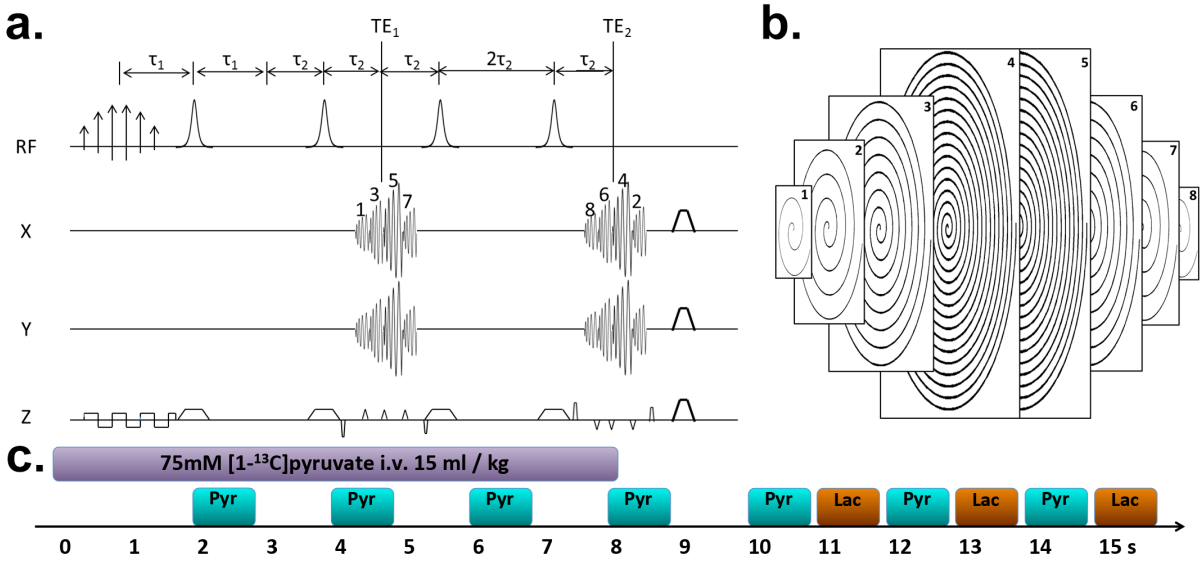

Figure 5.1. (a) 3D ^{13}C imaging pulse sequence, (b) its k-space trajectory and (c) the experiment timeline. Hyperpolarised [1-^{13}C]pyruvate is injected between 0 – 8 s with [1-^{13}C]pyruvate image acquisition every 2 s for the first 8 s followed by alternate [1-^{13}C]pyruvate and [1-^{13}C]lactate image acquisitions every second.

After completion of MRI the bed with mouse *in situ* was transferred to a nanoScan PET/CT (Mediso, Budapest, Hungary). A 15 min static PET acquisition began at 90 min post-injection of [^{18}F]DG. Static PET images, with a nominal isotropic resolution of 0.3 mm, were reconstructed using a 3D ordered-subset expectation maximisation method with a one to three coincidence mode, eight iterations and six subsets. Images were normalised and corrected for decay, dead-time, random events and attenuation. For anatomical reference and attenuation correction a whole-body helical CT was acquired with 360 projections, 55 kVp x-ray energy, 600 ms exposure

time and 0.21 mm isotropic voxels. The images were analysed using Vivoquant 3.0 software (InviCRO, Massachusetts, USA). A 3D region of interest was drawn manually over the subcutaneous tumour and Otsu thresholding applied to delineate the tumour. For semi-quantitative analysis, mean and maximum standardised uptake values were calculated using:

$$SUV = \frac{c_{img}}{ID/BW}$$

where c_{img} is the activity concentration (MBq/mL) derived from the image ROI, ID is the injected dose (MBq) and BW is the body weight (g) of the animal.

5.2.5. Whole-body [^{18}F]FDG autoradiography

Eμ-*Myc* mice (n = 6 untreated and n = 4 treated) were anaesthetised and injected intravenously with [^{18}F]FDG and then awakened. At 80 min post-injection mice were re-anaesthetised and sacrificed by intravenous injection of pentobarbital and immediately frozen by submersion in a bath of isopentane surrounded by an outer liquid nitrogen bath. Ten μm-thick axial cryo-sections (CM3050S Cryostat, Leica) taken through the cervical tumour region were thaw-mounted onto microscope slides. Slides were placed adjacent to a storage phosphor screen (GE, Chicago, IL, USA) overnight and the screen imaged with a pixel size of 10 μm (Typhoon Biomolecular Imager, Amersham Biosciences, Little Chalfont, UK). The slides were H&E stained and autoradiography and H&E images were co-registered manually. Tissue-to-muscle [^{18}F]FDG uptake ratios were calculated using Fiji for ImageJ[230].

5.3. Results

5.3.1. Hyperpolarised [1-^{13}C]pyruvate MRS and [^{18}F]FDG-PET in separate cohorts of mice

Eμ-*Myc* mice (n = 6) were imaged before and 24 h after treatment with cyclophosphamide (Figure 5.2). There was a decrease in the apparent k_{PL} from 0.12 ± 0.03 to 0.04 ± 0.03 after treatment (P = 0.002). In a separate cohort of Eμ-*Myc* mice (n = 4) [^{18}F]FDG-PET results were difficult to interpret. Tumour volume obviously decreased in all mice (n = 4) but, compared to the homogenous uptake in pre-treatment tumours (Figure 5.3c), post-treatment there were small areas of high uptake that could have been tumour tissue or spill-in from adjacent normal tissue (Figure 5.3 d & e). Whether the ROI included or excluded these areas significantly impacted post-treatment SUVs (Figure 5.3 a & b).

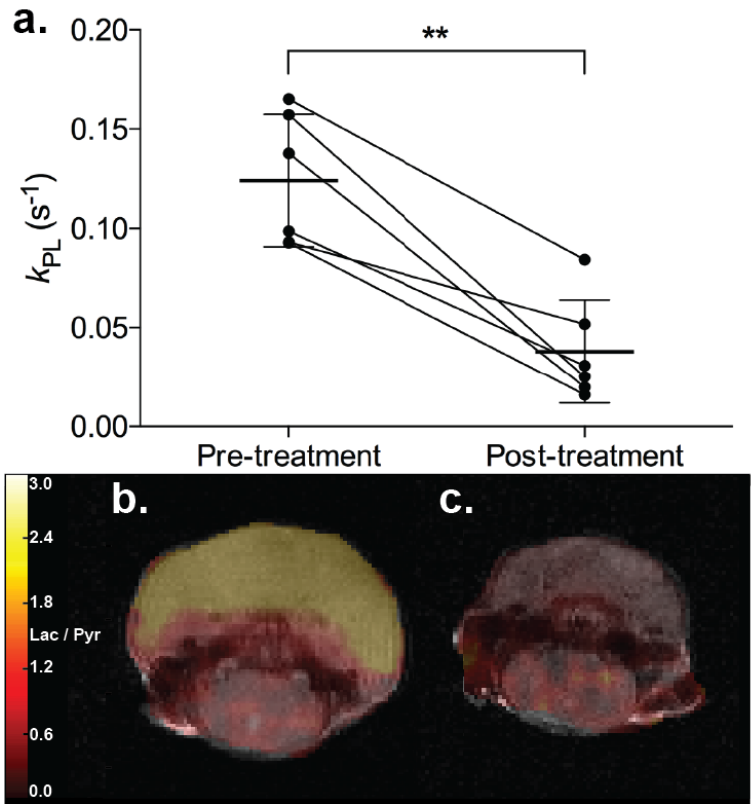

Figure 5.2. (a) Apparent k_{PL} in Eμ-*Myc* cervical tumours before and after treatment with cyclophosphamide. (b & c) Axial T_2-weighted slice of the same

tumour with overlays of [1-^{13}C]lactate/[1-^{13}C]pyruvate ratio chemical shift images acquired between 20 and 50 s after [1-^{13}C]pyruvate injection **(b)** before and **(c)** after treatment. The ^{13}C MRS measurements in **(a)** were performed by Tiago Rodrigues and Mikko Kettunen.

5.3.2. Whole-body [^{18}F]FDG autoradiography of Eμ-*Myc* mice

To determine whether the post-treatment [^{18}F]FDG avid regions were tumour or normal tissue, whole body autoradiography was performed on Eμ-*Myc* mice and the autoradiograms co-registered with the H&E stained section (Figure 5.4). In addition to lymph node tumours, the salivary glands were sometimes infiltrated with tumour cells. 24 h after treatment with cyclophosphamide there was a dramatic reduction in lymph node volume, with an expansion of normal glandular tissue. The tumour/muscle ratio decreased from 2.71 ± 0.4 to 1.84 ± 0.55 (n = 4; P = 0.02) after treatment. Treatment did not significantly change [^{18}F]FDG uptake in other tissues (2.21 ± 0.8 to 1.83 ± 0.5; n = 6; P = 0.07). The source of high [^{18}F]FDG uptake (visible in the centre of both autoradiograms in Figure 5.4 a & c) was inconsistent: in most mice it appeared to be small areas of muscle but in others it appeared to be glandular tissue (probably sublingual gland).

There were two key implications of the [^{18}F]FDG autoradiography: (1) [^{18}F]FDG uptake in lymph node tumours does decrease in response to cyclophosphamide and (2) the area of high uptake most frequently corresponded to muscle and was probably also responsible for the spill-in effects seen with the larger ROI in the [^{18}F]FDG-PET measurements acquired *in vivo*. Keeping mice anaesthetised throughout the uptake period is known to suppress muscle uptake and potentially these areas could be

excluded if tumours could be better delineated by improving the soft tissue contrast of anatomical imaging[187].

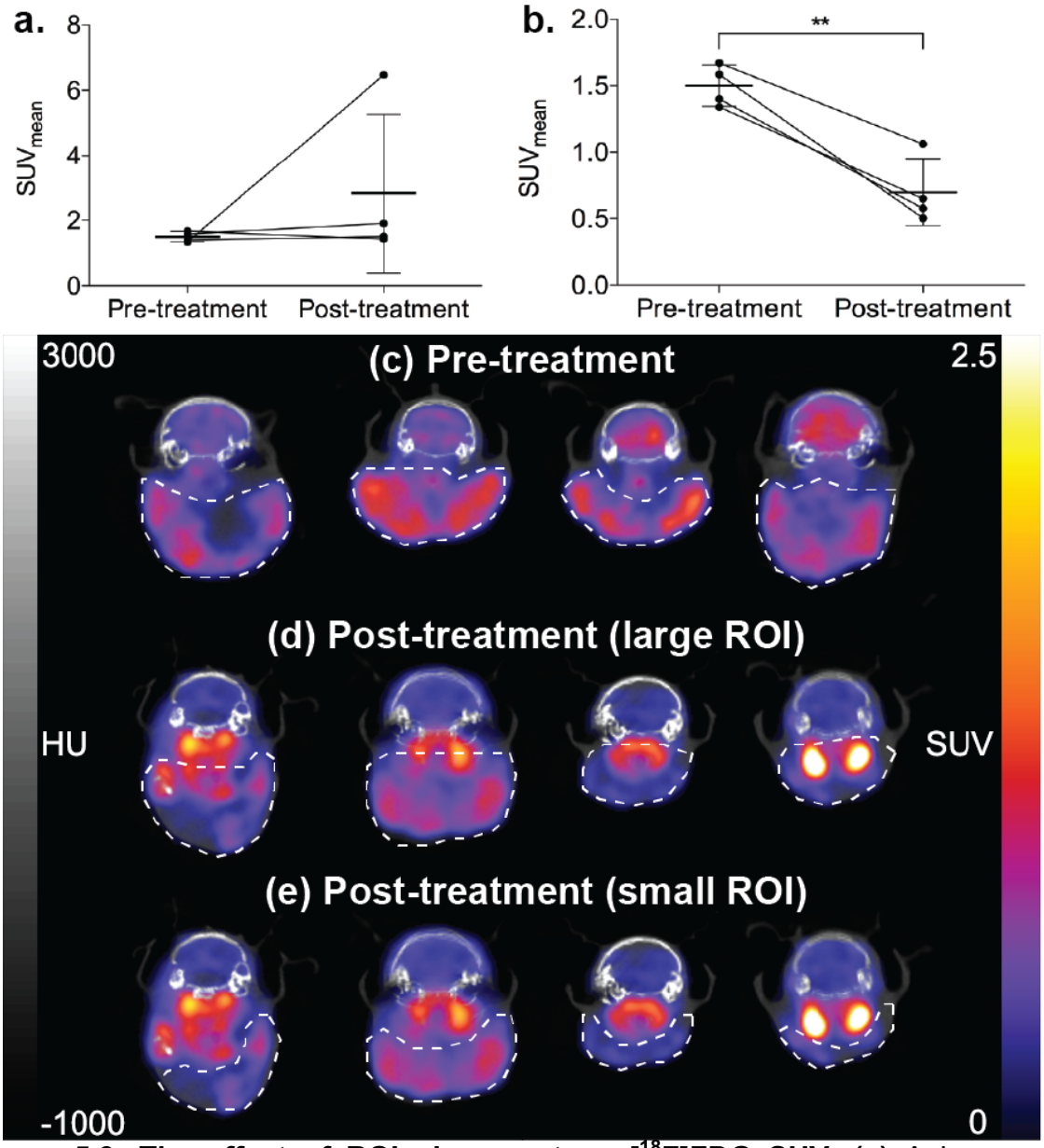

Figure 5.3. The effect of ROI placement on [^{18}F]FDG SUV. (a) A large post-treatment ROI resulted in significant spill in from surrounding tissues, masking the decrease in tumour SUV. **(b)** A small ROI that avoided any of the high uptake areas showed a decrease in tumour SUV after treatment. Images of the cervical tumours of four mice are shown **(c)** before treatment; **(d)** after treatment showing examples of large ROIs and **(e)** the same post-treatment images showing small ROIs.

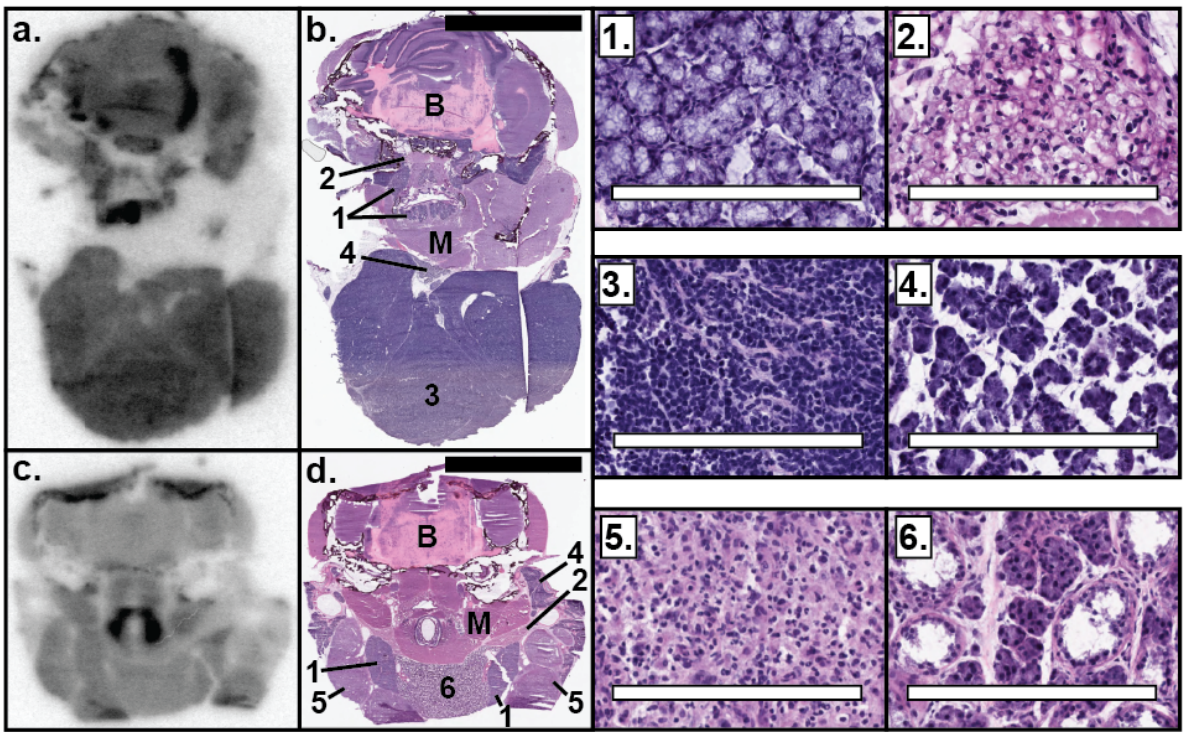

Figure 5.4. Eμ-*Myc* [^{18}F]FDG autoradiography and co-registered H&E stained sections (a & b) before and (c & d) after treatment. Tissues 1 – 6 are shown at higher scale in the insets. **(1)** Sublingual gland; **(2)** submaxillary gland; **(3)** lymph node tumour; **(4)** submandibular gland with tumour infiltration; **(5)** lymph node tumour 24 h after treatment; **(6)** submandibular gland 24 h after treatment; **(B)** brain, in the pre-treatment brain there was tumour cell infiltration as described previously[189]; **(M)** muscle. Black scale bars – 5 mm; white scale bars – 200 μm.

5.3.3. Combined hyperpolarised [1-^{13}C]pyruvate MRI and [^{18}F]FDG-PET of Eμ-*Myc* mice

Imaging with hyperpolarised [1-^{13}C]pyruvate and [^{18}F]FDG-PET was completed in eight mice, six of which were treated with cyclophosphamide 24 h before post-treatment imaging with two acting as controls. Cyclophosphamide treatment resulted in a decrease in tumour volume from 1.23 ± 0.6 to 0.52 ± 0.2 cm^3 (n = 6, P = 0.02). The tumour lactate/pyruvate ratio decreased from 2.09 ± 0.9 to 1.20 ± 0.4 (n = 4, P =

0.03) and [^{18}F]FDG SUV_{mean} decreased from 2.28 ± 0.4 to 1.28 ± 0.5 after treatment. Only in one animal did SUV_{mean} not decrease but this was the only animal (including autoradiography cohorts) where there was an increase in tumour size following treatment. Anaesthesia throughout the imaging procedure limited the uptake in surrounding tissues and spill-in was greatly reduced compared to the previous imaging protocol.

The tumours of control mice behaved very similarly to treated mice. The tumour volume decreased from 1.28 ± 0.3 to 0.50 ± 0.1, labelled lactate/pyruvate ratio decreased from 2.86 ± 0.01 to 1.01 ± 0.4 and SUV_{mean} decreased from 1.95 ± 0.1 to 1.14 ± 0.5.

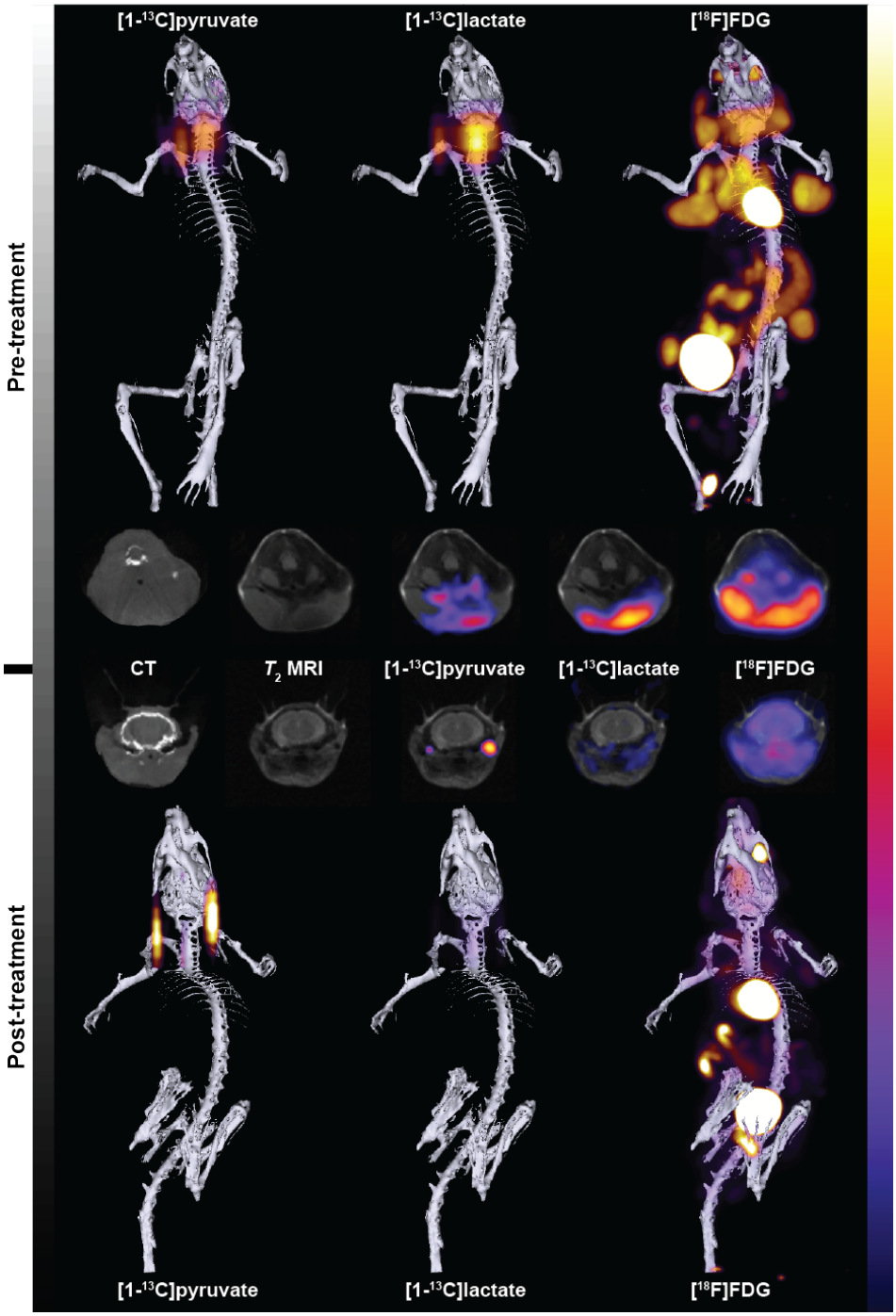

Figure 5.5. 3D reconstructions and axial slices through the cervical tumour of an Eμ-*Myc* mouse before (top) and after (bottom) cyclophosphamide treatment. Pre- and post-treatment images have the same scale, the CT is scaled from -1000 – 3000 HU, and the [^{18}F]FDG is scaled from an SUV of 0 – 2.5. The reduced background [^{18}F]FDG uptake as a result of optimal animal handling is notable in these images.

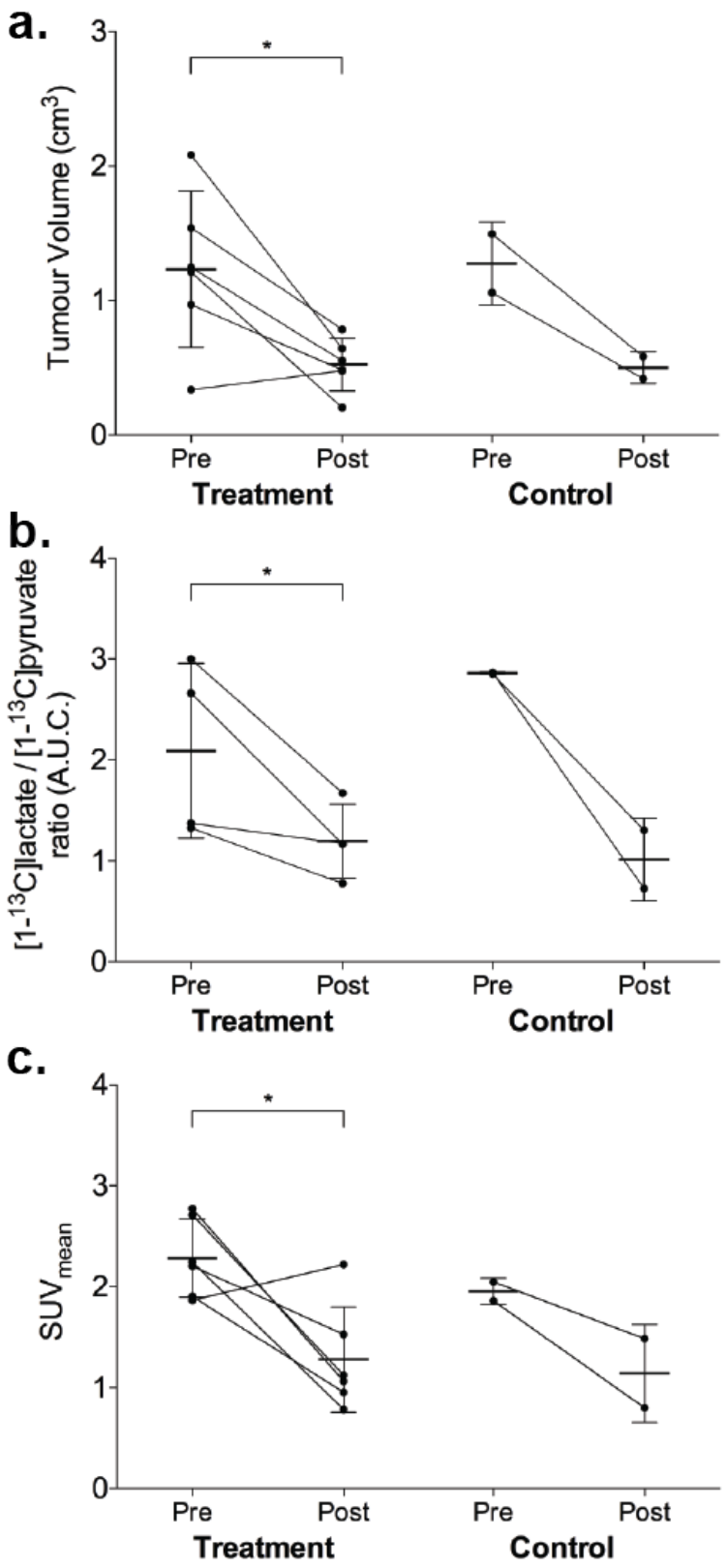

Figure 5.6. Changes in (a) tumour volume, (b) [1-^{13}C]lactate/[1-^{13}C]pyruvate ratio and (c) [^{18}F]FDG SUV_{mean} in treated and control Eμ-*Myc* mice.

5.3.4. T_2-weighted imaging of control mice

Eμ-*Myc* mice were anaesthetised for 90 min and T_2-weighted imaging of cervical tumours performed and repeated 48 h later. Tumour volume decreased by 63 ± 6% (n = 3) suggesting that the reduction in tumour volume seen in control mice was due to anaesthesia and animal handling, rather than as a result of CT irradiation or injection of [1-^{13}C]pyruvate or [^{18}F]FDG (Figure 5.7).

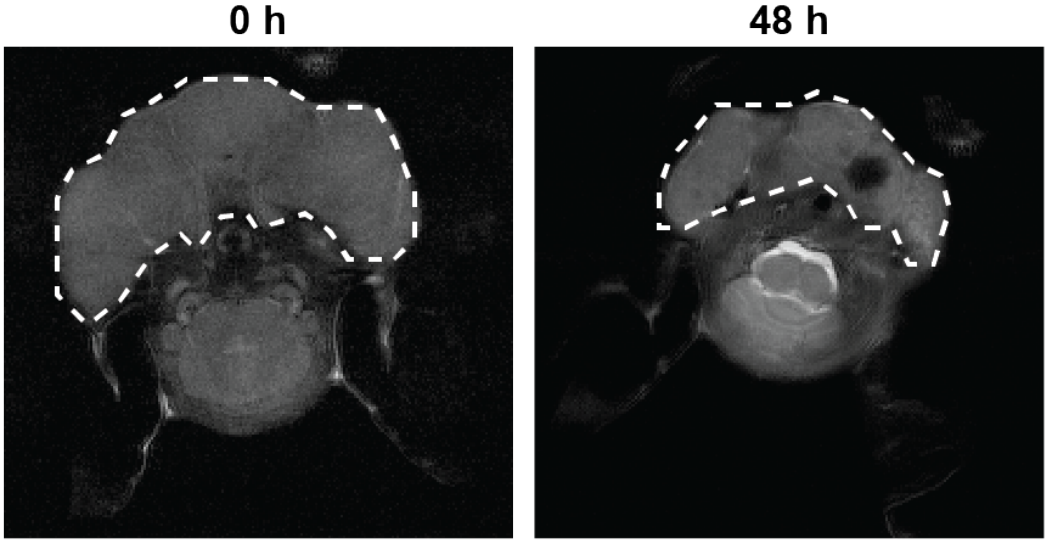

Figure 5.7. The cervical tumour of an Eμ-*Myc* mouse imaged before and 48 h later showing a significant decrease in the tumour volume without cyclophosphamide treatment.

5.4. Discussion

This study investigated the combined use of hyperpolarised [1-^{13}C]pyruvate and [^{18}F]FDG-PET for detecting the response of Eμ-*Myc* cervical tumours to cyclophosphamide. In separate cohorts of mice cyclophosphamide caused a 69% decrease in ^{13}C label exchange between pyruvate and lactate after 24 h. There was significant [^{18}F]FDG uptake in tissues surrounding the tumour and, as indicated in a previous case report, the conversion of labelled pyruvate to lactate appears to improve

tumour specificity compared to [^{18}F]FDG uptake[182]. This was presumably due to muscle having high rates of aerobic glycolysis but low rates of anaerobic lactate production and the lack of specificity that [^{18}F]FDG uptake has for detecting the Warburg effect. This is potentially advantageous clinically although differentiating tumour and muscle is rarely an issue and it remains to be seen whether hyperpolarised [1-^{13}C]pyruvate can differentiate tumours from inflammatory lesions which may also have increased rates of lactate production[231].

Whole body autoradiography showed that tumour [^{18}F]FDG uptake decreased after treatment whilst uptake in surrounding normal tissues was largely unchanged. Furthermore, some of the most [^{18}F]FDG avid tissues were areas of muscle and salivary gland. Due to the high morbidity of Eμ-*Myc* mice they were kept awake during the [^{18}F]FDG uptake period, resulting in higher levels of background uptake, particularly by muscle[187]. Therefore, combined imaging with hyperpolarised [1-^{13}C]pyruvate and [^{18}F]FDG was undertaken with mice anaesthetised throughout and, although this increased the mortality rate, a reduction in background [^{18}F]FDG uptake made images far easier to interpret. Similar distributions of [1-^{13}C]lactate production and [^{18}F]FDG uptake were seen in all tumours before treatment. Cyclophosphamide caused mean decreases of 43%, 44%, and 57% in the labelled lactate/pyruvate ratio, SUV_{mean} and tumour volume, respectively. In one animal tumour volume increased by 41%, SUV_{mean} increased by 19% and the labelled lactate/pyruvate ratio decreased by 15% after cyclophosphamide treatment. However, in mice where both the tumour volume and SUV_{mean} also decreased after treatment the labelled lactate/pyruvate ratio decreased by 54.2 ± 12%. Therefore, the slight decrease in the labelled lactate/pyruvate ratio in the non-responding animal is probably insignificant.

Unfortunately, the study was limited by the sensitivity of the model to the stress of animal handling and anaesthesia as decreases of 65%, 42% and 61% were seen in labelled lactate/pyruvate ratio, SUV_{mean} and tumour volume in untreated mice.

5.5 Conclusions

In this study hyperpolarised [1-^{13}C]pyruvate, [^{18}F]FDG and tumour volume all showed responses to treatment in Eμ-*Myc* mice, although the response was not necessarily due to the cyclophosphamide treatment. Although anaesthetising animals throughout the [^{18}F]FDG uptake period minimised background uptake, this study highlights the potential of measuring [1-^{13}C]pyruvate to [1-^{13}C]lactate flux as a more specific measure of the Warburg effect than [^{18}F]FDG-PET.

6. Hyperpolarised [1-^{13}C]pyruvate and [^{18}F]FDG imaging for detecting cell death induced by a TRAIL agonist in MDA-MB231 and Colo205 tumours

6.1. Introduction

The preceding two chapters comparing hyperpolarised [1-^{13}C]pyruvate and [^{18}F]FDG for detecting treatment response in two mouse tumour models came to differing conclusions. In murine EL4 tumours there was a reduction in [^{18}F]FDG uptake but hyperpolarised [1-^{13}C]pyruvate did not detect a response. However, there were variable levels of cell death before and after treatment that limited the study. In Eμ-*Myc* mice both agents detected a response in tumours but control conditions also invoked a tumour response. In the work described in this chapter human colorectal (Colo205) and breast (MDA-MB-231) adenocarcinoma xenografts were treated with MEDI3039, a multivalent TRAIL agonist that activates the extrinsic pathway of apoptosis by targeting death receptor 5 (DR5). Although subcutaneous tumours in athymic Balb/c nude mice have clear limitations as models of human disease, they have the advantages of relatively rapid tumour growth (approximately 6 – 10 weeks), minimal pre-treatment cell death and rapid, extensive apoptosis following MEDI3039 treatment. Furthermore, both cell lines were engineered to express luciferase and mStrawberry fluorescent protein to provide independent measures of treatment response.

Combined hyperpolarised [1-^{13}C]pyruvate and [^{18}F]FDG-PET imaging was performed to detect the early response of Colo205 and MDA-MB-231 tumours 24 h after treatment with MEDI3039, which induced long-term tumour remission[232]. There was a reduction in label flux between hyperpolarised [1-^{13}C]pyruvate and [1-^{13}C]lactate in all animals after treatment. This was accompanied by a decrease in bioluminescence but preceded by a reduction in tumour volume. In the same cohort [^{18}F]FDG-PET largely failed to detect response. Using a novel fluorescence activated cell sorting (FACS) technique we determined that this failure was not due to immune

cell infiltration or activation. We demonstrated that glucose and [^{18}F]FDG continued to accumulate and be phosphorylated in treated tumours but there was a decrease in further metabolism. These results indicate that in certain tumours hyperpolarised [1-^{13}C]pyruvate may be a more sensitive marker of response to treatment than [^{18}F]FDG.

6.2. Methods

The following methods described in "Chapter 2 - Methods" are used in this chapter:

2.1. Animal licence statement

2.3. Colo205 cell culture, tumour growth and treatment

2.4. MDA-MB-231 cell culture, tumour growth and treatment

2.6. Anaesthesia of mice

2.7. Hyperpolarisation of [1-^{13}C]pyruvate

2.8. Western blotting

2.9. Lactate dehydrogenase (LDH) activity assay

2.10. Immunohistochemistry (IHC)

2.11. Statistical analysis

6.2.1. Animal preparation

Mice were fasted for 6 – 8 h and kept in a warmed chamber (31 ºC) for 1 h prior to anaesthesia before all procedures requiring intravenous injection or imaging[187, 233].

6.2.2. Detection of long-term treatment response

Colo205 tumour-bearing mice (n = 3) were treated with MEDI3039 i.v. weekly for four weeks and fortnightly thereafter. Response was monitored by [^{18}F]FDG-PET

(for 72 h), T_2-weighted MRI (for 12 days), fluorescence and bioluminescence imaging (for 176 days).

6.2.3. Imaging treatment response

Mice were warmed, anaesthetised and a tail vein cannula inserted as described previously. Venous glucose concentration was measured using a StatStrip Xpress glucose meter (Nova Biomedical, Waltham, MA, USA). Bioluminescence, fluorescence, MRI and PET-CT imaging were performed in the same 2 h session before and 24 h after treatment with MEDI3039. Fluorescence and bioluminescence imaging were performed using an IVIS Lumina In Vivo Imaging System (Perkin Elmer, MA, USA). Fluorescence images (FLI) of mStrawberry expression (wavelength of excitation (λ_{ex}) = 574 nm, wavelength of emission (λ_{em}) = 596 nm) were obtained using a DSRed filter (λ_{ex} = 500-550 nm, λ_{em} = 575-650 nm) and corrected for background autofluorescence. Bioluminescence images (BLI) were acquired 5 min after intraperitoneal injection of 150 mg/kg D-luciferin.

After completion of bioluminescence imaging, mice were injected intravenously with 12.9±1.8 MBq [^{18}F]FDG (Alliance Medical, Guildford, UK) before magnetic resonance imaging (MRI). MRI was performed in a 7.0 T horizontal bore magnet (Agilent, Palo Alto, CA) using an actively decoupled dual-tuned ^{13}C/^{1}H volume transmit coil (Rapid Biomedical, Rimpar, Germany) and a 20 mm diameter ^{13}C receiver coil (Rapid Biomedical) placed over the tumours. To facilitate co-registration between PET and MR images the receiver coil and hindquarters of the mice were fixed to the mouse bed using R&S Turboflex (CFPM, Aulnay-sous-Bois, France). For anatomical reference, eight axial T_2-weighted ^{1}H images were acquired using a fast-spin echo sequence with a slice thickness of 2.5 mm, field-of-view (FOV) 40 × 40 mm and matrix

size of 256 × 256 points. ^{13}C images were acquired using a SpSp pulse sequence and 3D DSE acquisition.[223] Flip angles were 7º for [1-^{13}C]pyruvate and 45º for [1-^{13}C]lactate, respectively, FOV was 40 × 40 × 20 mm with a nominal spatial resolution of 1.25 × 1.25 × 2.5 mm in the x, y and z planes, respectively. Five [1-^{13}C]pyruvate images were acquired prior to the first [1-^{13}C]lactate image, after which each metabolite was excited at a temporal resolution of 2 s per metabolite. At 1 h after injection of [^{18}F]DG, hyperpolarised [1-^{13}C]pyruvate (15 mL/kg) was infused intravenously over 8 s and the pulse sequence was started 2 s after the start of the infusion. Five [1-^{13}C]pyruvate images were acquired prior to the first [1-^{13}C]lactate image in order to minimise off-resonance effects and maximise SNR. Images were acquired over 90 s and analysed in MATLAB (Mathworks, MA, USA). A 3D region of interest (ROI) over the tumour was defined on the T_2-weighted image and the [1-^{13}C]lactate/ [1-^{13}C]pyruvate signal ratio was calculated from the area under the curve of their respective time courses.

After completion of MRI the bed with mouse *in situ* was transferred to a nanoScan PET/CT (Mediso, Budapest, Hungary). A 15 min static PET acquisition began at 90 min post-injection of [^{18}F]FDG. Static PET images, with a nominal isotropic resolution of 0.3 mm, were reconstructed using a 3D ordered-subset expectation maximisation method with one to three coincidence mode, eight iterations and six subsets. Images were normalised and corrected for decay, dead-time, random events and attenuation. For anatomical reference and attenuation correction a whole-body helical CT was acquired with 360 projections, 55 kVp x-ray energy, 600 ms exposure time and 0.21 mm isotropic voxels. The images were analysed using Vivoquant 3.0 software (InviCRO, Massachusetts, USA). A 3D region of interest was drawn manually

over the subcutaneous tumour and Otsu thresholding applied to delineate the tumour. For semi-quantitative analysis, mean and maximum SUVs were calculated using:

$$SUV = \frac{c_{img}}{ID/BW}$$

where c_{img} is the activity concentration (MBq/mL) derived from the image ROI, ID is the injected dose and BW is the body weight of the animal.

6.2.4. Dynamic contrast enhanced (DCE) MRI

A separate cohort of Colo205 tumour-bearing mice (n = 3) was used to acquire a DCE-MRI dataset, before and 24 h after treatment with MEDI3039. Baseline spin-lattice relaxation rates ($R_{1,pre} = 1/T_1$) were measured using an inversion recovery fast low angle shot (FLASH) pulse sequence (TR 5.5 ms, TE 2.5 ms, 10 s delay between acquisitions, 2 averages per inversion time). To obtain a pre-contrast R_1 map these data were fitted voxel-by-voxel to a mono-exponential function:

$$S = S_0[1 - 2\, e^{-T_I/T_1}]$$

where T_I is the inversion time. A T_1-weighted gradient-echo pulse sequence was used with 4 × 1.5 mm thick axial slices with 0.25 mm gaps covering the tumour region, FOV 40 × 40 mm, data matrix 128 × 128, TR 110 ms, TE 9 ms. Ten baseline images were collected prior to the injection, over 8 s, of 200 μmoles/kg i.v. Dotarem® (gadoterate meglumine; Guerbet, Villepinte, France). Forty images were acquired immediately after injection and a further nine blocks of nine images were acquired every ten minutes up to 90 min post-injection. Each block of nine images were averaged, creating the timepoints in Figure 6.5. Images were converted to R_1 relaxation rate maps using:

$$S = S_0 \frac{(1 - e^{-TR/T_1})\sin\theta}{1 - e^{-TR/T_1}\cos\theta}$$

where S_0 is the relaxed signal (TR >> T_1) and θ is the flip angle used in the gradient-echo sequence (27º). Changes in R_1 were directly converted to gadolinium (Gd^{3+}) concentration curves as described by Noebauer-Huhmann et al.[234]. The DCE calculations were performed by Alan Wright.

6.2.5. Dynamic [^{18}F]FDG-PET imaging

A separate cohort of Colo205 tumour-bearing mice (n = 9) was imaged before and 24 h after treatment with MEDI3039. Mice were imaged three at a time. A 3 h PET acquisition was started just prior to injection over 30 s of 8.12 ± 1.13 MBq [^{18}F]FDG into each tumour-bearing mouse. Data were acquired in list-mode format. A CT image was acquired for anatomic co-registration and attenuation correction. Scans were reconstructed with a nominal isotropic resolution of 0.6 mm using a 3D ordered-subset expectation maximisation method with one to five coincidence modes, two iterations and six subsets. Images were normalised and corrected for decay, dead-time, random events and attenuation. Three h scans were reconstructed into 50 time frames (5 s × 12, 0 – 1 min; 2 min × 30, 0 – 60 min; 15 min × 8, 60 – 180 min). An image-derived arterial input function was derived from a 3D ROI drawn manually over the aorta and inferior vena cava (which could not be differentiated from each other). To minimise spill-in effects the ROI was drawn between the level of the kidneys and diaphragm, where contributions from other organs are relatively low, and thresholded at 75% of the maximum in the 5 s time frames. A 3D ROI drawn manually over the tumour was Otsu thresholded on the 165 – 180 min dataset. Patlak graphical analysis was used to estimate the rate of irreversible [^{18}F]FDG uptake (k_i) from the linear portion of the graph between 20 and 60 min[209]. Across all datasets, the mean coefficient of determination (r^2) for linear regression fitting was 0.97 ± 0.03.

6.2.6. Whole-body [^{18}F]FDG autoradiography and mStrawberry fluorescence imaging

Colo205 tumour-bearing mice (n = 6) were anaesthetised and injected intravenously with [^{18}F]FDG, sacrificed by cervical dislocation at 90 min post-injection and immediately frozen by submersion in a bath of isopentane surrounded by an outer liquid nitrogen bath. Ten µm-thick axial cryo-sections (CM3050S Cryostat, Leica) were thaw-mounted onto microscope slides. Fluorescence images (Amersham™ Typhoon™ Biomolecular Imager) of mStrawberry distribution were acquired using a 532 nm laser and long-pass 550 nm filter with a pixel size of 10 µm. Slides were then placed adjacent to a storage phosphor screen (GE) overnight and imaged with a pixel size of 10 µm. The slides were subsequently H&E stained and the three images (red fluorescence, autoradiography and H&E images) were co-registered manually.

6.2.7. Determining the cellular fate of [^{18}F]FDG using fluorescence-activated cell sorting (FACS)

Colo205 tumour-bearing mice (n = 6) were anaesthetised and injected intravenously with 140 ± 4.9 MBq [^{18}F]FDG. At 90 min post-injection, the animals were sacrificed by cervical dislocation and the tumours removed, weighed and washed in PBS. Single cell suspensions were prepared by finely mincing the tumours and digesting them in 1 mg/mL collagenase I (Sigma-Aldrich, MO, USA) and 0.1 mg/mL DNase I (Roche, Penzburg, Germany) at 37 ºC for 45 min with trituration at 15 min intervals. The cells were washed in PBS / 2mM EDTA and labelled for flow cytometry by incubation with anti-CD45 (30-F11), anti-CD11b (M1/70) (Biolegend, CA, USA) and live/dead fixable viability dye e780 (eBioscience, ThermoFisher Scientific, MA, USA) at 4 ºC for 1 h. CD11b+ / CD45+ phagocytes, CD45- / mStrawberry+ tumour cells,

CD45- / mStrawberry- non-haematopoetic, non-tumour cells and e780+ dead cells were sorted on a BD Influx™ flow sorter (BD Biosciences, NJ, USA). Flow cytometric data were analysed using FlowJo V10.0 (FlowJo LLC, OR, USA). The activity (cpm) of each cell population was counted three times for five minutes on a well counter (Nuklear-Medizintechnik, Dresden, Germany) and converted to Bq using a calibration curve and the injected dose per cell calculated.

6.2.8. [1,6-$^{13}C_2$]glucose infusion and ^{13}C and ^{1}H NMR spectroscopy of tumour extracts

Colo205 tumour-bearing mice were anaesthetised and [1,6-$^{13}C_2$]glucose infusions were performed as described previously[235]. Mice were sacrificed by cervical dislocation and the tumours immediately freeze-clamped in liquid nitrogen-cooled tongs and blood obtained by cardiac puncture. Extracts were prepared by the addition of 5 µL/mg tissue 2 M perchloric acid (PCA) and homogenisation using a Precellys 24 homogeniser (Stretton Scientific, Stretton, UK). Extracts were pH corrected to 7.0 with 2 M KOH, lyophilised and dissolved in 99.9% deuterium oxide. Two µmoles trimethylsilylpropanoic acid (TMSP) were added to each sample as a chemical shift standard (0 p.p.m.). High-resolution ^{1}H and ^{1}H-decoupled ^{13}C NMR spectra were acquired at 294 K using a Bruker 600 MHz NMR spectrometer (Bruker, MA, USA) using a 5 mm probe. ^{13}C spectroscopy acquisition used a pulse-acquire sequence with 30º flip angle, 15000 transients, spectral width 36.8 kHz, acquisition time 1.8 s and a relaxation delay 1.2 s. ^{1}H spectroscopy used a pulse-acquire sequence with a 90º flip angle, 1024 transients, spectral width 10 kHz, acquisition time 3.3 s, relaxation delay 2 s. Data were phased and baseline-corrected and peak areas calculated using Topspin 4.0 (Bruker, MA, USA).

6.2.9. Analysis of [^{18}F]FDG and labelled metabolites in tumour extracts

Colo205 tumour-bearing mice were anaesthetised and injected, via a tail vein, with a bolus of 146.2 ± 7.8 MBq [^{18}F]FDG. After 90 min the mice were sacrificed by cervical dislocation and the tumours excised and immediately homogenised in ice-cold 4M PCA using a Precellys homogeniser (Stretton Scientific, Stretton, UK). The extracts were neutralised using 8M KOH and passed through an Anotop 10, 0.2 µm syringe filter (Whatman, Maidstone, UK). RadioHPLC was performed using a Dionex UltiMate 3000 HPLC system (ThermoFisher Scientific, MA, USA) using a method adapted from Rokka et al.[236]. 100 µL samples were injected into the system, separated using a Partasil SAX 10 µm column (250 mm × 4.6 mm, Sigma-Aldrich) and eluted with a linear gradient of 300 mM sodium dihydrogen phosphate containing 2% methanol (A) and 2% methanol in water (B). The gradient profile was 0 – 15 min 5% A, 15 – 25 min 50% A (isocratic), with a flow rate of 1.5 ml/min. Radioactivity was detected using a fLumo HPLC NaI detector (Berthold Technologies, Bad Wildbad, Germany) connected to the outflow of the column. Data were collected and analysed using Chromeleon v6.8 (ThermoFisher Scientific, MA, USA). Metabolites had the following retention times: 2 min, [^{18}F]FDG; 6 min, [^{18}F]FDG-6-*P*; 20 min, 2-([^{18}F]fluoro)-2-deoxy-6-phospho-D-gluconolactone [^{18}F]FD-PGL; and 22.5 min, 2-([^{18}F]fluoro)-2-deoxy-D-glucose-1,6-bisphosphate ([^{18}F]FDG-1,6-P_2).

6.2.10. ATP quantification assay

Tumour ATP concentration was quantified from freeze-clamped tumour samples using a colourimetric ATP Assay Kit (ab83355, Abcam, Cambridge, UK). Absorbance at 570 nm was measured using a PHERAstar FS microplate reader (BMG Labtech, Aylesbury, UK).

6.3. Results

6.3.1. MEDI3039 induces cell death and tumour regression

MEDI3039 treatment of Colo205 tumour-bearing mice (n = 3) resulted in a decrease in tumour volume from 0.95±0.1 cm^3 to 0.03±0.02 cm^3 12 days after initial treatment, after which volumes dropped to below the detection limit for T_2-weighted MRI (Figure 6.1 a – d). After treatment, bioluminescence and red fluorescence intensity decreased over the first month, after which one tumour started to regrow while the other two continued to decrease in intensity (Figure 6.1 e – n). Animals were culled at six months, at which point the tumour that regrew had reached its size limit and in the other two mice the tumours remained undetectable.

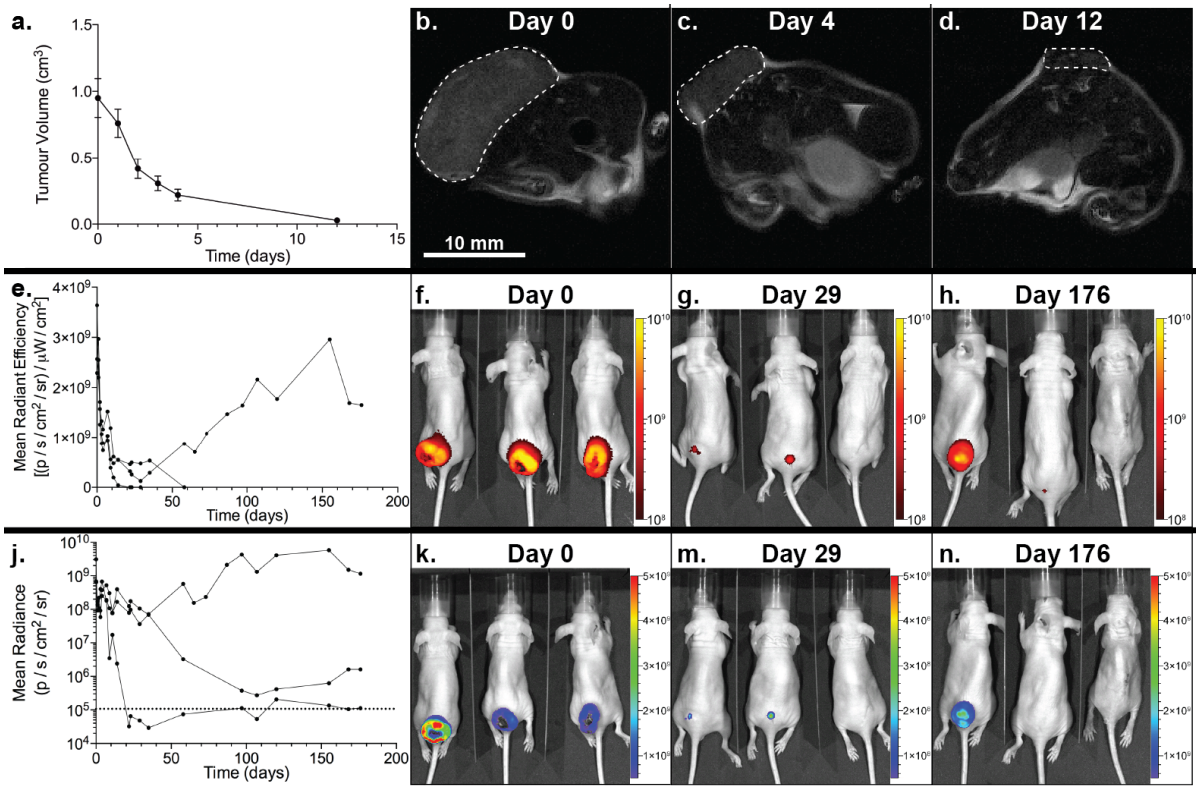

Figure 6.1. MEDI3039 treatment induces long-term remission of Colo205 tumours. (a-d) Tumour volumes (n=3) were determined by T_2-weighted MRI measurements. (e-h) mStrawberry fluorescence; (j-n) bioluminescence. The bioluminescence scale has been decreased by a factor of 10 for the images acquired on day 29.

6.3.2. Histological evaluation of cell death in tumours treated with MEDI3039

Colo205 (n = 18) and MDA-MB-231 (n = 22) tumour-bearing mice underwent combined BLI, FLI, [1-^{13}C]pyruvate MRI and FDG-PET imaging before and 24 h after treatment with either MEDI3039 or drug vehicle (Table 6.1). After treatment an insignificant increase in tumour volume was observed in controls for both tumour types while there was a slight, insignificant decrease in the volume of tumours treated with MEDI3039 (Figure 6.2). Treatment resulted in a significant increase in CC3 staining from 21.8 ± 11.6% to 58.51 ± 14.4% (P = 0.0002) in Colo205 tumours and 19 ± 5.1% to 57.7 ± 19.3% (P = 0.006) in MDA-MB-231 tumours. TUNEL staining increased from 8.0 ± 6.7% to 19.4 ± 6.3% (P = 0.007) in Colo205 tumours and 6.6 ± 2.0% to 21.1 ± 6.1% (P = 0.003) in MDA-MB-231 tumours (Figure 6.3).

	T_2 MRI	Bioluminescence	Fluorescence	^{13}C MRI
Tumour type	**Volume (cm^3)**	**Mean Radiance ($p/s/cm^2/sr$)**	**Mean Radiant Efficiency ($[p/s/cm^2/sr] / [\mu W/cm^2]$)**	**[1-^{13}C]lactate / [1-^{13}C]pyruvate ratio**
Colo205				
Pre-treatment	0.879 ± 0.425 (n = 10)	$2.455 \times 10^9 \pm 3.445 \times 10^9$ (n = 10)	$1.465 \times 10^9 \pm 9.009 \times 10^8$ (n = 8)	2.525 ± 0.549 (n = 7)
Post-treatment	0.829 ± 0.491 (n = 10)	$4.723 \times 10^8 \pm 5.678 \times 10^8$ ** (n = 10)	$2.068 \times 10^9 \pm 1.981 \times 10^9$ (n = 8)	1.414 ± 0.391 ** (n = 7)
Pre-control	0.705 ± 0.252 (n = 7)	$6.961 \times 10^8 \pm 9.705 \times 10^8$ (n = 8)	$1.373 \times 10^9 \pm 1.494 \times 10^9$ (n = 7)	1.975 ± 0.548 (n = 5)
Post-control	0.721 ± 0.289 (n = 7)	$1.092 \times 10^9 \pm 1.406 \times 10^9$ (n = 8)	$1.288 \times 10^9 \pm 1.191 \times 10^9$ (n = 7)	2.106 ± 0.630 (n = 5)
MDA-MB-231				
Pre-treatment	0.939 ± 0.488 (n = 8)	$1.288 \times 10^9 \pm 4.629 \times 10^8$ (n = 12)	$3.002 \times 10^9 \pm 1.180 \times 10^9$ (n = 12)	2.236 ± 0.386 (n = 7)
Post-treatment	0.862 ± 0.450 (n = 8)	$4.148 \times 10^8 \pm 4.340 \times 10^8$ **** (n = 12)	$1.634 \times 10^9 \pm 1.015 \times 10^9$ *** (n = 12)	1.382 ± 0.331 ** (n = 7)
Pre-control	0.664 ± 0.281 (n = 9)	$1.541 \times 10^9 \pm 1.503 \times 10^9$ (n = 9)	$2.349 \times 10^9 \pm 1.067 \times 10^9$ (n = 9)	2.126 ± 0.588 (n = 9)
Post-control	0.686 ± 0.304 (n = 9)	$1.067 \times 10^9 \pm 6.385 \times 10^8$ (n = 9)	$2.174 \times 10^9 \pm 1.110 \times 10^9$ (n = 9)	2.442 ± 0.607 (n = 9)

	[^{18}F]FDG-PET			Histology	
Tumour type	**SUV_{max}**	**SUV_{mean}**	**k_i**	**CC3 (% positivity)**	**TUNEL (% positivity)**
Colo205					
Pre-treatment	2.103 ± 0.250 (n = 7)	1.131 ± 0.160 (n = 7)	0.048 ± 0.01 (n = 9)		
Post-treatment	2.134 ± 0.362 (n = 7)	1.087 ± 0.190 (n = 7)	0.037 ± 0.012 (n = 9)	58.510 ± 14.440 *** (n = 7)	19.360 ± 6.311 ** (n = 7)
Pre-control	2.261 ± 0.580 (n = 7)	1.230 ± 0.223 (n = 7)			
Post-control	2.219 ± 0.161 (n = 7)	1.182 ± 0.206 (n = 7)		21.800 ± 11.580 (n = 7)	8.005 ± 6.728 (n = 7)
MDA-MB-231					
Pre-treatment	2.219 ± 0.399 (n = 10)	1.045 ± 0.172 (n = 10)			
Post-treatment	1.977 ± 0.346 (n = 10)	0.877 ± 0.158 * (n = 10)		57.650 ± 19.300 ** (n = 5)	21.120 ± 6.061 ** (n = 5)
Pre-control	2.125 ± 0.558 (n = 9)	0.998 ± 0.214 (n = 9)			
Post-control	2.039 ± 0.685 (n = 9)	0.913 ± 0.275 (n = 9)		18.980 ± 5.092 (n = 4)	6.644 ± 1.944 (n = 4)

Table 6.1. Multi-modality imaging and histological detection of treatment response 24 h after administration of 0.4 mg/kg MEDI3039. Levels of significance: *, $P \leq 0.05$; **, $P \leq 0.01$; ***, $P \leq 0.001$; ****, $P \leq 0.0001$.

mStrawberry fluorescence decreased in response to treatment in MDA-MB-231 tumours by 45.3 ± 28.6% (P = 0.0002) but there was no change in Colo205 tumours (P = 0.30). However, fluorescence in these tumours had started to decrease by 48 h after treatment (P = 0.04; n = 3). With the exception of one animal, bioluminescence decreased after treatment, with a 57.3 ± 53.3% (P = 0.0053; n = 10) and 68.5 ± 24.8% (P = <0.0001; n = 12) decrease in Colo205 and MDA-MB-231 tumours, respectively.

Corresponding to the decrease in bioluminescence signal, measurements of ATP concentrations in Colo205 tumour extracts showed a decrease from 0.36 ± 0.1 to 0.14 ± 0.05 µmol/g w.w. (*P* = 0.0008; n = 11) at 24 h after treatment.

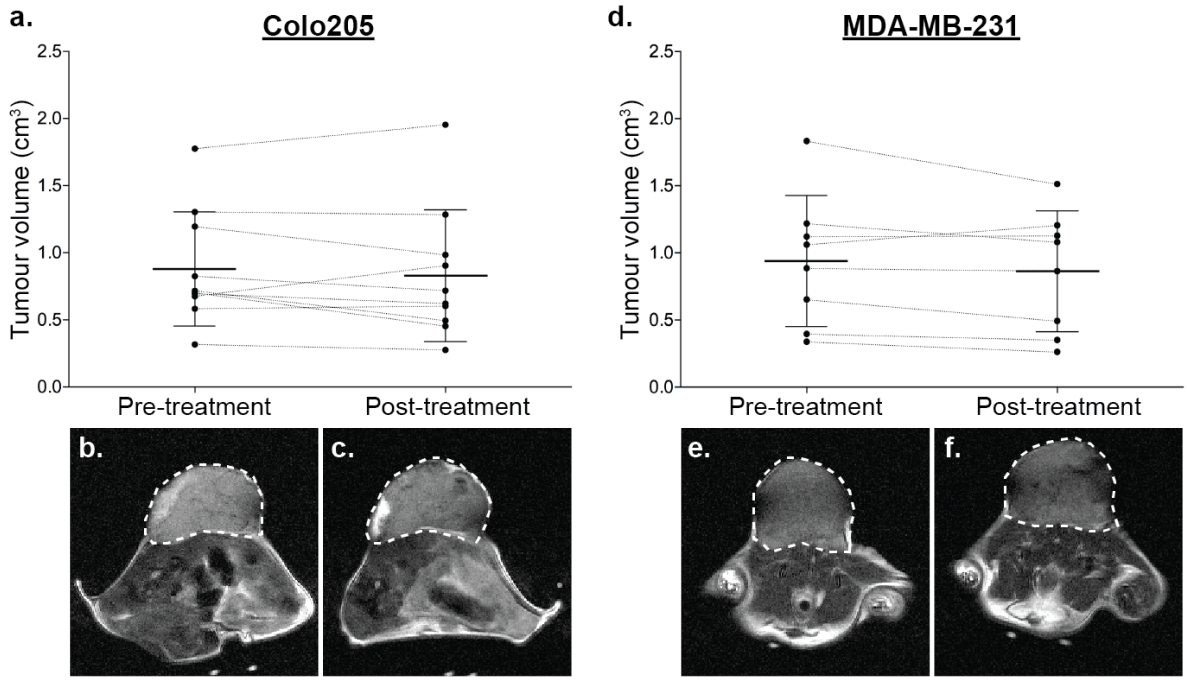

Figure 6.2. Tumour volume measurements of (a) Colo205 and (b) MDA-MB-231 tumours (b & e) before and (c & f) 24 h after MEDI3039 treatment.

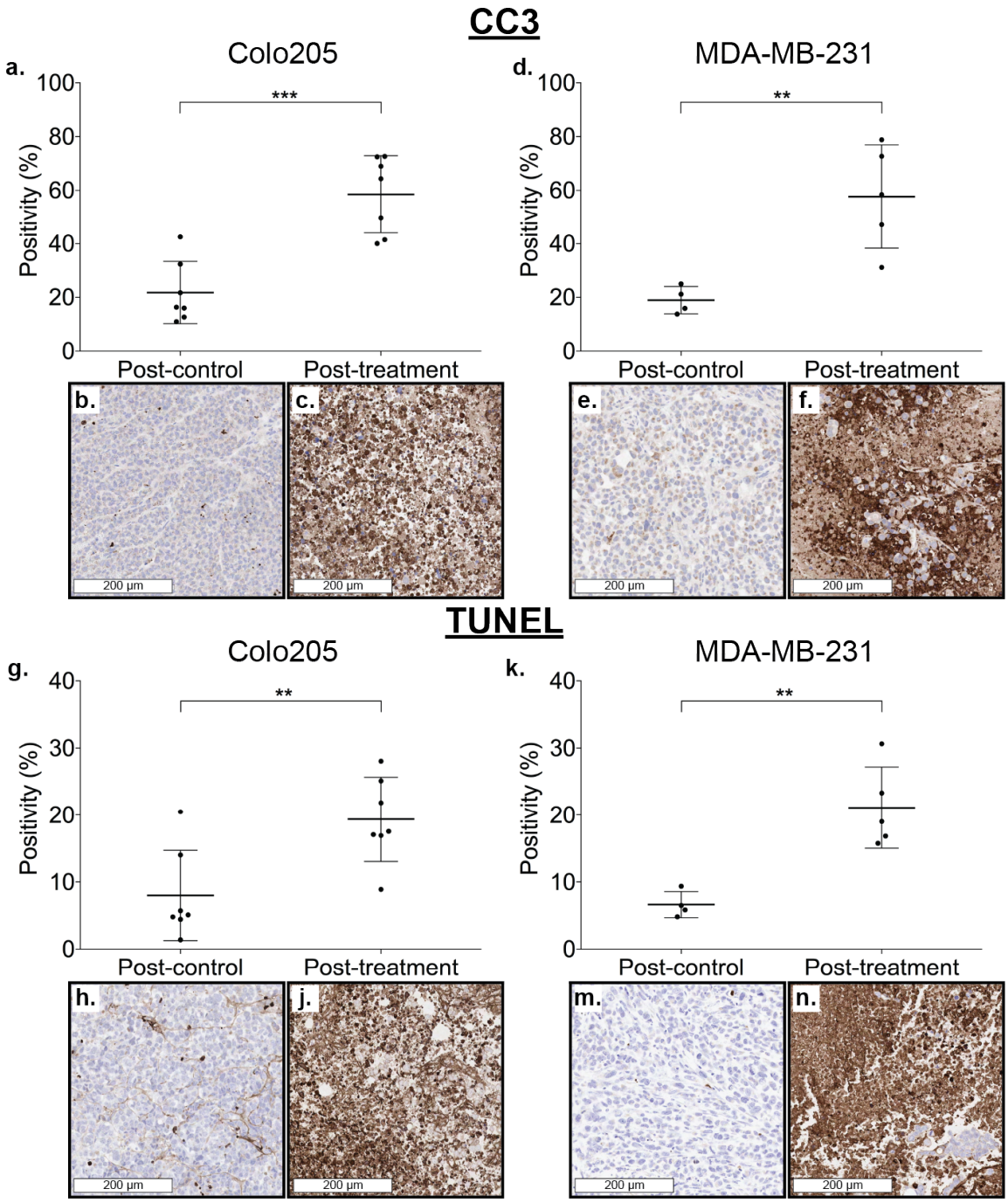

Figure 6.3. Histological assessment of tumour cell death following treatment with MEDI3039. Tumour sections were stained for cleaved caspase 3 (CC3) and TUNEL. (a – c) CC3 and (g – j) TUNEL staining of Colo205 tumour sections taken 24 h after treatment of the animals with MEDI3039 (treatment) or drug vehicle (control). (d – f) CC3 and (g – j) TUNEL staining of MDA-MB-231 tumour sections taken 24 h after treatment of the animals with MEDI3039 (treatment) or drug vehicle (control).

6.3.3. Imaging early response to MEDI3039 treatment using ^{13}C MRI and [^{18}F]FDG-PET

3D ^{13}C MR images, following injection of hyperpolarised [1-^{13}C]pyruvate, showed a post-treatment reduction of the [1-^{13}C]lactate/[1-^{13}C]pyruvate ratio in all animals, with a mean reduction of 42.2 ± 15.9% (P = 0.004; n = 7) and 36.3 ± 18.6% (P = 0.007; n = 7) in Colo205 and MDA-MB-231 tumours, respectively (Table 1 and Figure 6.4). However, with [^{18}F]FDG-PET there was no change in SUV_{max} (2.1 ± 0.3 to 2.1 ± 0.4, P = 0.82) or SUV_{mean} (1.1 ± 0.2 to 1.1 ± 0.2, P = 0.6) in Colo205 tumours after treatment. In a separate cohort of Colo205 tumours there was an insignificant decrease in influx rate constants for [^{18}F]FDG after treatment (0.05 ± 0.01 to 0.04 ± 0.01, P = 0.052). In MDA-MB-231 tumours SUV_{max} did not change significantly (2.2 ± 0.4 to 2.0 ± 0.3, P = 0.2) but there was a decrease in SUV_{mean} (1.0 ± 0.2 to 0.9 ± 0.2; P = 0.05) after treatment. However, this was a decrease of 14 ± 21%, compared to a 36 ± 19% decrease in [1-^{13}C]lactate/[1-^{13}C]pyruvate ratio in the same tumours, indicating that changes in [1-^{13}C]pyruvate metabolism were more sensitive for detecting response to treatment in these tumours.

To determine whether there were later changes in [^{18}F]FDG uptake, Colo205 tumour-bearing mice (n = 3) were imaged 24, 48 and 72 h following MEDI3039 treatment. Mean SUV_{max} increased insignificantly from 1.67 ± 0.1 before treatment to 1.79 ± 0.5 (P = 0.77) 72 h after treatment, despite significant decreases in tumour volume by this time.

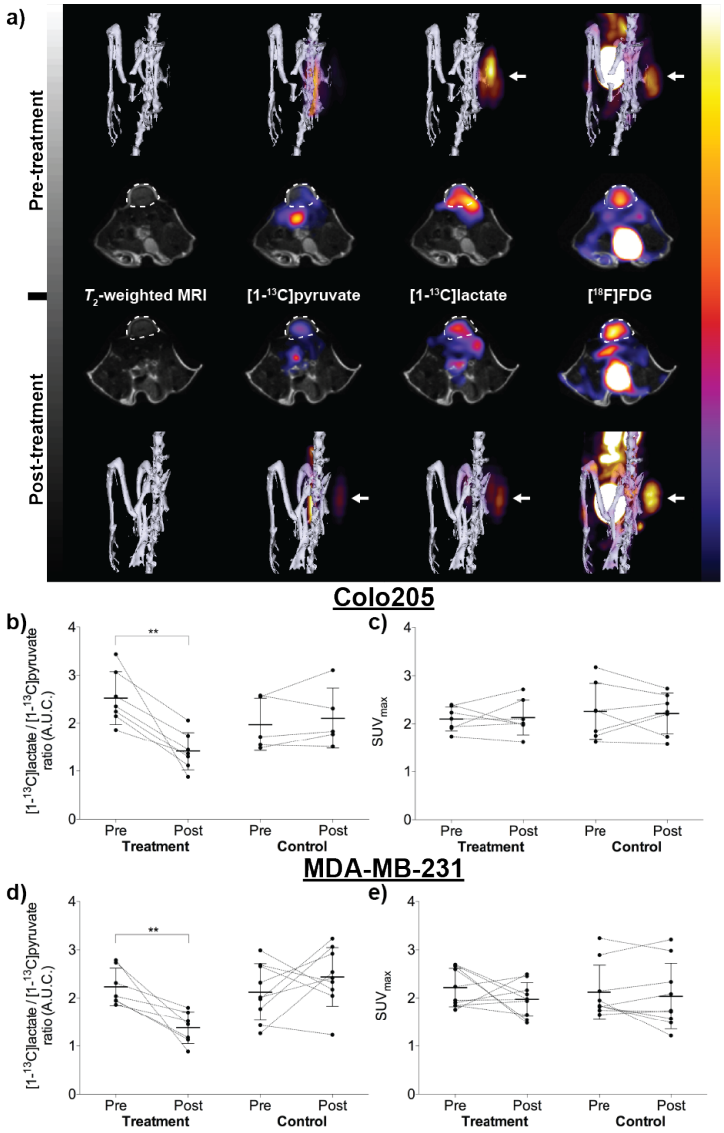

Figure 6.4. Comparison of hyperpolarised [1-^{13}C]lactate/[1-^{13}C]pyruvate ratio and [^{18}F]FDG-PET SUV_{max} in Colo205 and MDA-MB-231 tumours before and 24 h after treatment with MEDI3039. (a) A Colo205 tumour-bearing mouse before (top two rows of images) and after treatment (bottom two rows of images). 3D metabolite images overlaid on bone reconstructions (top and bottom rows) and an axial slice through the tumour (middle two rows). The tumour is indicated by white arrows and a dashed outline. **(b & d)** [1-^{13}C]lactate/[1-^{13}C]pyruvate ratio before and after treatment in **(b)** Colo205 and **(d)** MDA-MB-231 tumours. **(c & e)** [^{18}F]FDG SUV_{max} before and after treatment in **(c)** Colo205 and **(e)** MDA-MB-231 tumours.

6.3.4. DCE-MRI shows an increase in Colo205 tumour perfusion after MEDI3039 treatment

In a separate cohort of Colo205 tumour-bearing mice (n = 3) treatment response was assessed using DCE-MRI measurements (Figure 6.5). Tumour gadolinium (Gd^{3+}) concentration increased in all mice after treatment from 0.05 ± 0.009 to 0.09 ± 0.02 mM at 10 min post-injection although, due to the low cohort size, this was not statistically significant. The rate of contrast agent clearance was similar in pre-treatment and post-treatment tumours.

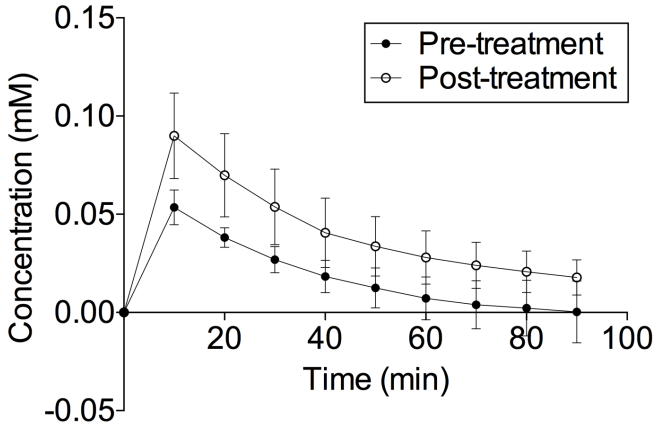

Figure 6.5. Dynamic contrast enhanced MRI in Colo205 tumours before and 24 h after treatment with MEDI3039.

6.3.5. Autoradiography of [^{18}F]FDG uptake in Colo205 tumours

To confirm the *in vivo* [^{18}F]FDG-PET measurements, whole-body autoradiography of Colo205 tumour-bearing mice (n = 3, treated and untreated) was performed. [^{18}F]FDG tumour/muscle ratios were unchanged after treatment (4.1 ± 0.8 before treatment and 4.1 ± 0.6 after treatment, P = 0.9) (Figure 6.6). Measurements of [^{18}F]FDG radioactivity in excised Colo205 tumours revealed a non-significant decrease of mean % injected dose per gram (%ID/g) from 8.8 ± 2.0 to 7.6 ± 1.7 after treatment (n = 3 treated and untreated, P = 0.3).

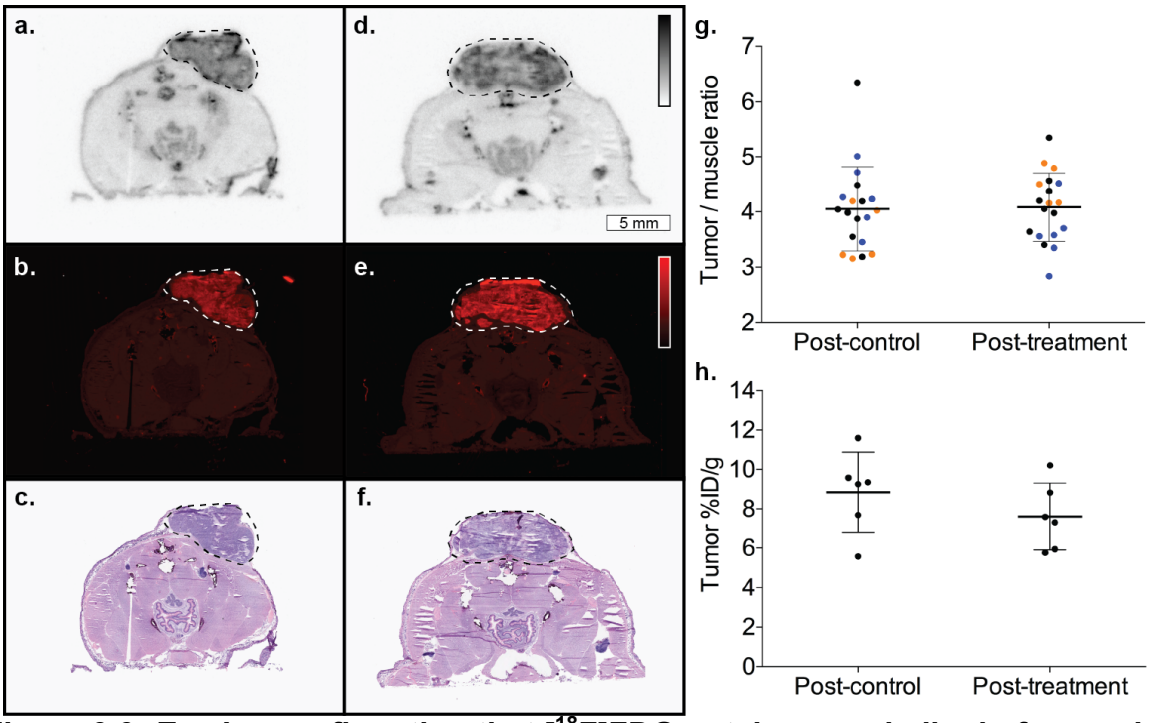

Figure 6.6. *Ex vivo* confirmation that [^{18}F]FDG uptake was similar before and 24 h after treatment. Examples of whole-body autoradiography sections of Colo205 tumour-bearing mice 24 h before **(a – c)** and after MEDI3039 treatment **(d – f). (a & d)** whole-body [^{18}F]FDG autoradiography; **(b & e)** mStrawberry fluorescence and **(c – f)** H&E staining of the same sections. **(g)** Tumour to muscle ratios derived from autoradiography (n = 3, colours indicate biological replicates, points indicate technical replicates from different sections); **(h)** uptake of [^{18}F]FDG measured in excised tumours. Abbreviations: ID – injected dose.

6.3.6. Determining the cellular fate of [^{18}F]FDG using FACS

Before treatment (n = 3) tumour cells (mStrawberry+, CD45-) comprised 78.3 ± 5.2% of the cells sorted by flow cytometry, a figure that dropped to 71.6 ± 9.4% (n = 3, *P* = 0.3) in tumours 24 h after treatment with MEDI3039 (Figure 5.7). In contrast, phagocytes (CD45+, CD11b+) comprised just 1.6 ± 0.4% of cells prior to treatment and 2.3 ± 1.7% (*P* = 0.5) after treatment (Figure 6.7). Treatment resulted in a slight

decrease in [^{18}F]FDG uptake (%ID/cell) in tumour cells from $2.1 \times 10^{-9} \pm 5.0 \times 10^{-10}$% to $7.5 \times 10^{-10} \pm 2.7 \times 10^{-10}$% ($P = 0.01$). Phagocytes were by far the most [^{18}F]FDG avid cell-type, taking up $1.2 \times 10^{-8} \pm 2.5 \times 10^{-9}$% per cell before treatment, which was approximately 5× tumour cell uptake. As in tumour cells after treatment, the activity per phagocyte also decreased to $6.5 \times 10^{-9} \pm 1.9 \times 10^{-9}$ ($P = 0.04$) and was approximately 8× the uptake of tumour cells. However, due to there being approximately 50× and 30× more tumour cells than phagocytes before and after treatment, respectively, despite their greater [^{18}F]FDG uptake per cell, the contribution of phagocytes to [^{18}F]FDG uptake in the tumour as a whole remained small. Correction for % cell type, represented as %ID per million total cells, showed that before treatment uptake in the tumour cell population was $2 \times 10^{-3} \pm 5 \times 10^{-4}$% per million cells, whereas in phagocytes it was $2 \times 10^{-4} \pm 8.7 \times 10^{-5}$% per million cells. After treatment uptake in the tumour cell population was $6 \times 10^{-4} \pm 5.5 \times 10^{-4}$%, whereas in the phagocyte population it was $1 \times 10^{-4} \pm 5.6 \times 10^{-5}$%.

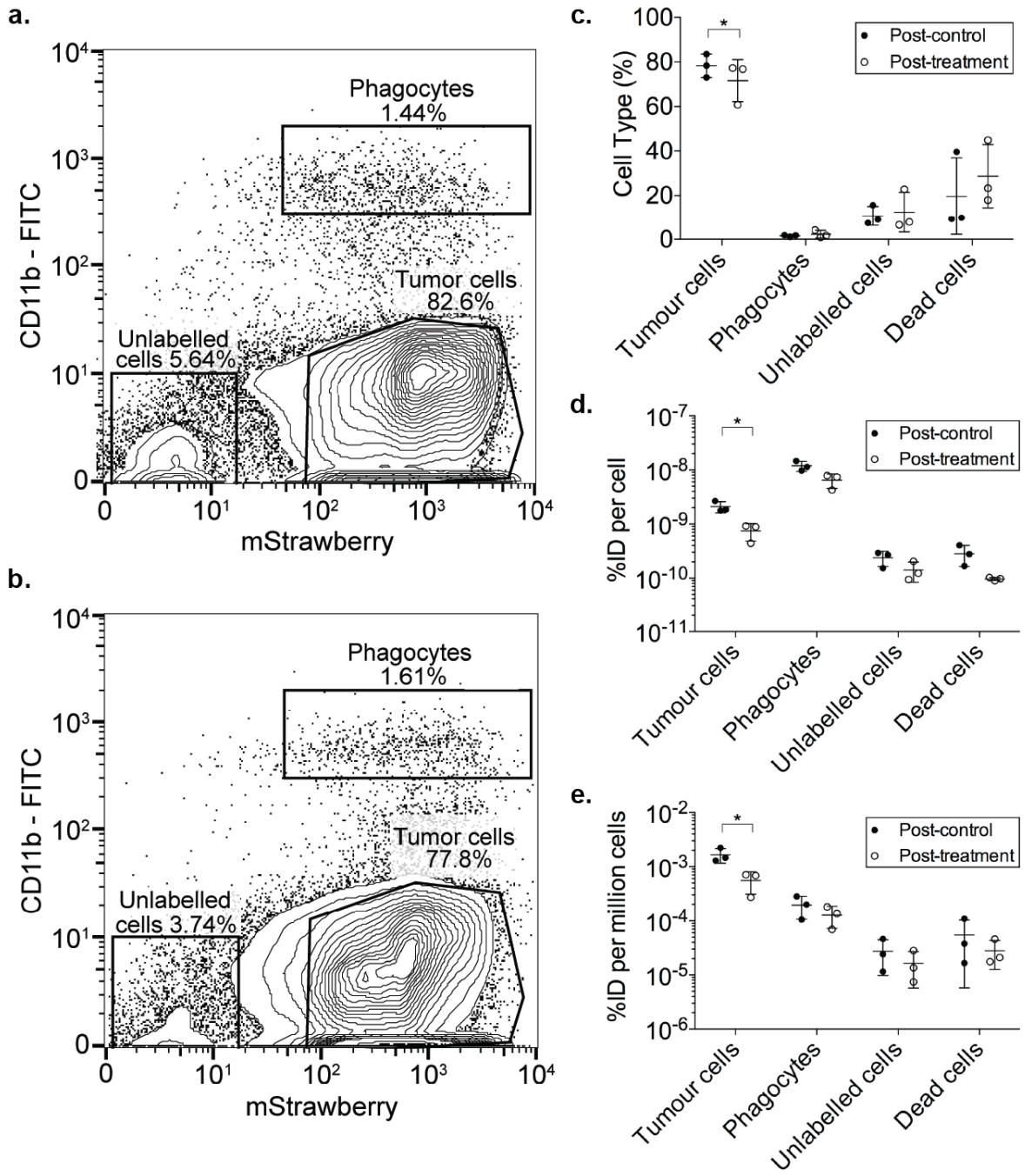

Figure 6.7. FACS sorting of *ex vivo* Colo205 tumours and determination of the cellular fate of [^{18}F]FDG. Examples of sort profiles of tumours 24 h after treatment with (**a)** drug vehicle and **(b)** MEDI3039; **(c)** the percentage of different cell types sorted; **(d)** the percentage injected dose per cell for each cell type and **(e)** the percentage injected dose for each population of cells (i.e. the %ID per cell corrected for the percentage of each cell type) displayed as %ID per million sorted cells.

6.3.7. Measurement of glycolytic flux in MEDI3039-treated Colo205 tumours using [1,6 $^{13}C_2$]glucose infusions

To investigate the effect of treatment on glycolytic flux [1,6 $^{13}C_2$]glucose was infused into mice (n = 3, treated and untreated). At the end of each 150 min infusion of [1,6 $^{13}C_2$]glucose ^{13}C enrichment of blood glucose was 50.0 ± 7.2%. There was no difference in the enrichment between treated and untreated animals. The concentration of [3-^{13}C]lactate, measured in extracts of Colo205 tumours, decreased from 1259 ± 297 μmoles/g w.w. before treatment to 363 ± 148 μmoles/g w.w. after treatment (P = 0.01, Figure 6.8). Treatment also resulted in a decrease in [3-^{13}C]alanine and [4-^{13}C]glutamate labelling. There was a much smaller and non-significant decrease in [1,6 $^{13}C_2$]glucose concentration in the tumours, from 425 ± 169 to 279 ± 135 μmoles/g w.w. (P = 0.3).

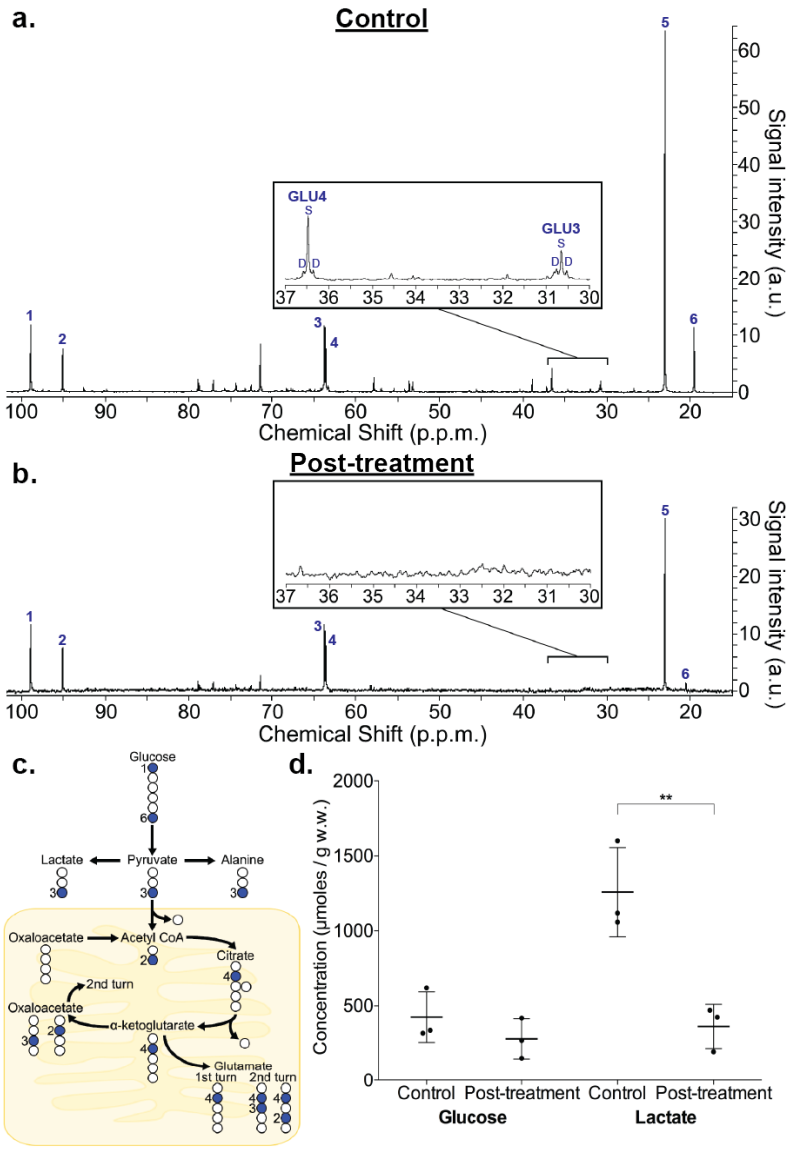

Figure 6.8. ^{13}C NMR measurements of Colo205 tumour extracts following [1,6 $^{13}C_2$]glucose infusions into tumour-bearing mice 24 h after drug vehicle or MEDI3039 treatment. Example ^{13}C NMR spectra from **(a)** a control tumour and **(b)** a treated tumour**.** Chemical shift assignments: 1, β-glucose C1; 2, α-glucose C1; 3, β-glucose C6; 4, α-glucose C6; 5, lactate C3; 6, alanine C3. Insets: the spectra zoomed between 30 and 37 p.p.m. to show the difference in C3 and C4 glutamate labelling before treatment and after treatment. **(c)** Diagram showing the ^{13}C labelling pattern (blue) following [1,6 $^{13}C_2$]glucose infusions. **(d)** Comparison of ^{13}C labelled glucose and lactate concentrations in control and MEDI3039 treated tumours.

6.3.8. MEDI3039 induced changes in the expression of glycolytic enzymes and membrane transporters in Colo205 tumours

Tumour protein expression of the enzymes and transporters involved in [^{18}F]FDG uptake and [1-^{13}C]pyruvate uptake and metabolism to [1-^{13}C]lactate were investigated by western blotting (Table 6.2, Figure 6.9). Treatment resulted in decreased expression of both monocarboxylate transporters, MCT1 and to a lesser extent MCT4 (P = 0.005 and P = 0.02, respectively). LDH activity and expression were unchanged, (P = 0.07 and P = 0.9, respectively) (Table 6.3). Expression of GLUT1 and GLUT3 also decreased (P = 0.01 and P = 0.0001, respectively), while HK2 expression was unchanged (P = 0.1). PARP cleavage by caspase-3, a feature of apoptosis and previously correlated with NADH depletion and subsequent reduction in pyruvate to lactate exchange *in vitro*, increased significantly after MEDI3039 treatment (P = 0.005)[69, 107].

Treatment	MCT1	MCT4	GLUT1	GLUT3	LDH	HK-2	cPARP
Control (n = 7)	0.070 ± 0.01	0.47 ± 0.04	0.028 ± 0.007	0.0047 ± 0.002	0.35 ± 0.04	0.018 ± 0.007	0.0019 ± 0.0008
Post-treatment (n = 7)	0.013 ± 0.009 **	0.32 ± 0.04 *	0.0079 ± 0.002 *	0.0002 ± 0.0009 ***	0.30 ± 0.06	0.012 ± 0.06	0.012 ± 0.008 **

Table 6.2. Protein expression of the transporters and enzymes involved in [^{18}F]FDG and [1-^{13}C]pyruvate uptake and metabolism in Colo205 tumours. Numbers are level of expression relative to: GAPDH for MCT1; β-tubulin for MCT4 and β-actin for all others.

Treatment	LDH activity	GAPDH activity	PK activity
Control (n = 7)	2.1 ± 0.3	0.16 ± 0.1	2.4 ± 1.6
Post-treatment (n = 7)	2.1 ± 0.4	0.13 ± 0.1	3.3 ± 1.8

Table 6.3. Enzyme activities in Colo205 tumours. All enzyme activities are expressed in units/mg protein.

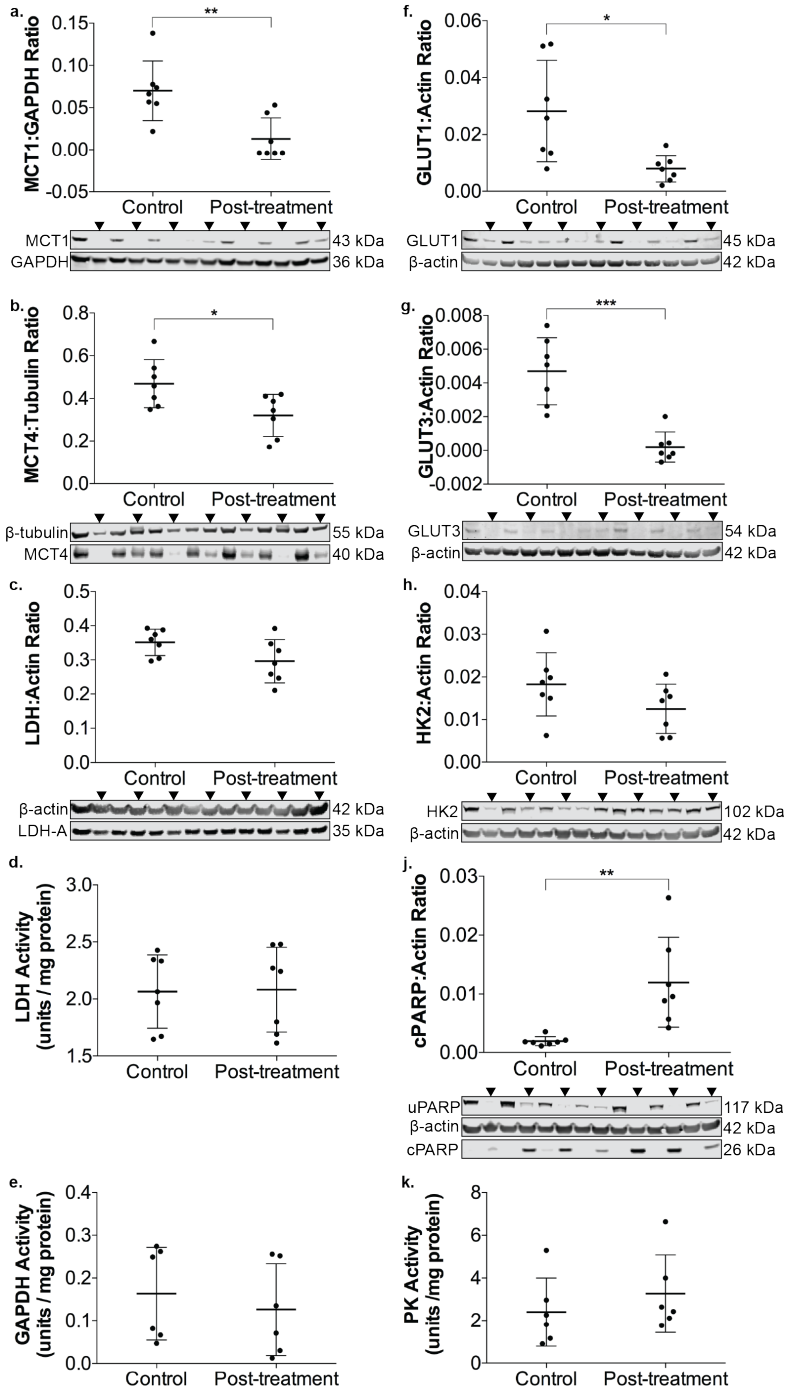

Figure 6.9. Expression and enzyme activity changes induced by MEDI3039 treatment. Arrows above western blots indicate post-treatment tumours. **(a)** MCT1 expression; **(b)** MCT4 expression; **(c)** LDH-A expression; **(d)** LDH activity; **(e)** GAPDH activity; **(f)** GLUT1 expression; **(g)** GLUT3 expression; **(h)** HK2 expression; **(j)** PARP expression**; (k)** pyruvate kinase activity. Abbreviations: cPARP – cleaved PARP; uPARP – uncleaved PARP.

Given the discrepancy between [^{18}F]FDG uptake and lactate production in tumours, the activity of glyceraldehyde-3-phosphate dehydrogenase (GAPDH) and pyruvate kinase (PK) were measured but treatment did not change activity of either these glycolytic enzymes.

6.3.9. Measurement of [^{18}F]FDG and its metabolites in tumour extracts

As [1,6 $^{13}C_2$]glucose could not be differentiated from [1,6 $^{13}C_2$]glucose-6-phosphate using NMR, HPLC measurements on tumour extracts were used to determine whether treatment affected [^{18}F]FDG phosphorylation (Figure 6.10). In Colo205 tumours >90% of [^{18}F]FDG was phosphorylated regardless of MEDI3039 treatment. The ratio of [^{18}F]FDG/[^{18}F]FDG-6-*P* was 6.2 ± 3% prior to treatment and 7.0 ± 3.7% after treatment (n =3, *P* = 0.8). In addition to [^{18}F]FDG and [^{18}F]FDG-6-*P* peaks at retention times of 2 and 6 min respectively, we observed peaks at 8.5, 9, 20 and 22.5 min. The peak at 20 min, assigned to [^{18}F]FD-6-PGL[236], was reduced in treated tumours suggesting that MEDI3039 treatment reduced flux into the pentose phosphate pathway.

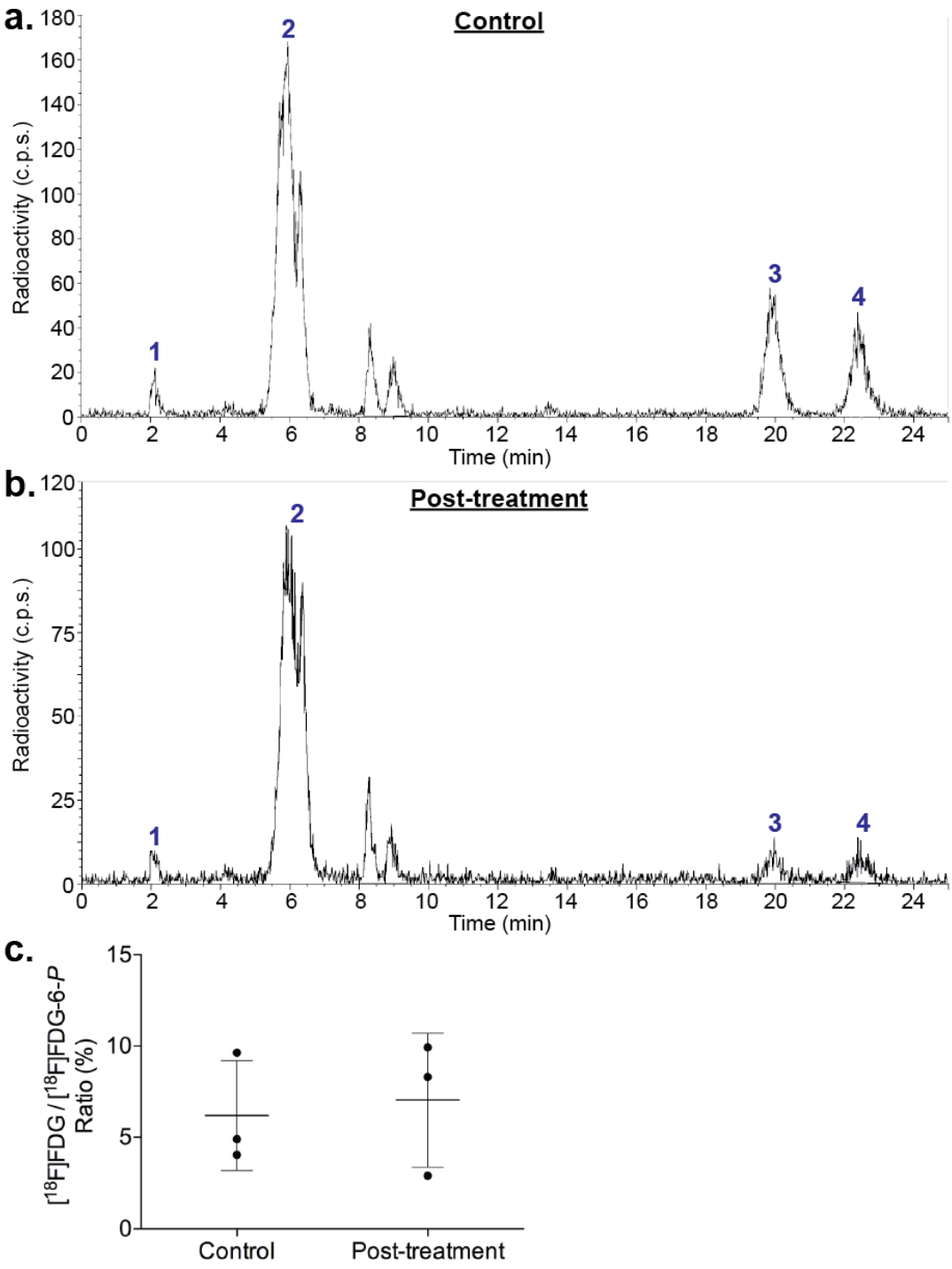

Figure 6.10. RadioHPLC measurements of [^{18}F]FDG metabolism in Colo205 tumours 24 h after control or MEDI3039 treatment. Examples of radioHPLC chromatograms from **(a)** a control tumour and **(b)** a MEDI3039 treated tumour. **(c)** Comparison of [^{18}F]FDG/[^{18}F]FDG-6*P* ratios in control and MEDI3039 treated tumours. Labelled metabolites: 1, [^{18}F]FDG, 2, [^{18}F]FDG-6-*P*; 3, [^{18}F]FD-PGL; 4, [^{18}F]FDG-1,6-P_2.

6.4. Discussion

Earlier detection of treatment response is one of the most likely clinical applications of hyperpolarised [1-^{13}C]pyruvate[110, 111]. Previous pre-clinical studies in models of breast cancer and glioma have demonstrated reductions in label flux from [1-^{13}C]pyruvate to lactate prior to a reduction in tumour volume[161, 169]. However, others have failed to demonstrate the superiority of hyperpolarised [1-^{13}C]pyruvate over reductions in tumour volume or [^{18}F]FDG uptake[69, 107, 173].

Cytotoxic chemotherapeutic agents can have direct effects on metabolic pathways, for example, etoposide is known to inhibit oxidative phosphorylation[220, 237]. Therefore, any effects observed with metabolic imaging may be drug-specific, rather than a generic measure of treatment response. The aim of this study was to use a targeted agent to induce apoptosis which avoided potential direct effects of the drug on glycolytic enzyme expression and allowed comparison of hyperpolarised [1-^{13}C]pyruvate and [^{18}F]FDG to provide a generic marker of treatment response in the colorectal (Colo205) and breast (MDA-MB-231) xenograft models. As reported previously, MEDI3039 was highly effective at inducing apoptosis in tumours with no detectable side effects[232, 238]. In two out of three tumours treatment increased survival from under two weeks in control animals to a minimum of six months in treated mice. To study early detection of treatment response we used 24 h as the earliest possible timepoint between repeated i.v. cannulations and anaesthesia sessions. At 24 h after treatment there were marked increases in histological markers of cell death (CC3 and TUNEL staining), decreased mStrawberry fluorescence in MDA-MB-231 tumours and reductions in bioluminescence in both tumour types, indicating a loss of ATP, which was confirmed in tumour extracts. In both tumour types label flux from hyperpolarised [1-^{13}C]pyruvate to lactate was decreased by MEDI3039 treatment at 24 h, preceding

changes in tumour volume. Decreased labelling can be explained by decreased MCT1 and MCT4 expression and a reduction in the size of the lactate pool[160].

The failure to observe a significant decrease in [^{18}F]FDG uptake in treated tumours was surprising given the degree of cell death observed histologically. Although we observed significant decreases in GLUT1 and GLUT3 expression, HK2 expression did not change and there was a slight increase in perfusion after treatment. The relationship between [^{18}F]FDG accumulation in tissues is multi-factorial and poorly understood, with studies not demonstrating a consistent relationship between [^{18}F]FDG uptake and GLUT and hexokinase expression[67, 71]. Here ^{13}C NMR measurements of [1,6 $^{13}C_2$]glucose metabolism and radioHPLC measurements of [^{18}F]FDG metabolism showed that treatment of Colo205 tumours reduced glycolytic flux to lactate, flux into the TCA cycle and PPP but that phosphorylation of [^{18}F]FDG was maintained. This suggests that, contrary to the generally accepted view, [^{18}F]FDG-6-*P* accumulation in tumours is not necessarily reflective of glycolytic flux and that the differential response seen with [^{18}F]FDG-PET and [1-^{13}C]pyruvate was not due to a switch to oxidative metabolism after treatment[183]. That hyperpolarised [1-^{13}C]pyruvate can detect changes in glycolytic flux, but not [^{18}F]FDG, is a reflection that the rate of exchange between pyruvate and lactate is partly dependent on the lactate concentration which is determined primarily by glycolytic flux whereas the accumulation of [^{18}F]FDG is only dependent on transport and phosphorylation[160].

In a previous study [^{18}F]FDG uptake did not decrease in Colo205 and HT29 xenografts following treatment with conatumumab, a monoclonal antibody targeting DR5 (the same target as MEDI3039), despite histological evidence of cell death and ^{99m}Tc-duramycin SPECT detection of phosphatidylethanolamine externalisation during apoptosis[190]. The authors attributed the failure of [^{18}F]FDG to detect response

to treatment to the “metabolic flare” effect, which has been reported in several small case studies[190]. In metastatic colorectal carcinoma, four patients with increased [^{18}F]FDG uptake in liver metastases one-two weeks after 5-fluorouracil treatment had the lowest [^{18}F]FDG uptake after four-five weeks[239]. Similar observations have been reported in breast cancer, where a metabolic flare following initiation of tamoxifen treatment was predictive of response to treatment[89]. The attribution of this effect to macrophage infiltration and activation is based on the work of Kubota et al. who used micro-autoradiography to demonstrate that [^{18}F]FDG in uptake is relatively higher in macrophages and granulation tissue[87]. However, they also concluded, “these findings do not mean that the inflammatory cells are the major source of radioactivity of [^{18}F]FDG in tumour tissue. Despite more active uptake of [^{18}F]FDG by inflammatory cells within or around the tumour, it is reasonable to consider that most of the radioactivity of [^{18}F]FDG the whole tumour originates from viable tumour cells because they consist of the major component of the tumour mass[87].” By using FACS to sort labelled populations we were able to quantify the [^{18}F]FDG uptake per cell. We defined a phagocytic population as CD45+ and CD11b+, presumed in tumours to be mostly macrophages[240]. The majority of the CD11b+ population was also positive for mStrawberry+, both before and after treatment, indicative of tumour cell phagocytosis. Although macrophages were the most glycolytically active cell type, their low numbers meant that the majority of [^{18}F]FDG] in the tumour accumulated in tumour cells, corroborating the findings of Kubota et al.[87]. In these tumours this excluded inflammatory infiltration and activation as a cause of “metabolic flare” and the failure of [^{18}F]FDG to detect treatment response. An obvious limitation of this study is the use of subcutaneous human xenografts in mice with greatly reduced numbers of T-cells[241]. However, the proportion of phagocytes in Colo205 tumours was less than 5% in all

tumours which is similar to the numbers found in most early human colorectal tumours[242]. In a minority of human colorectal tumours, macrophages represent greater than 10% of the total cells which could potentially lead to higher proportional uptake in the immune cells and a greater effect on [^{18}F]FDG-PET than demonstrated in our study[242].

6.5. Conclusions

This study shows that hyperpolarised [1-^{13}C]pyruvate MRI can be used for the early detection of cell death after treatment with changes in lactate labelling preceding a reduction in tumour volume, whereas no response to treatment was detected with [^{18}F]FDG-PET. Furthermore, these experiments showed that [^{18}F]FDG-6-*P* accumulation in tumours does not necessarily reflect glycolytic flux and that the failure of [^{18}F]FDG-PET to detect treatment response could not be attributed to inflammatory cell infiltration or a “metabolic flare” effect.

7. Discussion and conclusions

7.1. Summary of results

- The [^{18}F]FDG tumour-to-background ratio continued to increase beyond 60 min post-injection in subcutaneous tumours whereas in autochthonous Eμ-*Myc* tumours uptake reached a maximum after approximately 60 min.
- Fasting mice prior to imaging enhanced tumour [^{18}F]FDG uptake and suppressed myocardial uptake.
- In EL4 murine lymphomas, etoposide treatment reduced [^{18}F]FDG uptake and GLUT1 and GLUT3 expression. An inconsistent change in labelled lactate/pyruvate ratio reflected variable levels of cell death and no significant change in MCT1 and MCT4 expression, LDH activity or PARP cleavage.
- In Eμ-*Myc* mice tumour volume, [^{18}F]FDG SUV and labelled lactate/pyruvate ratio all decreased similarly following treatment with cyclophosphamide but also decreased in untreated mice. Hyperpolarised [1-^{13}C]pyruvate improved tumour specificity compared to [^{18}F]FDG.
- In Colo205 and MDA-MB-231 tumours treated with MEDI3039, labelled lactate/pyruvate ratio and bioluminescence decreased prior to a decrease in tumour volume. This change was accompanied by a large increase in cell death and PARP cleavage and a decrease in MCT1 and MCT4 expression.
- MEDI3039 treatment resulted in a relatively small decrease in [^{18}F]FDG uptake in MDA-MB-231 tumours and no decrease in Colo205 tumours despite a reduction in GLUT1 and GLUT3 expression.
- In Colo205 tumours the phosphorylation (and subsequent trapping) of [^{18}F]FDG did not change after treatment, despite there being a significant reduction in further metabolism.

- The most [^{18}F]FDG-avid cells in Colo205 tumours were phagocytes although their low numbers meant that the majority of total uptake occurs into tumour cells. The high uptake of phagocytes did not contribute to the lack of treatment response seen using [^{18}F]FDG-PET.

7.2. Discussion

Anatomical imaging is essential in clinical practice to diagnose, stage, determine therapeutic strategy and monitor treatment response. However, it is becoming increasingly apparent that, for further improvements in outcomes to be made, knowing the site and spread of a tumour is insufficient and understanding and targeting individual tumour biology is required. Uniquely, molecular imaging can spatially map functional information providing a macroscopic understanding of tumours not possible using circulating biomarkers or biopsy-derived tissue. Delays in detecting tumour responses to treatment result in significant morbidity, delay switching to alternative therapy and result in prolonged use of increasingly expensive drugs. As molecular changes occur prior to changes in volume, molecular imaging has great potential for early detection of tumour response to treatment as already demonstrated clinically using [^{18}F]FDG[83, 84].

The first uses of hyperpolarised [1-^{13}C]pyruvate to monitor response to treatment in prostate cancer patients have yielded positive results[110, 165]. The aim of this study was to compare hyperpolarised [1-^{13}C]pyruvate with [^{18}F]FDG-PET for detecting tumour responses to treatment. The increased specificity of [1-^{13}C]pyruvate for the Warburg effect may yield improved sensitivity of treatment response and also improve imaging of tumours in organs with high background uptake of [^{18}F]FDG e.g., brain and prostate[57, 111]. However, despite numerous previous preclinical studies

demonstrating a decrease in label exchange between hyperpolarised [1-^{13}C]pyruvate and endogenous lactate in tumours following treatment (Table 1.3), studies that have compared the technique to [^{18}F]FDG-PET have failed to demonstrate superiority[69, 173]. In the first study a reduction in [^{18}F]FDG uptake preceded a reduction in pyruvate to lactate label flux, while in the other study tumour volume was better indicator of response than either molecular imaging technique[69, 173]. Here we demonstrated that hyperpolarised [1-^{13}C]pyruvate and lactate can be imaged *in vivo* in 3D at high spatial and temporal resolution, although the investigation of intra-tumoral heterogeneity was precluded by the low per-voxel signal-to-noise ratio requiring signal averaging over the whole tumour for robust analysis[149, 221]. Four different tumour models treated with three different chemotherapeutics and imaged with [1-^{13}C]pyruvate and [^{18}F]FDG produced three different results. A reduction in [^{18}F]FDG SUV and tumour volume was seen in EL4 tumours treated with etoposide, hyperpolarised [1-^{13}C]pyruvate detected responses of Colo205 and MDA-MB-231 tumours to MEDI3039 and all three modalities detected responses of Eμ-*Myc* tumours to cyclophosphamide. The variable effect of treatment on imaging with [^{18}F]FDG and [1-^{13}C]pyruvate clearly indicates that, in cells undergoing drug-induced apoptosis, glycolysis is not globally inhibited but affected reactions are probably specific to the administered drug (although the contributions of tumour type and mouse breed may also contribute to the variation observed)[243]. [^{18}F]FDG and [1-^{13}C]pyruvate measure components of a common pathway but they measure separate reactions and neither is a surrogate for total glycolysis. [^{18}F]FDG measures uptake and phosphorylation and does not report on the subsequent metabolism of glucose-6-*P* which, in addition to conversion to pyruvate, can enter the PPP, the glycogen synthesis pathway or numerous other pathways *via* glycolytic intermediates. The insensitivity of [^{18}F]FDG to changes in metabolism

downstream of hexokinase is highlighted by the experiments in Colo205 tumours treated with MEDI3039 where [^{18}F]FDG-6-*P* continued to accumulate despite an almost complete inhibition of further glucose metabolism. In this instance the reduction in tumour lactate concentration and MCT1 and MCT4 expression meant that hyperpolarised [1-^{13}C]pyruvate was a more sensitive marker of treatment response than [^{18}F]FDG. In EL4 tumours where the predominant effect of treatment on glycolysis was to reduce GLUT1 and GLUT3 expression, [^{18}F]FDG was the more sensitive marker of response. Although the relationship between irreversible [^{18}F]FDG uptake and GLUT expression is complex, as demonstrated in Colo205 tumours treated with MEDI3039 where a reduction in GLUT expression did not result in a reduction in [^{18}F]FDG uptake, in EL4 tumours a correlation has been demonstrated in two separate studies[67, 69]. The variable response seen with hyperpolarised [1-^{13}C]pyruvate in EL4 tumours was attributed to the variable levels of pre-treatment cell death which also has potential clinical relevance as human tumours have variable levels of pre-existing necrosis[244].

The studies reported in Chapters 2 and 4 demonstrate the importance of rigorous experimental design. Understanding the impact of animal handling is essential for pre-clinical imaging to avoid potentially false conclusions. Fasting and isoflurane anaesthesia have been shown previously to reduce background [^{18}F]FDG uptake and this study corroborated these findings and also showed that fasting enhances tumour uptake[187]. In many cases sub-optimal imaging is sufficient as, particularly in clinical imaging, [^{18}F]FDG imaging is only used for lesion detection. However, in Eμ-*Myc* cervical tumours [^{18}F]FDG uptake by tissues adjacent to the tumour had a significant impact on interpretation that could be minimised by anaesthesia throughout the uptake period. Similarly, improved characterisation of

tumours may be possible using dynamic imaging or performing static scans at later time points[199-203].

The results presented here demonstrate the potential power of combining [18F]FDG-PET and hyperpolarised [1-^{13}C]pyruvate MR imaging to measure multiple steps of glycolysis. Either modality alone would have only detected a response to treatment in three of four tumour types whereas combined imaging detected responses in all tumours. The conversion of hyperpolarised [U-^{2}H, U-^{13}C]glucose to lactate reflects flux through the entire glycolytic pathway which, theoretically, would also have detected responses to treatment in all models and could therefore be a single assay for data obtainable by combining [^{18}F]FDG and hyperpolarised [1-^{13}C]pyruvate. However, clinical translation of hyperpolarised [U-^{2}H, U-^{13}C]glucose is currently limited by its short T_1 and low polarisation[119]. Despite the possible improvements in hyperpolarised MRI, hybrid PET/MR systems may offer the best of both worlds: tumour and metastasis identification using the unrivalled sensitivity of [^{18}F]FDG and ^{1}H MRI and the ability to further characterise identified lesions with one or more hyperpolarised substrates in a single imaging session[245]. Functional ^{1}H MR imaging has also shown the potential to detect tumour responses to treatment earlier than volume measurements. For example, diffusion weighted imaging (DWI) and an is a routine part of MR assessment of many tumour types and has demonstrated efficacy as a biomarker of response to a wide range of treatments with changes usually preceding decreases in tumour volume[246, 247]. The mono-exponential apparent diffusion coefficient (ADC) is the simplest and most frequently used mathematical model applied to DWI images to semi-quantitatively describe the diffusion characteristics of tissues. In the vast majority of cases tumour ADC increases following a response to treatment, theoretically due to decreased cell membrane integrity, cell

death and a relative increase in the interstitial water volume[248]. However, immediately post-treatment a transient decrease in ADC has also been observed which may be due to the converse effects of cytotoxic oedema, inflammation and fibrosis[249].

Hybrid PET/MR facilitates clinical comparison of hyperpolarised substrates, PET tracers and multi-parametric ^{1}H-MRI in a single imaging session[250]. This has been demonstrated in rats with in a clinical PET/MR system where the ADC correlated with measurements of [^{18}F]FDG uptake (SUV and total lesion glycolysis) but not measurements of [1-^{13}C]pyruvate metabolism (k_{PL} and AUC), the discrepancy being attributed to the low spatial resolution of ^{13}C chemical shift imaging and the limited numbers in the study[251]. In a separate study EL4 murine lymphomas treated with a vascular disrupting agent, changes in [1-^{13}C]pyruvate and 1,4-$^{13}C_2$]fumarate metabolism were demonstrated at 6 h post-treatment whereas reductions in the ADC were not observed until 24 h post-treatment[167]. However, DWI is also an evolving field and earlier and more accurate detection of response to treatment than is possible with ADC has been reported in patients using more complex modelling of DWI, for example using IVIM (intravascular incoherent motion) and VERDICT (Vascular, Extracellular and Restricted Diffusion for Cytometry in Tumours), although the former has produced inconsistent results particularly in prostate cancer[252, 253].

The capability of hyperpolarised imaging to provide novel insights into tumour metabolism *in vivo* is unrivalled which, as well as improving our understanding of tumour biology, has great potential to identify novel therapeutic targets and potentially be introduced as a companion diagnostic. However, several barriers to clinical translation still exist.

Further technical development, primarily focussed on improving the signal-to-noise ratio and the reliability of equipment, is required to continue the considerable

progress made in the last decade. The hyperpolarised signal that is initially available can be increased by increasing the level of polarisation (which has already been improved considerably by using the latest generation of polarisers[105]), improved and faster injection protocols and increased probe concentrations. Annihilation of the free radical and removal of gadolinium ions following polarisation would substantially increase the pre-injection T_1 and, along with the increasing clinical evidence that injection of hyperpolarised substrates is safe[111], may also help to relax the stringent and time consuming quality control practices currently employed[254, 255]. Following injection, improvements in the hardware and sequence design can help preserve and take advantage of the available signal. These include increasing the magnetic field and gradient strengths and improving the ^{13}C coil design to permit uniform sensitivity over larger volumes and parallel acquisition to reduce the number of phase encoding steps required[256]. From the first studies that employed spectroscopy and single time-point chemical shift imaging[107], sequences have already improved considerably to both increase spatial and temporal resolution whilst minimising substrate excitation to preserve the available signal. Numerous sequences that rapidly acquire 3D spatial, temporal and spectral data whilst maximising signal-to-noise have been developed using spectral-spatial and spectroscopic echo-planar and spiral imaging[149, 221, 256, 257], balanced steady state free precession[150, 258], and indirect detection by polarisation transfer from ^{13}C to ^{1}H nuclei[153]. So far, ^{13}C echo-planar spectroscopic imaging (EPSI) has been the most widely used in human studies largely due to being less prone to artefacts and less demanding on gradients than spiral acquisitions and more reliable at low field strength than spectral-spatial excitation[257]. Improvements in image reconstruction, potentially through the use of compressed sensing, also have great potential to reduce the acquisition time and crucially the number of excitations required

which leads to preservation of hyperpolarisation and increases in the available signal[259].

Assuming that sufficient signal-to-noise ratio can be achieved there are several questions to be answered prior to hyperpolarised imaging becoming part of routine clinical practice. The repeatability of hyperpolarised in pre-clinical imaging has been demonstrated in pre-clinical studies of tumours and normal tissue[233, 260]. Sufficient repeatability in human studies to permit accurate differentiation of normal and pathological tissue and reproducibility across multiple sites is an important goal for the early clinical studies[256]. Comparisons between hyperpolarised imaging, current state-of-the-art imaging techniques (including [^{18}F]FDG-PET and multi-parametric ^{1}H MRI) and histological classifiers can be incorporated into repeatability studies to build on the proof-of-concept studies already performed[110, 111, 261] and, ultimately, these initial trials should begin to answer the critical question of whether hyperpolarised MRI can provide novel information that can guide clinical decision making[256].

7.3. Conclusions

[^{18}F]FDG-PET and hyperpolarised [1-^{13}C]pyruvate were used to detect the response of four tumour models to treatment with three different chemotherapy drugs. In human colorectal and breast adenocarcinoma models a reduction in lactate labelling following injection of hyperpolarised [1-^{13}C]pyruvate detected cell death prior to a reduction in tumour volume when [^{18}F]FDG-PET did not detect a response. However, in EL4 tumours where cell death was variable before and after treatment, [^{18}F]FDG and tumour volume measurements detected a response to etoposide treatment whereas there was no significant change in labelled lactate/pyruvate ratio. In Eμ-*Myc* mice volume, labelled lactate/pyruvate ratio and [^{18}F]FDG SUV decreased

proportionally, although the response of these lymphomas was not necessarily due to the drug. Despite the discrepancies between tumour models and drug treatments, combined imaging with [^{18}F]FDG and hyperpolarised [1-^{13}C]pyruvate imaging detected responses in all tumours, providing a persuasive argument for evaluation of the technique in clinical trials.

References

1. Ferlay J SI, Ervik M, Dikshit R, Eser S, Mathers C, Rebelo M, Parkin DM, Forman D, Bray, F. GLOBOCAN 2012 v1.0, Cancer Incidence and Mortality Worldwide: IARC CancerBase No. 11 [Internet]. Lyon, France: International Agency for Research on Cancer; 2013.

2. UK. CR. 2018 [Available from: https://www.cancerresearchuk.org/health-professional/cancer-statistics/mortality - heading-Zero.

3. Evan GI, Vousden KH. Proliferation, cell cycle and apoptosis in cancer. Nature. 2001;411(6835):342-8.

4. De Bont R, van Larebeke N. Endogenous DNA damage in humans: a review of quantitative data. Mutagenesis. 2004;19(3):169-85.

5. Ozturk M. p53 mutation in hepatocellular carcinoma after aflatoxin exposure. Lancet. 1991;338(8779):1356-9.

6. Alexandrov LB, Ju YS, Haase K, Van Loo P, Martincorena I, Nik-Zainal S, et al. Mutational signatures associated with tobacco smoking in human cancer. Science. 2016;354(6312):618-22.

7. Denissenko MF, Pao A, Tang M, Pfeifer GP. Preferential formation of benzo[a]pyrene adducts at lung cancer mutational hotspots in P53. Science. 1996;274(5286):430-2.

8. Lynch M. Rate, molecular spectrum, and consequences of human mutation. Proc Natl Acad Sci U S A. 2010;107(3):961-8.

9. Saul RL, Ames BN. Background levels of DNA damage in the population. Basic Life Sci. 1986;38:529-35.

10. Tubbs A, Nussenzweig A. Endogenous DNA Damage as a Source of Genomic Instability in Cancer. Cell. 2017;168(4):644-56.

11. Martincorena I, Raine KM, Gerstung M, Dawson KJ, Haase K, Van Loo P, et al. Universal Patterns of Selection in Cancer and Somatic Tissues. Cell. 2017;171(5):1029-41 e21.

12. Martincorena I, Roshan A, Gerstung M, Ellis P, Van Loo P, McLaren S, et al. Tumor evolution. High burden and pervasive positive selection of somatic mutations in normal human skin. Science. 2015;348(6237):880-6.

13. Lawrence MS, Stojanov P, Mermel CH, Robinson JT, Garraway LA, Golub TR, et al. Discovery and saturation analysis of cancer genes across 21 tumour types. Nature. 2014;505(7484):495-501.

14. Lawrence MS, Stojanov P, Polak P, Kryukov GV, Cibulskis K, Sivachenko A, et al. Mutational heterogeneity in cancer and the search for new cancer-associated genes. Nature. 2013;499(7457):214-8.

15. Stoler DL, Chen N, Basik M, Kahlenberg MS, Rodriguez-Bigas MA, Petrelli NJ, et al. The onset and extent of genomic instability in sporadic colorectal tumor progression. Proc Natl Acad Sci U S A. 1999;96(26):15121-6.

16. Yates LR, Campbell PJ. Evolution of the cancer genome. Nat Rev Genet. 2012;13(11):795-806.

17. Hesketh R. Introduction to Cancer Biology: Cambridge University Press; 2013.

18. Hillen F, Griffioen AW. Tumour vascularization: sprouting angiogenesis and beyond. Cancer Metastasis Rev. 2007;26(3-4):489-502.

19. Hanahan D, Weinberg RA. Hallmarks of cancer: the next generation. Cell. 2011;144(5):646-74.

20. Stehelin D, Varmus HE, Bishop JM, Vogt PK. DNA related to the transforming gene(s) of avian sarcoma viruses is present in normal avian DNA. Nature. 1976;260(5547):170-3.

21. Warburg O PK, Negelein E. Über den stoffwechsel der carcinomzelle. Biochemische Zeitschrift. 1924;152(1):319-44.

22. Vander Heiden MG, Cantley LC, Thompson CB. Understanding the Warburg effect: the metabolic requirements of cell proliferation. Science. 2009;324(5930):1029-33.

23. Hensley CT, Faubert B, Yuan Q, Lev-Cohain N, Jin E, Kim J, et al. Metabolic Heterogeneity in Human Lung Tumors. Cell. 2016;164(4):681-94.

24. Mazurek S, Grimm H, Boschek CB, Vaupel P, Eigenbrodt E. Pyruvate kinase type M2: a crossroad in the tumor metabolome. Br J Nutr. 2002;87 Suppl 1:S23-9.

25. Cairns RA, Harris IS, Mak TW. Regulation of cancer cell metabolism. Nat Rev Cancer. 2011;11(2):85-95.

26. Timm KN, Hu DE, Williams M, Wright AJ, Kettunen MI, Kennedy BW, et al. Assessing Oxidative Stress in Tumors by Measuring the Rate of Hyperpolarized [1-13C]Dehydroascorbic Acid Reduction Using 13C Magnetic Resonance Spectroscopy. J Biol Chem. 2017;292(5):1737-48.

27. Davidson SM, Papagiannakopoulos T, Olenchock BA, Heyman JE, Keibler MA, Luengo A, et al. Environment Impacts the Metabolic Dependencies of Ras-Driven Non-Small Cell Lung Cancer. Cell Metab. 2016;23(3):517-28.

28. Marshall AD, van Geldermalsen M, Otte NJ, Lum T, Vellozzi M, Thoeng A, et al. ASCT2 regulates glutamine uptake and cell growth in endometrial carcinoma. Oncogenesis. 2017;6(7):e367.

29. Wise DR, Thompson CB. Glutamine addiction: a new therapeutic target in cancer. Trends Biochem Sci. 2010;35(8):427-33.

30. Cluntun AA, Lukey MJ, Cerione RA, Locasale JW. Glutamine Metabolism in Cancer: Understanding the Heterogeneity. Trends Cancer. 2017;3(3):169-80.

31. Sciacovelli M, Frezza C. Oncometabolites: Unconventional triggers of oncogenic signalling cascades. Free Radic Biol Med. 2016;100:175-81.

32. Yang M, Soga T, Pollard PJ, Adam J. The emerging role of fumarate as an oncometabolite. Front Oncol. 2012;2:85.

33. Yan H, Parsons DW, Jin G, McLendon R, Rasheed BA, Yuan W, et al. IDH1 and IDH2 mutations in gliomas. N Engl J Med. 2009;360(8):765-73.

34. Mardis ER, Ding L, Dooling DJ, Larson DE, McLellan MD, Chen K, et al. Recurring mutations found by sequencing an acute myeloid leukemia genome. N Engl J Med. 2009;361(11):1058-66.

35. Xu W, Yang H, Liu Y, Yang Y, Wang P, Kim SH, et al. Oncometabolite 2-hydroxyglutarate is a competitive inhibitor of alpha-ketoglutarate-dependent dioxygenases. Cancer Cell. 2011;19(1):17-30.

36. DeBerardinis RJ, Chandel NS. Fundamentals of cancer metabolism. Sci Adv. 2016;2(5):e1600200.

37. Muller PA, Vousden KH. p53 mutations in cancer. Nat Cell Biol. 2013;15(1):2-8.

38. Liu J, Zhang C, Hu W, Feng Z. Tumor suppressor p53 and its mutants in cancer metabolism. Cancer Lett. 2015;356(2 Pt A):197-203.

39. Puzio-Kuter AM. The Role of p53 in Metabolic Regulation. Genes Cancer. 2011;2(4):385-91.

40. Contractor T, Harris CR. p53 negatively regulates transcription of the pyruvate dehydrogenase kinase Pdk2. Cancer Res. 2012;72(2):560-7.

41. Wanka C, Brucker DP, Bahr O, Ronellenfitsch M, Weller M, Steinbach JP, et al. Synthesis of cytochrome C oxidase 2: a p53-dependent metabolic regulator that promotes respiratory function and protects glioma and colon cancer cells from hypoxia-induced cell death. Oncogene. 2012;31(33):3764-76.

42. Semenza GL. HIF-1: upstream and downstream of cancer metabolism. Curr Opin Genet Dev. 2010;20(1):51-6.

43. Kim JW, Tchernyshyov I, Semenza GL, Dang CV. HIF-1-mediated expression of pyruvate dehydrogenase kinase: a metabolic switch required for cellular adaptation to hypoxia. Cell Metab. 2006;3(3):177-85.

44. Sabo A, Kress TR, Pelizzola M, de Pretis S, Gorski MM, Tesi A, et al. Selective transcriptional regulation by Myc in cellular growth control and lymphomagenesis. Nature. 2014;511(7510):488-92.

45. Lin CY, Loven J, Rahl PB, Paranal RM, Burge CB, Bradner JE, et al. Transcriptional amplification in tumor cells with elevated c-Myc. Cell. 2012;151(1):56-67.

46. Yeung SJ, Pan J, Lee MH. Roles of p53, MYC and HIF-1 in regulating glycolysis - the seventh hallmark of cancer. Cell Mol Life Sci. 2008;65(24):3981-99.

47. Dang CV. MYC, metabolism, cell growth, and tumorigenesis. Cold Spring Harb Perspect Med. 2013;3(8).

48. Banerjee AK, Beckmann E, Busch U, Buzzi A, Thomas A. The Story of Radiology: ESR - European Society of Radiology; 2013.

49. Beckmann E. CT scanning the early days. The British Journal of Radiology. 2006;79(937):5-8.

50. Lauterbur PC. Image Formation by Induced Local Interactions: Examples Employing Nuclear Magnetic Resonance. Nature. 1973;242:190.

51. Eisenhauer EA, Therasse P, Bogaerts J, Schwartz LH, Sargent D, Ford R, et al. New response evaluation criteria in solid tumours: revised RECIST guideline (version 1.1). Eur J Cancer. 2009;45(2):228-47.

52. Therasse P, Arbuck SG, Eisenhauer EA, Wanders J, Kaplan RS, Rubinstein L, et al. New guidelines to evaluate the response to treatment in solid tumors. European Organization for Research and Treatment of Cancer, National Cancer Institute of the United States, National Cancer Institute of Canada. J Natl Cancer Inst. 2000;92(3):205-16.

53. Michaelis LC, Ratain MJ. Measuring response in a post-RECIST world: from black and white to shades of grey. Nat Rev Cancer. 2006;6(5):409-14.

54. Mattonen SA, Palma DA, Haasbeek CJ, Senan S, Ward AD. Distinguishing radiation fibrosis from tumour recurrence after stereotactic ablative radiotherapy (SABR) for lung cancer: a quantitative analysis of CT density changes. Acta Oncol. 2013;52(5):910-8.

55. Hygino da Cruz LC, Jr., Rodriguez I, Domingues RC, Gasparetto EL, Sorensen AG. Pseudoprogression and pseudoresponse: imaging challenges in the assessment of posttreatment glioma. AJNR Am J Neuroradiol. 2011;32(11):1978-85.

56. Borcoman E, Nandikolla A, Long G, Goel S, Tourneau CL. Patterns of Response and Progression to Immunotherapy. American Society of Clinical Oncology Educational Book. 2018(38):169-78.

57. Brindle K. New approaches for imaging tumour responses to treatment. Nat Rev Cancer. 2008;8(2):94-107.

58. Phelps ME. PET: Physics, Instrumentation, and Scanners. Phelps ME, editor: Springer; 2006. 140 p.

59. Basu S, Kwee TC, Surti S, Akin EA, Yoo D, Alavi A. Fundamentals of PET and PET/CT imaging. Ann N Y Acad Sci. 2011;1228:1-18.

60. Alauddin MM. Positron emission tomography (PET) imaging with (18)F-based radiotracers. Am J Nucl Med Mol Imaging. 2012;2(1):55-76.

61. Paans AM, Vaalburg W, Woldring MG. A comparison of the sensitivity of PET and NMR for in vivo quantitative metabolic imaging. Eur J Nucl Med. 1985;11(2-3):73-5.

62. Nolting DD, Nickels ML, Guo N, Pham W. Molecular imaging probe development: a chemistry perspective. Am J Nucl Med Mol Imaging. 2012;2(3):273-306.

63. Minamimoto R, Senda M, Jinnouchi S, Terauchi T, Yoshida T, Inoue T. Detection of breast cancer in an FDG-PET cancer screening program: results of a nationwide Japanese survey. Clin Breast Cancer. 2015;15(2):e139-46.

64. Barron C, Tsiani E, Tsakiridis T. Expression of the glucose transporters GLUT1, GLUT3, GLUT4 and GLUT12 in human cancer cells. BMC Proceedings. 2012;6(Suppl 3):P4-P.

65. Barron CC, Bilan PJ, Tsakiridis T, Tsiani E. Facilitative glucose transporters: Implications for cancer detection, prognosis and treatment. Metabolism. 2016;65(2):124-39.

66. Mathupala SP, Ko YH, Pedersen PL. Hexokinase II: cancer's double-edged sword acting as both facilitator and gatekeeper of malignancy when bound to mitochondria. Oncogene. 2006;25(34):4777-86.

67. Avril N. GLUT1 expression in tissue and (18)F-FDG uptake. J Nucl Med. 2004;45(6):930-2.

68. Brown RS, Leung JY, Fisher SJ, Frey KA, Ethier SP, Wahl RL. Intratumoral distribution of tritiated-FDG in breast carcinoma: correlation between Glut-1 expression and FDG uptake. J Nucl Med. 1996;37(6):1042-7.

69. Witney TH, Kettunen MI, Day SE, Hu DE, Neves AA, Gallagher FA, et al. A comparison between radiolabeled fluorodeoxyglucose uptake and hyperpolarized

(13)C-labeled pyruvate utilization as methods for detecting tumor response to treatment. Neoplasia. 2009;11(6):574-82, 1 p following 82.

70. Alvarez JV, Belka GK, Pan TC, Chen CC, Blankemeyer E, Alavi A, et al. Oncogene pathway activation in mammary tumors dictates FDG-PET uptake. Cancer Res. 2014;74(24):7583-98.

71. Hong R, Lim SC. (1)(8)F-fluoro-2-deoxyglucose uptake on PET CT and glucose transporter 1 expression in colorectal adenocarcinoma. World J Gastroenterol. 2012;18(2):168-74.

72. Paudyal B, Oriuchi N, Paudyal P, Higuchi T, Nakajima T, Endo K. Expression of glucose transporters and hexokinase II in cholangiocellular carcinoma compared using [18F]-2-fluro-2-deoxy-D-glucose positron emission tomography. Cancer Sci. 2008;99(2):260-6.

73. Aloj L, Caraco C, Jagoda E, Eckelman WC, Neumann RD. Glut-1 and hexokinase expression: relationship with 2-fluoro-2-deoxy-D-glucose uptake in A431 and T47D cells in culture. Cancer Res. 1999;59(18):4709-14.

74. Wang K. Feasibility of high spatial resolution working modes for clinical PET scanner. Int J Med Phys. 2018;7(4):88804.

75. Chung JH, Cho KJ, Lee SS, Baek HJ, Park JH, Cheon GJ, et al. Overexpression of Glut1 in lymphoid follicles correlates with false-positive (18)F-FDG PET results in lung cancer staging. J Nucl Med. 2004;45(6):999-1003.

76. Bos R, van Der Hoeven JJ, van Der Wall E, van Der Groep P, van Diest PJ, Comans EF, et al. Biologic correlates of (18)fluorodeoxyglucose uptake in human breast cancer measured by positron emission tomography. J Clin Oncol. 2002;20(2):379-87.

77. Brucher BL, Weber W, Bauer M, Fink U, Avril N, Stein HJ, et al. Neoadjuvant therapy of esophageal squamous cell carcinoma: response evaluation by positron emission tomography. Ann Surg. 2001;233(3):300-9.

78. Wahl RL, Jacene H, Kasamon Y, Lodge MA. From RECIST to PERCIST: Evolving Considerations for PET response criteria in solid tumors. J Nucl Med. 2009;50 Suppl 1:122S-50S.

79. Kim MK, Ryu JS, Kim SB, Ahn JH, Kim SY, Park SI, et al. Value of complete metabolic response by (18)F-fluorodeoxyglucose-positron emission tomography in oesophageal cancer for prediction of pathologic response and survival after preoperative chemoradiotherapy. Eur J Cancer. 2007;43(9):1385-91.

80. Asagi A, Ohta K, Nasu J, Tanada M, Nadano S, Nishimura R, et al. Utility of contrast-enhanced FDG-PET/CT in the clinical management of pancreatic cancer: impact on diagnosis, staging, evaluation of treatment response, and detection of recurrence. Pancreas. 2013;42(1):11-9.

81. Duong CP, Demitriou H, Weih L, Thompson A, Williams D, Thomas RJ, et al. Significant clinical impact and prognostic stratification provided by FDG-PET in the staging of oesophageal cancer. Eur J Nucl Med Mol Imaging. 2006;33(7):759-69.

82. Johnson P, Federico M, Kirkwood A, Fossa A, Berkahn L, Carella A, et al. Adapted Treatment Guided by Interim PET-CT Scan in Advanced Hodgkin's Lymphoma. N Engl J Med. 2016;374(25):2419-29.

83. Van den Abbeele AD. The lessons of GIST--PET and PET/CT: a new paradigm for imaging. Oncologist. 2008;13 Suppl 2:8-13.

84. Hoekstra OS, Ossenkoppele GJ, Golding R, van Lingen A, Visser GW, Teule GJ, et al. Early treatment response in malignant lymphoma, as determined by planar fluorine-18-fluorodeoxyglucose scintigraphy. J Nucl Med. 1993;34(10):1706-10.

85. Stroobants S, Goeminne J, Seegers M, Dimitrijevic S, Dupont P, Nuyts J, et al. 18FDG-Positron emission tomography for the early prediction of response in advanced soft tissue sarcoma treated with imatinib mesylate (Glivec). Eur J Cancer. 2003;39(14):2012-20.

86. Biggi A, Gallamini A, Chauvie S, Hutchings M, Kostakoglu L, Gregianin M, et al. International validation study for interim PET in ABVD-treated, advanced-stage hodgkin lymphoma: interpretation criteria and concordance rate among reviewers. J Nucl Med. 2013;54(5):683-90.

87. Kubota R, Yamada S, Kubota K, Ishiwata K, Tamahashi N, Ido T. Intratumoral distribution of fluorine-18-fluorodeoxyglucose in vivo: high accumulation in macrophages and granulation tissues studied by microautoradiography. J Nucl Med. 1992;33(11):1972-80.

88. Lazarovici J, Terroir M, Arfi-Rouche J, Michot JM, Mussot S, Florea V, et al. Poor predictive value of positive interim FDG-PET/CT in primary mediastinal large B-cell lymphoma. Eur J Nucl Med Mol Imaging. 2017;44(12):2018-24.

89. Mortimer JE, Dehdashti F, Siegel BA, Trinkaus K, Katzenellenbogen JA, Welch MJ. Metabolic flare: indicator of hormone responsiveness in advanced breast cancer. J Clin Oncol. 2001;19(11):2797-803.

90. The Nobel Prize in Physics 1952: Nobel Media AB; 2014 [Available from: http://www.nobelprize.org/nobel_prizes/physics/laureates/1952/.

91. Levitt M. Spin Dynamics: Basics of Nuclear Magnetic Resonance. 2nd ed: Wiley-Blackwell; 2008. 740 p.

92. de Graaf R. In Vivo NMR Spectroscopy: Principles and Techniques. 2nd ed: Wiley-Blackwell; 2007 26/10/2007.

93. Johnson GA, Benveniste H, Black RD, Hedlund LW, Maronpot RR, Smith BR. Histology by magnetic resonance microscopy. Magn Reson Q. 1993;9(1):1-30.

94. Tofts P. PD: Proton Density of Tissue Water. Quantitative MRI of the Brain.

95. Xiao YD, Paudel R, Liu J, Ma C, Zhang ZS, Zhou SK. MRI contrast agents: Classification and application (Review). Int J Mol Med. 2016;38(5):1319-26.

96. Brindle KM. Imaging metabolism with hyperpolarized (13)C-labeled cell substrates. J Am Chem Soc. 2015;137(20):6418-27.

97. Howe FA, Opstad KS. 1H MR spectroscopy of brain tumours and masses. NMR Biomed. 2003;16(3):123-31.

98. Nelson SJ. Assessment of therapeutic response and treatment planning for brain tumors using metabolic and physiological MRI. NMR Biomed. 2011;24(6):734-49.

99. Brindle KM. NMR methods for measuring enzyme kinetics in vivo. Progress in NMR Spectroscopy. 1988;20:257 - 93.

100. Shulman RG, Rothman DL. 13C NMR of intermediary metabolism: implications for systemic physiology. Annu Rev Physiol. 2001;63:15-48.

101. Ardenkjaer-Larsen JH, Fridlund B, Gram A, Hansson G, Hansson L, Lerche MH, et al. Increase in signal-to-noise ratio of > 10,000 times in liquid-state NMR. Proc Natl Acad Sci U S A. 2003;100(18):10158-63.

102. Comment A. Dissolution DNP for in vivo preclinical studies. J Magn Reson. 2016;264:39-48.

103. Gutte H, Hansen AE, Larsen MM, Rahbek S, Henriksen ST, Johannesen HH, et al. Simultaneous Hyperpolarized 13C-Pyruvate MRI and 18F-FDG PET (HyperPET) in 10 Dogs with Cancer. J Nucl Med. 2015;56(11):1786-92.

104. Lumata L, Merritt ME, Malloy CR, Sherry AD, Kovacs Z. Impact of Gd3+ on DNP of [1-13C]pyruvate doped with trityl OX063, BDPA, or 4-oxo-TEMPO. J Phys Chem A. 2012;116(21):5129-38.

105. Yoshihara HA, Can E, Karlsson M, Lerche MH, Schwitter J, Comment A. High-field dissolution dynamic nuclear polarization of [1-(13)C]pyruvic acid. Phys Chem Chem Phys. 2016;18(18):12409-13.

106. Serrao EM, Kettunen MI, Rodrigues TB, Dzien P, Wright AJ, Gopinathan A, et al. MRI with hyperpolarised [1-13C]pyruvate detects advanced pancreatic preneoplasia prior to invasive disease in a mouse model. Gut. 2016;65(3):465-75.

107. Day SE, Kettunen MI, Gallagher FA, Hu DE, Lerche M, Wolber J, et al. Detecting tumor response to treatment using hyperpolarized 13C magnetic resonance imaging and spectroscopy. Nat Med. 2007;13(11):1382-7.

108. Cunningham CH, Lau JY, Chen AP, Geraghty BJ, Perks WJ, Roifman I, et al. Hyperpolarized 13C Metabolic MRI of the Human Heart: Initial Experience. Circ Res. 2016;119(11):1177-82.

109. Brindle KM, Bohndiek SE, Gallagher FA, Kettunen MI. Tumor imaging using hyperpolarized 13C magnetic resonance spectroscopy. Magn Reson Med. 2011;66(2):505-19.

110. Aggarwal R, Vigneron DB, Kurhanewicz J. Hyperpolarized 1-[13C]-Pyruvate Magnetic Resonance Imaging Detects an Early Metabolic Response to Androgen Ablation Therapy in Prostate Cancer. Eur Urol. 2017;72(6):1028-9.

111. Nelson SJ, Kurhanewicz J, Vigneron DB, Larson PE, Harzstark AL, Ferrone M, et al. Metabolic imaging of patients with prostate cancer using hyperpolarized [1-(1)(3)C]pyruvate. Sci Transl Med. 2013;5(198):198ra08.

112. Gallagher FA, Kettunen MI, Hu DE, Jensen PR, Zandt RI, Karlsson M, et al. Production of hyperpolarized [1,4-13C2]malate from [1,4-13C2]fumarate is a marker of cell necrosis and treatment response in tumors. Proc Natl Acad Sci U S A. 2009;106(47):19801-6.

113. Chen AP, Kurhanewicz J, Bok R, Xu D, Joun D, Zhang V, et al. Feasibility of using hyperpolarized [1-13C]lactate as a substrate for in vivo metabolic 13C MRSI studies. Magn Reson Imaging. 2008;26(6):721-6.

114. Park JM, Khemtong C, Liu SC, Hurd RE, Spielman DM. In vivo assessment of intracellular redox state in rat liver using hyperpolarized [1-13 C]Alanine. Magn Reson Med. 2017;77(5):1741-8.

115. Chaumeil MM, Larson PE, Yoshihara HA, Danforth OM, Vigneron DB, Nelson SJ, et al. Non-invasive in vivo assessment of IDH1 mutational status in glioma. Nat Commun. 2013;4:2429.

116. Salamanca-Cardona L, Shah H, Poot AJ, Correa FM, Di Gialleonardo V, Lui H, et al. In Vivo Imaging of Glutamine Metabolism to the Oncometabolite 2-Hydroxyglutarate in IDH1/2 Mutant Tumors. Cell Metab. 2017.

117. Gallagher FA, Kettunen MI, Day SE, Lerche M, Brindle KM. 13C MR spectroscopy measurements of glutaminase activity in human hepatocellular carcinoma cells using hyperpolarized 13C-labeled glutamine. Magn Reson Med. 2008;60(2):253-7.

118. Gallagher FA, Kettunen MI, Day SE, Hu DE, Karlsson M, Gisselsson A, et al. Detection of tumor glutamate metabolism in vivo using (13)C magnetic resonance spectroscopy and hyperpolarized [1-(13)C]glutamate. Magn Reson Med. 2011;66(1):18-23.

119. Rodrigues TB, Serrao EM, Kennedy BW, Hu DE, Kettunen MI, Brindle KM. Magnetic resonance imaging of tumor glycolysis using hyperpolarized 13C-labeled glucose. Nat Med. 2014;20(1):93-7.

120. Nishihara T, Yoshihara HA, Nonaka H, Takakusagi Y, Hyodo F, Ichikawa K, et al. Direct Monitoring of gamma-Glutamyl Transpeptidase Activity In Vivo Using a Hyperpolarized (13) C-Labeled Molecular Probe. Angew Chem Int Ed Engl. 2016;55(36):10626-9.

121. Welch HG, Black WC. Overdiagnosis in cancer. J Natl Cancer Inst. 2010;102(9):605-13.

122. Klotz L. Prostate cancer overdiagnosis and overtreatment. Curr Opin Endocrinol Diabetes Obes. 2013;20(3):204-9.

123. Howlader N NA, Krapcho M, Miller D, Bishop K, Kosary CL, Yu M, Ruhl J, Tatalovich Z, Mariotto A, Lewis DR, Chen HS, Feuer EJ, Cronin KA. SEER Cancer Statistics Review, 1975-2014, National Cancer Institute. Bethesda, MD, https://seer.cancer.gov/csr/1975_2014/, based on November 2016 SEER data submission, posted to the SEER web site, April 2017. 2017.

124. Chen HY, Larson PEZ, Bok RA, von Morze C, Sriram R, Delos Santos R, et al. Assessing Prostate Cancer Aggressiveness with Hyperpolarized Dual-Agent 3D Dynamic Imaging of Metabolism and Perfusion. Cancer Res. 2017;77(12):3207-16.

125. Hesketh RL, Zhu AX, Oklu R. Radiomics and circulating tumor cells: personalized care in hepatocellular carcinoma? Diagn Interv Radiol. 2015;21(1):78-84.

126. Bode BP, Kaminski DL, Souba WW, Li AP. Glutamine transport in isolated human hepatocytes and transformed liver cells. Hepatology. 1995;21(2):511-20.

127. Bode BP, Souba WW. Modulation of cellular proliferation alters glutamine transport and metabolism in human hepatoma cells. Ann Surg. 1994;220(4):411-22; discussion 22-4.

128. DeBerardinis RJ, Mancuso A, Daikhin E, Nissim I, Yudkoff M, Wehrli S, et al. Beyond aerobic glycolysis: transformed cells can engage in glutamine metabolism that exceeds the requirement for protein and nucleotide synthesis. Proc Natl Acad Sci U S A. 2007;104(49):19345-50.

129. Cabella C, Karlsson M, Canape C, Catanzaro G, Colombo Serra S, Miragoli L, et al. In vivo and in vitro liver cancer metabolism observed with hyperpolarized [5-(13)C]glutamine. J Magn Reson. 2013;232:45-52.

130. Barb AW, Hekmatyar SK, Glushka JN, Prestegard JH. Exchange facilitated indirect detection of hyperpolarized 15ND2-amido-glutamine. J Magn Reson. 2011;212(2):304-10.

131. Park JM, Josan S, Jang T, Merchant M, Watkins R, Hurd RE, et al. Volumetric spiral chemical shift imaging of hyperpolarized [2-(13) c]pyruvate in a rat c6 glioma model. Magn Reson Med. 2016;75(3):973-84.

132. Izquierdo-Garcia JL, Viswanath P, Eriksson P, Cai L, Radoul M, Chaumeil MM, et al. IDH1 Mutation Induces Reprogramming of Pyruvate Metabolism. Cancer Res. 2015;75(15):2999-3009.

133. Zhou W, Feng X, Ren C, Jiang X, Liu W, Huang W, et al. Over-expression of BCAT1, a c-Myc target gene, induces cell proliferation, migration and invasion in nasopharyngeal carcinoma. Mol Cancer. 2013;12:53.

134. Wang ZQ, Faddaoui A, Bachvarova M, Plante M, Gregoire J, Renaud MC, et al. BCAT1 expression associates with ovarian cancer progression: possible implications in altered disease metabolism. Oncotarget. 2015;6(31):31522-43.

135. Tonjes M, Barbus S, Park YJ, Wang W, Schlotter M, Lindroth AM, et al. BCAT1 promotes cell proliferation through amino acid catabolism in gliomas carrying wild-type IDH1. Nat Med. 2013;19(7):901-8.

136. Karlsson M, Jensen PR, in 't Zandt R, Gisselsson A, Hansson G, Duus JO, et al. Imaging of branched chain amino acid metabolism in tumors with hyperpolarized 13C ketoisocaproate. Int J Cancer. 2010;127(3):729-36.

137. Butt SA, Sogaard LV, Magnusson PO, Lauritzen MH, Laustsen C, Akeson P, et al. Imaging cerebral 2-ketoisocaproate metabolism with hyperpolarized (13)C magnetic resonance spectroscopic imaging. J Cereb Blood Flow Metab. 2012;32(8):1508-14.

138. Corti A, Franzini M, Paolicchi A, Pompella A. Gamma-glutamyltransferase of cancer cells at the crossroads of tumor progression, drug resistance and drug targeting. Anticancer Res. 2010;30(4):1169-81.

139. Kato Y, Ozawa S, Miyamoto C, Maehata Y, Suzuki A, Maeda T, et al. Acidic extracellular microenvironment and cancer. Cancer Cell Int. 2013;13(1):89.

140. Gallagher FA, Sladen H, Kettunen MI, Serrao EM, Rodrigues TB, Wright A, et al. Carbonic Anhydrase Activity Monitored In Vivo by Hyperpolarized 13C-Magnetic Resonance Spectroscopy Demonstrates Its Importance for pH Regulation in Tumors. Cancer Res. 2015;75(19):4109-18.

141. Gallagher FA, Kettunen MI, Day SE, Hu DE, Ardenkjaer-Larsen JH, Zandt R, et al. Magnetic resonance imaging of pH in vivo using hyperpolarized 13C-labelled bicarbonate. Nature. 2008;453(7197):940-3.

142. Shchepin RV, Barskiy DA, Coffey AM, Theis T, Shi F, Warren WS, et al. (15)N Hyperpolarization of Imidazole-(15)N2 for Magnetic Resonance pH Sensing via SABRE-SHEATH. ACS Sens. 2016;1(6):640-4.

143. Jiang W, Lumata L, Chen W, Zhang S, Kovacs Z, Sherry AD, et al. Hyperpolarized 15N-pyridine derivatives as pH-sensitive MRI agents. Sci Rep. 2015;5:9104.

144. Duwel S, Hundshammer C, Gersch M, Feuerecker B, Steiger K, Buck A, et al. Imaging of pH in vivo using hyperpolarized 13C-labelled zymonic acid. Nat Commun. 2017;8:15126.

145. Rodic S, Vincent MD. Reactive oxygen species (ROS) are a key determinant of cancer's metabolic phenotype. Int J Cancer. 2018;142(3):440-8.

146. Timm KN, Hartl J, Keller MA, Hu DE, Kettunen MI, Rodrigues TB, et al. Hyperpolarized [U-(2) H, U-(13) C]Glucose reports on glycolytic and pentose phosphate pathway activity in EL4 tumors and glycolytic activity in yeast cells. Magn Reson Med. 2015;74(6):1543-7.

147. Moreno KX, Harrison CE, Merritt ME, Kovacs Z, Malloy CR, Dean Sherry A. Hyperpolarized delta-[1-13 C]gluconolactone as a probe of the pentose phosphate pathway. NMR Biomed. 2017;30(6).

148. Keshari KR, Kurhanewicz J, Bok R, Larson PE, Vigneron DB, Wilson DM. Hyperpolarized 13C dehydroascorbate as an endogenous redox sensor for in vivo metabolic imaging. Proc Natl Acad Sci U S A. 2011;108(46):18606-11.

149. Wang J, Wright AJ, Hu DE, Hesketh R, Brindle KM. Single shot three-dimensional pulse sequence for hyperpolarized 13 C MRI. Magn Reson Med. 2017;77(2):740-52.

150. Milshteyn E, von Morze C, Reed GD, Shang H, Shin PJ, Zhu Z, et al. Development of high resolution 3D hyperpolarized carbon-13 MR molecular imaging techniques. Magn Reson Imaging. 2017;38:152-62.

151. Ji X, Bornet A, Vuichoud B, Milani J, Gajan D, Rossini AJ, et al. Transportable hyperpolarized metabolites. Nat Commun. 2017;8:13975.

152. Capozzi A, Cheng T, Boero G, Roussel C, Comment A. Thermal annihilation of photo-induced radicals following dynamic nuclear polarization to produce transportable frozen hyperpolarized 13C-substrates. Nat Commun. 2017;8:15757.

153. Wang J, Kreis F, Wright AJ, Hesketh RL, Levitt MH, Brindle KM. Dynamic 1 H imaging of hyperpolarized [1-13 C]lactate in vivo using a reverse INEPT experiment. Magn Reson Med. 2017.

154. Siegel JA, Pennington CW, Sacks B. Subjecting Radiologic Imaging to the Linear No-Threshold Hypothesis: A Non Sequitur of Non-Trivial Proportion. J Nucl Med. 2017;58(1):1-6.

155. Vilenchik MM, Knudson AG. Radiation dose-rate effects, endogenous DNA damage, and signaling resonance. Proc Natl Acad Sci U S A. 2006;103(47):17874-9.

156. Hill DK, Orton MR, Mariotti E, Boult JK, Panek R, Jafar M, et al. Model free approach to kinetic analysis of real-time hyperpolarized 13C magnetic resonance spectroscopy data. PLoS One. 2013;8(9):e71996.

157. Asghar Butt S, Sogaard LV, Ardenkjaer-Larsen JH, Lauritzen MH, Engelholm LH, Paulson OB, et al. Monitoring mammary tumor progression and effect of tamoxifen treatment in MMTV-PymT using MRI and magnetic resonance spectroscopy with hyperpolarized [1-13C]pyruvate. Magn Reson Med. 2015;73(1):51-8.

158. Hu S, Balakrishnan A, Bok RA, Anderton B, Larson PE, Nelson SJ, et al. 13C-pyruvate imaging reveals alterations in glycolysis that precede c-Myc-induced tumor formation and regression. Cell Metab. 2011;14(1):131-42.

159. Saito K, Matsumoto S, Takakusagi Y, Matsuo M, Morris HD, Lizak MJ, et al. 13C-MR Spectroscopic Imaging with Hyperpolarized [1-13C]pyruvate Detects Early Response to Radiotherapy in SCC Tumors and HT-29 Tumors. Clin Cancer Res. 2015;21(22):5073-81.

160. Witney TH, Kettunen MI, Brindle KM. Kinetic modeling of hyperpolarized 13C label exchange between pyruvate and lactate in tumor cells. J Biol Chem. 2011;286(28):24572-80.

161. Witney TH, Kettunen MI, Hu DE, Gallagher FA, Bohndiek SE, Napolitano R, et al. Detecting treatment response in a model of human breast adenocarcinoma using hyperpolarised [1-13C]pyruvate and [1,4-13C2]fumarate. Br J Cancer. 2010;103(9):1400-6.

162. Harris T, Eliyahu G, Frydman L, Degani H. Kinetics of hyperpolarized 13C1-pyruvate transport and metabolism in living human breast cancer cells. Proc Natl Acad Sci U S A. 2009;106(43):18131-6.

163. Delgado-Goni T, Miniotis MF, Wantuch S, Parkes HG, Marais R, Workman P, et al. The BRAF Inhibitor Vemurafenib Activates Mitochondrial Metabolism and Inhibits Hyperpolarized Pyruvate-Lactate Exchange in BRAF-Mutant Human Melanoma Cells. Mol Cancer Ther. 2016;15(12):2987-99.

164. Park I, Mukherjee J, Ito M, Chaumeil MM, Jalbert LE, Gaensler K, et al. Changes in pyruvate metabolism detected by magnetic resonance imaging are linked to DNA damage and serve as a sensor of temozolomide response in glioblastoma cells. Cancer Res. 2014;74(23):7115-24.

165. Chen H, Larson P, Gordon J, Bok R, Ferrone M, van Griekinge M, et al. Hyperpolarized-13C Imaging of Treatment Responses on Prostate Cancer Patients using 3D Dynamic CS-EPSI Techniques. Joint Annual Meeting ISMRM-ESMRMB 2018; 20th June 2018; Paris Expo, Porte de Versailles2018.

166. (NICE) NIfHaCE. Prostate cancer: diagnosis and management (NG131). Online2019.

167. Bohndiek SE, Kettunen MI, Hu DE, Witney TH, Kennedy BW, Gallagher FA, et al. Detection of tumor response to a vascular disrupting agent by hyperpolarized 13C magnetic resonance spectroscopy. Mol Cancer Ther. 2010;9(12):3278-88.

168. Bohndiek SE, Kettunen MI, Hu DE, Brindle KM. Hyperpolarized (13)C spectroscopy detects early changes in tumor vasculature and metabolism after VEGF neutralization. Cancer Res. 2012;72(4):854-64.

169. Day SE, Kettunen MI, Cherukuri MK, Mitchell JB, Lizak MJ, Morris HD, et al. Detecting response of rat C6 glioma tumors to radiotherapy using hyperpolarized [1-13C]pyruvate and 13C magnetic resonance spectroscopic imaging. Magn Reson Med. 2011;65(2):557-63.

170. Chaumeil MM, Ozawa T, Park I, Scott K, James CD, Nelson SJ, et al. Hyperpolarized 13C MR spectroscopic imaging can be used to monitor Everolimus treatment in vivo in an orthotopic rodent model of glioblastoma. Neuroimage. 2012;59(1):193-201.

171. Park JM, Spielman DM, Josan S, Jang T, Merchant M, Hurd RE, et al. Hyperpolarized (13)C-lactate to (13)C-bicarbonate ratio as a biomarker for monitoring the acute response of anti-vascular endothelial growth factor (anti-VEGF) treatment. NMR Biomed. 2016;29(5):650-9.

172. Iversen AB, Busk M, Bertelsen LB, Laustsen C, Munk OL, Nielsen T, et al. The potential of hyperpolarized 13C magnetic resonance spectroscopy to monitor the effect of combretastatin based vascular disrupting agents. Acta Oncol. 2017;56(11):1626-33.

173. Ravoori MK, Singh SP, Lee J, Bankson JA, Kundra V. In Vivo Assessment of Ovarian Tumor Response to Tyrosine Kinase Inhibitor Pazopanib by Using Hyperpolarized 13C-Pyruvate MR Spectroscopy and 18F-FDG PET/CT Imaging in a Mouse Model. Radiology. 2017;285(3):830-8.

174. Matsumoto S, Saito K, Takakusagi Y, Matsuo M, Munasinghe JP, Morris HD, et al. In vivo imaging of tumor physiological, metabolic, and redox changes in response to the anti-angiogenic agent sunitinib: longitudinal assessment to identify transient vascular renormalization. Antioxid Redox Signal. 2014;21(8):1145-55.

175. Sandulache VC, Chen Y, Lee J, Rubinstein A, Ramirez MS, Skinner HD, et al. Evaluation of hyperpolarized [1-(1)(3)C]-pyruvate by magnetic resonance to detect ionizing radiation effects in real time. PLoS One. 2014;9(1):e87031.

176. Park JM, Recht LD, Josan S, Merchant M, Jang T, Yen YF, et al. Metabolic response of glioma to dichloroacetate measured in vivo by hyperpolarized (13)C magnetic resonance spectroscopic imaging. Neuro Oncol. 2013;15(4):433-41.

177. Chen AP, Chu W, Gu YP, Cunningham CH. Probing early tumor response to radiation therapy using hyperpolarized [1-(1)(3)C]pyruvate in MDA-MB-231 xenografts. PLoS One. 2013;8(2):e56551.

178. Duwel S, Durst M, Gringeri CV, Kosanke Y, Gross C, Janich MA, et al. Multiparametric human hepatocellular carcinoma characterization and therapy response evaluation by hyperpolarized (13) C MRSI. NMR Biomed. 2016;29(7):952-60.

179. Neveu MA, De Preter G, Joudiou N, Bol A, Brender JR, Saito K, et al. Multi-modality imaging to assess metabolic response to dichloroacetate treatment in tumor models. Oncotarget. 2016;7(49):81741-9.

180. Varna M, Gapihan G, Feugeas JP, Ratajczak P, Tan S, Ferreira I, et al. Stem cells increase in numbers in perinecrotic areas in human renal cancer. Clin Cancer Res. 2015;21(4):916-24.

181. Ehman EC, Johnson GB, Villanueva-Meyer JE, Cha S, Leynes AP, Larson PEZ, et al. PET/MRI: Where might it replace PET/CT? J Magn Reson Imaging. 2017;46(5):1247-62.

182. Gutte H, Hansen AE, Henriksen ST, Johannesen HH, Ardenkjaer-Larsen J, Vignaud A, et al. Simultaneous hyperpolarized (13)C-pyruvate MRI and (18)F-FDG-PET in cancer (hyperPET): feasibility of a new imaging concept using a clinical PET/MRI scanner. Am J Nucl Med Mol Imaging. 2015;5(1):38-45.

183. Gutte H, Hansen AE, Larsen MM, Rahbek S, Johannesen HH, Ardenkjaer-Larsen J, et al. In Vivo Phenotyping of Tumor Metabolism in a Canine Cancer Patient with Simultaneous (18)F-FDG-PET and Hyperpolarized (13)C-Pyruvate Magnetic Resonance Spectroscopic Imaging (hyperPET): Mismatch Demonstrates that FDG may not Always Reflect the Warburg Effect. Diagnostics (Basel). 2015;5(3):287-9.

184. Hansen AE, Gutte H, Holst P, Johannesen HH, Rahbek S, Clemmensen AE, et al. Combined hyperpolarized (13)C-pyruvate MRS and (18)F-FDG PET (hyperPET) estimates of glycolysis in canine cancer patients. Eur J Radiol. 2018;103:6-12.

185. Afshar-Oromieh A, Zechmann CM, Malcher A, Eder M, Eisenhut M, Linhart HG, et al. Comparison of PET imaging with a (68)Ga-labelled PSMA ligand and (18)F-choline-based PET/CT for the diagnosis of recurrent prostate cancer. Eur J Nucl Med Mol Imaging. 2014;41(1):11-20.

186. Morigi JJ, Stricker PD, van Leeuwen PJ, Tang R, Ho B, Nguyen Q, et al. Prospective Comparison of 18F-Fluoromethylcholine Versus 68Ga-PSMA PET/CT in Prostate Cancer Patients Who Have Rising PSA After Curative Treatment and Are Being Considered for Targeted Therapy. J Nucl Med. 2015;56(8):1185-90.

187. Fueger BJ, Czernin J, Hildebrandt I, Tran C, Halpern BS, Stout D, et al. Impact of animal handling on the results of 18F-FDG PET studies in mice. J Nucl Med. 2006;47(6):999-1006.

188. Patrick PS, Hammersley J, Loizou L, Kettunen MI, Rodrigues TB, Hu DE, et al. Dual-modality gene reporter for in vivo imaging. Proc Natl Acad Sci U S A. 2014;111(1):415-20.

189. Harris AW, Pinkert CA, Crawford M, Langdon WY, Brinster RL, Adams JM. The E mu-myc transgenic mouse. A model for high-incidence spontaneous lymphoma and leukemia of early B cells. J Exp Med. 1988;167(2):353-71.

190. Elvas F, Boddaert J, Vangestel C, Pak K, Gray B, Kumar-Singh S, et al. (99m)Tc-Duramycin SPECT Imaging of Early Tumor Response to Targeted Therapy: A Comparison with (18)F-FDG PET. J Nucl Med. 2017;58(4):665-70.

191. Boellaard R, Delgado-Bolton R, Oyen WJ, Giammarile F, Tatsch K, Eschner W, et al. FDG PET/CT: EANM procedure guidelines for tumour imaging: version 2.0. Eur J Nucl Med Mol Imaging. 2015;42(2):328-54.

192. Quantitative FDG-PET Technical Committee. UPICT oncology FDG-PET CT protocol v2.5: Quantitive Imaging Biomarkers Alliance; 2014 [Available from: https://qibawiki.rsna.org/index.php/FDG-PET_Biomarker_Ctte - Quantitative_FDG-PET_Biomarker_Committee_Mission.

193. Belohlavek O, Jaruskova M. [18F]FDG-PET scan in patients with fasting hyperglycemia. Q J Nucl Med Mol Imaging. 2016;60(4):404-12.

194. Sprinz C, Zanon M, Altmayer S, Watte G, Irion K, Marchiori E, et al. Effects of blood glucose level on 18F fluorodeoxyglucose (18F-FDG) uptake for PET/CT in normal organs: an analysis on 5623 patients. Scientific Reports. 2018;8(1):2126.

195. Rosica D, Cheng SC, Hudson M, Sakellis C, Van den Abbeele AD, Kim CK, et al. Effects of hyperglycemia on fluorine-18-fluorodeoxyglucose biodistribution in a large oncology clinical practice. Nucl Med Commun. 2018;39(5):417-22.

196. Langen KJ, Braun U, Rota Kops E, Herzog H, Kuwert T, Nebeling B, et al. The influence of plasma glucose levels on fluorine-18-fluorodeoxyglucose uptake in bronchial carcinomas. J Nucl Med. 1993;34(3):355-9.

197. Lowe VJ, DeLong DM, Hoffman JM, Coleman RE. Optimum scanning protocol for FDG-PET evaluation of pulmonary malignancy. J Nucl Med. 1995;36(5):883-7.

198. Hamberg LM, Hunter GJ, Alpert NM, Choi NC, Babich JW, Fischman AJ. The dose uptake ratio as an index of glucose metabolism: useful parameter or oversimplification? J Nucl Med. 1994;35(8):1308-12.

199. Spence AM, Muzi M, Mankoff DA, O'Sullivan SF, Link JM, Lewellen TK, et al. 18F-FDG PET of gliomas at delayed intervals: improved distinction between tumor and normal gray matter. J Nucl Med. 2004;45(10):1653-9.

200. Boerner AR, Weckesser M, Herzog H, Schmitz T, Audretsch W, Nitz U, et al. Optimal scan time for fluorine-18 fluorodeoxyglucose positron emission tomography in breast cancer. Eur J Nucl Med. 1999;26(3):226-30.

201. Nakayama M, Okizaki A, Ishitoya S, Sakaguchi M, Sato J, Aburano T. Dual-time-point F-18 FDG PET/CT imaging for differentiating the lymph nodes between malignant lymphoma and benign lesions. Ann Nucl Med. 2013;27(2):163-9.

202. Shinya T, Fujii S, Asakura S, Taniguchi T, Yoshio K, Alafate A, et al. Dual-time-point F-18 FDG PET/CT for evaluation in patients with malignant lymphoma. Ann Nucl Med. 2012;26(8):616-21.

203. Tian R, Su M, Tian Y, Li F, Li L, Kuang A, et al. Dual-time point PET/CT with F-18 FDG for the differentiation of malignant and benign bone lesions. Skeletal Radiol. 2009;38(5):451-8.

204. Ziai P, Hayeri MR, Salei A, Salavati A, Houshmand S, Alavi A, et al. Role of Optimal Quantification of FDG PET Imaging in the Clinical Practice of Radiology. Radiographics. 2016;36(2):481-96.

205. Yang Z, Zan Y, Zheng X, Hai W, Chen K, Huang Q, et al. Dynamic FDG-PET Imaging to Differentiate Malignancies from Inflammation in Subcutaneous and In Situ Mouse Model for Non-Small Cell Lung Carcinoma (NSCLC). PLoS One. 2015;10(9):e0139089.

206. Goetz C, Podein M, Braun F, Weber WA, Choquet P, Constantinesco A, et al. Influence of Animal Heating on PET Imaging Quantification and Kinetics: Biodistribution of (18)F-Tetrafluoroborate and (18)F-FDG in Mice. J Nucl Med. 2017;58(7):1162-6.

207. Zhuang H, Pourdehnad M, Lambright ES, Yamamoto AJ, Lanuti M, Li P, et al. Dual time point 18F-FDG PET imaging for differentiating malignant from inflammatory processes. J Nucl Med. 2001;42(9):1412-7.

208. Kokolus KM, Capitano ML, Lee CT, Eng JW, Waight JD, Hylander BL, et al. Baseline tumor growth and immune control in laboratory mice are significantly influenced by subthermoneutral housing temperature. Proc Natl Acad Sci U S A. 2013;110(50):20176-81.

209. Patlak CS, Blasberg RG, Fenstermacher JD. Graphical evaluation of blood-to-brain transfer constants from multiple-time uptake data. J Cereb Blood Flow Metab. 1983;3(1):1-7.

210. van den Hoff J, Oehme L, Schramm G, Maus J, Lougovski A, Petr J, et al. The PET-derived tumor-to-blood standard uptake ratio (SUR) is superior to tumor SUV as a surrogate parameter of the metabolic rate of FDG. EJNMMI Res. 2013;3(1):77.

211. Ghosh A, Cheung YY, Mansfield BC, Chou JY. Brain contains a functional glucose-6-phosphatase complex capable of endogenous glucose production. J Biol Chem. 2005;280(12):11114-9.

212. Green LA, Gambhir SS, Srinivasan A, Banerjee PK, Hoh CK, Cherry SR, et al. Noninvasive methods for quantitating blood time-activity curves from mouse PET

images obtained with fluorine-18-fluorodeoxyglucose. J Nucl Med. 1998;39(4):729-34.

213. Choi Y, Hawkins RA, Huang SC, Brunken RC, Hoh CK, Messa C, et al. Evaluation of the effect of glucose ingestion and kinetic model configurations of FDG in the normal liver. J Nucl Med. 1994;35(5):818-23.

214. Wahl RL, Henry CA, Ethier SP. Serum glucose: effects on tumor and normal tissue accumulation of 2-[F-18]-fluoro-2-deoxy-D-glucose in rodents with mammary carcinoma. Radiology. 1992;183(3):643-7.

215. Tseng J, Kelada O, Peterson J. PET 101: Best Practices for Preclinical 18F-FDG PET Imaging: Perkin Elmer; 2017 [Available from: http://www.perkinelmer.com/lab-solutions/resources/docs/TCH_013772_01_PET101_Best_Practices_Preclinical_18F-FDG_PET_Imaging.pdf.

216. Flores JE, McFarland LM, Vanderbilt A, Ogasawara AK, Williams SP. The effects of anesthetic agent and carrier gas on blood glucose and tissue uptake in mice undergoing dynamic FDG-PET imaging: sevoflurane and isoflurane compared in air and in oxygen. Mol Imaging Biol. 2008;10(4):192-200.

217. Grynberg A, Demaison L. Fatty acid oxidation in the heart. J Cardiovasc Pharmacol. 1996;28 Suppl 1:S11-7.

218. Montecucco A, Zanetta F, Biamonti G. Molecular mechanisms of etoposide. EXCLI J. 2015;14:95-108.

219. Hande KR. Etoposide: four decades of development of a topoisomerase II inhibitor. Eur J Cancer. 1998;34(10):1514-21.

220. Yadav N, Kumar S, Marlowe T, Chaudhary AK, Kumar R, Wang J, et al. Oxidative phosphorylation-dependent regulation of cancer cell apoptosis in response to anticancer agents. Cell Death &Amp; Disease. 2015;6:e1969.

221. Wang J, Wright AJ, Hesketh RL, Hu DE, Brindle KM. A referenceless Nyquist ghost correction workflow for echo planar imaging of hyperpolarized [1-(13) C]pyruvate and [1-(13) C]lactate. NMR Biomed. 2018;31(2).

222. Ayers GD, McKinley ET, Zhao P, Fritz JM, Metry RE, Deal BC, et al. Volume of preclinical xenograft tumors is more accurately assessed by ultrasound imaging than manual caliper measurements. J Ultrasound Med. 2010;29(6):891-901.

223. Wang J, Wright AJ, Hu DE, Hesketh R, Brindle KM. Single shot three-dimensional pulse sequence for hyperpolarized (13) C MRI. Magn Reson Med. 2017;77(2):740-52.

224. Day CP, Merlino G, Van Dyke T. Preclinical mouse cancer models: a maze of opportunities and challenges. Cell. 2015;163(1):39-53.

225. Talmadge JE, Singh RK, Fidler IJ, Raz A. Murine models to evaluate novel and conventional therapeutic strategies for cancer. Am J Pathol. 2007;170(3):793-804.

226. Kersten K, de Visser KE, van Miltenburg MH, Jonkers J. Genetically engineered mouse models in oncology research and cancer medicine. EMBO Mol Med. 2017;9(2):137-53.

227. Brinster RL, Chen HY, Trumbauer M, Senear AW, Warren R, Palmiter RD. Somatic expression of herpes thymidine kinase in mice following injection of a fusion gene into eggs. Cell. 1981;27(1 Pt 2):223-31.

228. Schmitt CA, Rosenthal CT, Lowe SW. Genetic analysis of chemoresistance in primary murine lymphomas. Nature Medicine. 2000;6:1029.

229. Rempel RE, Jiang X, Fullerton P, Tan TZ, Ye J, Lau JA, et al. Utilization of the Emu-Myc mouse to model heterogeneity of therapeutic response. Mol Cancer Ther. 2014;13(12):3219-29.

230. Schindelin J, Arganda-Carreras I, Frise E, Kaynig V, Longair M, Pietzsch T, et al. Fiji: an open-source platform for biological-image analysis. Nat Methods. 2012;9(7):676-82.

231. Wright AJ, Husson ZMA, Hu DE, Callejo G, Brindle KM, Smith ESJ. Increased hyperpolarized [1-(13) C] lactate production in a model of joint inflammation is not accompanied by tissue acidosis as assessed using hyperpolarized (13) C-labelled bicarbonate. NMR Biomed. 2018;31(4):e3892.

232. Greer Y, Gilbert S, Tice D, Lipkowitz S. Abstract 3494: MEDI3039, a novel highly potent tumor necrosis factor (TNF)-related apoptosis-inducing ligand (TRAIL) receptor agonist, induces apoptotic cell death in breast cancer cells. Cancer Research. 2016;76(14 Supplement):3494-.

233. Serrao EM, Rodrigues TB, Gallagher FA, Kettunen MI, Kennedy BW, Vowler SL, et al. Effects of fasting on serial measurements of hyperpolarized [1-(13) C]pyruvate metabolism in tumors. NMR Biomed. 2016;29(8):1048-55.

234. Noebauer-Huhmann IM, Szomolanyi P, Juras V, Kraff O, Ladd ME, Trattnig S. Gadolinium-based magnetic resonance contrast agents at 7 Tesla: in vitro T1 relaxivities in human blood plasma. Invest Radiol. 2010;45(9):554-8.

235. Marin-Valencia I, Yang C, Mashimo T, Cho S, Baek H, Yang XL, et al. Analysis of tumor metabolism reveals mitochondrial glucose oxidation in genetically diverse human glioblastomas in the mouse brain in vivo. Cell Metab. 2012;15(6):827-37.

236. Rokka J, Gronroos TJ, Viljanen T, Solin O, Haaparanta-Solin M. HPLC and TLC methods for analysis of [(18)F]FDG and its metabolites from biological samples. J Chromatogr B Analyt Technol Biomed Life Sci. 2017;1048:140-9.

237. Demel HR, Feuerecker B, Piontek G, Seidl C, Blechert B, Pickhard A, et al. Effects of topoisomerase inhibitors that induce DNA damage response on glucose metabolism and PI3K/Akt/mTOR signaling in multiple myeloma cells. Am J Cancer Res. 2015;5(5):1649-64.

238. Xie B, Tomaszewski MR, Neves AA, Ros S, Hu DE, McGuire S, et al. Optoacoustic Detection of Early Therapy-Induced Tumor Cell Death Using a Targeted Imaging Agent. Clin Cancer Res. 2017;23(22):6893-903.

239. Findlay M, Young H, Cunningham D, Iveson A, Cronin B, Hickish T, et al. Noninvasive monitoring of tumor metabolism using fluorodeoxyglucose and positron emission tomography in colorectal cancer liver metastases: correlation with tumor response to fluorouracil. J Clin Oncol. 1996;14(3):700-8.

240. Cassetta L, Noy R, Swierczak A, Sugano G, Smith H, Wiechmann L, et al. Isolation of Mouse and Human Tumor-Associated Macrophages. Adv Exp Med Biol. 2016;899:211-29.

241. Belizário J. Immunodeficient Mouse Models: An Overview. The Open Immunology Journal. 2009;2:79-85.

242. Liu X, Liu H, Yuan C, Zhang Y, Wang Y, Hu S, et al. CD68-positive tumor-associated macrophages predicts the survival of patients with stage I colorectal cancer. Int J Clin Exp Pathol. 2016;9(11):11676-81.

243. Pradelli LA, Villa E, Zunino B, Marchetti S, Ricci JE. Glucose metabolism is inhibited by caspases upon the induction of apoptosis. Cell Death &Amp; Disease. 2014;5:e1406.

244. Thomlinson RH, Gray LH. The histological structure of some human lung cancers and the possible implications for radiotherapy. Br J Cancer. 1955;9(4):539-49.

245. Kwon HW, Becker AK, Goo JM, Cheon GJ. FDG Whole-Body PET/MRI in Oncology: a Systematic Review. Nucl Med Mol Imaging. 2017;51(1):22-31.

246. Pickles MD, Gibbs P, Lowry M, Turnbull LW. Diffusion changes precede size reduction in neoadjuvant treatment of breast cancer. Magn Reson Imaging. 2006;24(7):843-7.

247. Galban CJ, Hoff BA, Chenevert TL, Ross BD. Diffusion MRI in early cancer therapeutic response assessment. NMR Biomed. 2017;30(3).

248. Afaq A, Andreou A, Koh DM. Diffusion-weighted magnetic resonance imaging for tumour response assessment: why, when and how? Cancer Imaging. 2010;10 Spec no A:S179-88.

249. Hein PA, Kremser C, Judmaier W, Griebel J, Pfeiffer KP, Kreczy A, et al. Diffusion-weighted magnetic resonance imaging for monitoring diffusion changes in

rectal carcinoma during combined, preoperative chemoradiation: preliminary results of a prospective study. Eur J Radiol. 2003;45(3):214-22.

250. Heijmen L, Verstappen MC, Ter Voert EE, Punt CJ, Oyen WJ, de Geus-Oei LF, et al. Tumour response prediction by diffusion-weighted MR imaging: ready for clinical use? Crit Rev Oncol Hematol. 2012;83(2):194-207.

251. Hundshammer C, Braeuer M, Muller CA, Hansen AE, Schillmaier M, Duwel S, et al. Simultaneous characterization of tumor cellularity and the Warburg effect with PET, MRI and hyperpolarized (13)C-MRSI. Theranostics. 2018;8(17):4765-80.

252. Bourne R, Panagiotaki E. Limitations and Prospects for Diffusion-Weighted MRI of the Prostate. Diagnostics (Basel). 2016;6(2).

253. Panagiotaki E, Walker-Samuel S, Siow B, Johnson SP, Rajkumar V, Pedley RB, et al. Noninvasive quantification of solid tumor microstructure using VERDICT MRI. Cancer Res. 2014;74(7):1902-12.

254. Capozzi A, Cheng T, Boero G, Roussel C, Comment A. Thermal annihilation of photo-induced radicals following dynamic nuclear polarization to produce transportable frozen hyperpolarized 13C-substrates. Nature Communications. 2017;8:15757.

255. Marco-Rius I, Cheng T, Gaunt AP, Patel S, Kreis F, Capozzi A, et al. Photogenerated Radical in Phenylglyoxylic Acid for in Vivo Hyperpolarized (13)C MR with Photosensitive Metabolic Substrates. J Am Chem Soc. 2018;140(43):14455-63.

256. Kurhanewicz J, Vigneron DB, Ardenkjaer-Larsen JH, Bankson JA, Brindle K, Cunningham CH, et al. Hyperpolarized (13)C MRI: Path to Clinical Translation in Oncology. Neoplasia. 2019;21(1):1-16.

257. Durst M, Koellisch U, Frank A, Rancan G, Gringeri CV, Karas V, et al. Comparison of acquisition schemes for hyperpolarised (1)(3)C imaging. NMR Biomed. 2015;28(6):715-25.

258. von Morze C, Sukumar S, Reed GD, Larson PE, Bok RA, Kurhanewicz J, et al. Frequency-specific SSFP for hyperpolarized (1)(3)C metabolic imaging at 14.1 T. Magn Reson Imaging. 2013;31(2):163-70.

259. Chen HY, Larson PEZ, Gordon JW, Bok RA, Ferrone M, van Criekinge M, et al. Technique development of 3D dynamic CS-EPSI for hyperpolarized (13) C pyruvate MR molecular imaging of human prostate cancer. Magn Reson Med. 2018;80(5):2062-72.

260. Lau AZ, Chen AP, Barry J, Graham JJ, Dominguez-Viqueira W, Ghugre NR, et al. Reproducibility study for free-breathing measurements of pyruvate metabolism using hyperpolarized (13) C in the heart. Magn Reson Med. 2013;69(4):1063-71.

261. Tran M, Latifoltojar A, Neves JB, Papoutsaki M-V, Gong F, Comment A, et al. First-in-human in vivo non-invasive assessment of intra-tumoral metabolic heterogeneity in renal cell carcinoma. BJR|case reports.0(0):20190003.